

Tau Neutrinos in IceCube

Dissertation

zur Erlangung des akademischen Grades
doctor rerum naturalium
(Dr. rer. nat.)

im Fach: Physik
Spezialisierung: Experimentalphysik

eingereicht an der
Mathematisch-Naturwissenschaftlichen Fakultät
der Humboldt-Universität zu Berlin

von

Neha Lad M. Sc.

geboren am 18. April 1995

Präsidentin der Humboldt-Universität zu Berlin
Prof. Dr. Julia von Blumenthal

Dekanin der Mathematisch-Naturwissenschaftlichen Fakultät
Prof. Dr. Caren Tischendorf

Copyright Notice

This book is released into the public domain using the CC-BY-4.0 code.

To view a copy of the CC-BY-4.0 code, visit:

<https://creativecommons.org/licenses/by/4.0/>

Colophon

This document was typeset with the help of KOMA-Script and L^AT_EX using the open-source kaobook template class.

The source code of this thesis is available at:

https://github.com/LeanderFischer/phd_thesis

Abstract

In icecube, we have many neutrinos, select some very high energy ones, spend 1 year with them to group them in three flavour categories. I guess we will learn something about where they came from by doing this. Pretty normal stuff, not at all racist.

Zusammenfassung

Im IceCube haben wir viele Neutrinos, von denen wir einige mit sehr hoher Energie auswählen, verbringen 1 Jahr mit ihnen, um sie in drei Geschmackskategorien einzuteilen. Ich vermute, dass wir auf diese Weise etwas darüber erfahren, woher sie kommen. Ziemlich normales Zeug, ganz und gar nicht rassistisch.

Contents

Abstract	iii
Zusammenfassung	v
Contents	vii
1 Event Sample,(Re)construction and Particle Identification	1
1.1 Monte Carlo Simulation	1
1.1.1 Icecube simulation chain	1
1.1.2 SnowStorm Simulation	5
1.2 High Energy Starting Event (HESE) sample	6
1.3 Maximum Likelihood Event Reconstruction	8
1.4 Particle Identification of High Energy Neutrinos	10
1.4.1 Reclassification of PeV Double Cascades	14
1.4.2 Tau Polarisation	15
1.4.3 Glashow Cross-Section correction	15
1.5 Influence of South Pole Ice properties on Double Cascades Reconstruction	16
2 Flavour Composition Analysis	19
2.1 Statistical Methods	19
2.1.1 Binned Maximum-likelihood Fits	19
2.1.2 SAY Likelihood	21
2.2 Components of the Likelihood Fit	22
2.2.1 Model parameters	23
2.2.2 Analysis Observables and their Distributions	28
2.3 Analysis Sensitivity	31
3 Results	35
3.1 (Re)Analysing the 7.5 years of HESE Data	36
3.2 Unblinding of 12 years of HESE data	38
3.2.1 Fit results	39
Blind Fit results	39
Full fit results	40
3.2.2 Data/Monte Carlo Agreement	41
3.3 Flavour Composition of Diffuse Astrophysical Neutrinos	44
Why are the limits worse than the previous measurements?	46
Comparison of sensitivities and derived constraints	47
3.4 Discussion	51
APPENDIX	53
Figures	55
Tables	59
Bibliography	61

Event Sample,(Re)construction and Particle Identification

1

In the previous chapters, high-energy neutrino interactions within IceCube was discussed, focusing on how the secondary particles generated from these interactions propagate through the ice. From this, one could deduce that different neutrino flavours can create distinct morphological patterns due to the variety of charged particles produced in the interaction processes. As mentioned in Section ??, these morphological signatures are crucial in identifying the neutrino flavour, although it becomes particularly challenging in the case of tau neutrino-induced double-bang events. Apart from the complexities of reconstruction, another critical aspect is the selection of astrophysical neutrinos from the overwhelming background of atmospheric muons and neutrinos.

In this chapter, the high-energy neutrino sample used for the analysis presented in this thesis will be detailed, along with the reconstruction method used to identify the particles based on the event's morphology. The chapter will begin with a general overview of the simulation chain in IceCube, followed by a brief overview of the SnowStorm simulations used for the analysis. Lastly, the chapter will discuss the influence of the South Pole IceModel on reconstructed Double Cascade events.

1.1 Monte Carlo Simulation .	1
1.1.1 Icecube simulation chain .	1
1.1.2 SnowStorm Simulation . .	5
1.2 High Energy Starting Event (HESE) sample . . .	6
1.3 Maximum Likelihood Event Reconstruction . . .	8
1.4 Particle Identification of High Energy Neutrinos .	10
1.4.1 Reclassification of PeV Double Cascades	14
1.4.2 Tau Polarisation	15
1.4.3 Glashow Cross-Section correction	15
1.5 Influence of South Pole Ice properties on Double Cascades Reconstruction	16

1.1 Monte Carlo Simulation

The hunt for astrophysical neutrino interactions in the IceCube detector is conducted without access to actual data, a method known as **blind analysis**. To develop the selection (rejection) criteria for signal (background) events, and their light yield reconstruction, simulated events are used.¹ By comparing the distribution of an observable quantity between simulated and real data events, conclusions can be drawn about the detected neutrino population. Hence, simulating how IceCube responds to neutrinos and other particles is essential for comprehending the collected data.

Event simulation in IceCube is based on commonly used Monte Carlo methods. The simulation framework covers all stages, from the generation and propagation of a primary particle to the emission and propagation of Cherenkov light, and finally, the digitized waveforms recorded by all hit DOMs in IceCube.

1.1.1 Icecube simulation chain

The IceCube simulation begins with a *particle generator* that simulates a flux of particles hitting the detector. The primary particle can be a neutrino or a cosmic ray particle reaching Earth's atmosphere. Neutrinos may reach the detector directly, while cosmic rays interact with particles in the atmosphere to produce a shower of particles, from which muons and neutrinos can reach the detector by propagating through ice, forming the so-called atmospheric neutrino and atmospheric muon background.

1: In some cases, typically during the development phase of the analysis sample, selection cuts are validated on small subset (10%) of the experimental data, known as *the burn sample*.

Particle Generation

The software that generates neutrinos is called NuGen (Neutrino Generator) and is based on ANIS (All Neutrino Interaction Simulation). To start the simulation, neutrinos of a selected flavour are drawn from a power-law energy spectrum with an equal probability of being a neutrino or antineutrino. Neutrino directions are sampled from an isotropic distribution and aimed to intersect with an imaginary surface centered on the detector. Each neutrino is then propagated in discrete steps through matter encountered on the way to the detector. For each step, a neutrino interacts with a probability² of $1 - e^{-\sigma n \Delta x}$, where σ is the total interaction cross-section and n is the density of nucleons at the location in the Earth. The nucleon density is modelled using the *Preliminary Earth Reference Model (PREM)* [1], which provides the mass density of the Earth as a function of radius. Because the tau has a short lifetime and a large radiation length, it usually transfers a significant portion of its energy to the tau neutrino produced in its decay (see Section ??). This leads to substantial decrease of overall ν_τ flux at higher energies, a phenomenon known as *tau-regeneration* [2]. This so-called earth effect is also taken into account by the NuGen software.

2: a probability that gets stored as propagation weight for each stage and enters in total weight calculations as a *total interaction probability*.

[1]: Dziewonski et al. (1981), *Preliminary reference earth model*

[2]: Halzen et al. (1998), *Tau-neutrino appearance with a 1000 megaparsec baseline*

After enough steps, neutrinos will reach the imaginary cylinder defining the detection volume where they are forced to interact somewhere between the projected entry and exit points of the cylinder according to a uniform distribution. In the case of a muon resulting from a CC ν_μ interaction far outside the surface, the length at which interactions are required to occur is automatically extended backward based on a parameterization of the muon range in ice. When a neutrino interaction is forced, a weight of $p_{\text{int}} = n\sigma L \exp(-n\sigma L_{\text{before}})$ must be assigned, where L_{before} is the distance before the selected interaction point where an interaction may have occurred, and L is the total length where an interaction may have occurred. This weight is often combined with the propagation weight to give a total interaction probability weight $w_{\text{int}} = p_{\text{prop}} p_{\text{int}}$. The interaction type is then randomly selected according to CC, NC, and GR cross-sections, and secondary particles are generated for further propagation by another program. In IceCube, single atmospheric and astrophysical neutrinos cannot be distinguished on an event-by-event basis. Therefore, the NuGen-generated neutrinos are used for both atmospheric and astrophysical fluxes. Neutrinos will have weights assigned to them according to the expected (or tested) atmospheric and astrophysical fluxes, and these weights can be used to calculate an expected event rate.

[3]: Heck et al. (1998), *CORSIKA: A Monte Carlo code to simulate extensive air showers*

To generate atmospheric muons and neutrinos, an adapted version of CORSIKA [3] is used to simulate the production of muons resulting from cosmic ray showers in the Earth's atmosphere. This process begins with a primary particle, typically a nucleus, initiating a cascading shower of particles upon interaction with the atmosphere. Only neutrinos and muons from these showers are capable of reaching the detector. Due to the impracticality of simulating atmospheric neutrino interactions using CORSIKA, only the muons generated in the showers are transmitted to the detector. The software allows for event weighting based on various cosmic ray models. CORSIKA is currently the exclusive software capable of producing muon bundles, which are large numbers of muons origi-

nating from the same cosmic ray shower. However, a major limitation of CORSIKA is its computational expense, as it propagates all particles from a cosmic ray shower, most of which are undetectable in a sub-surface detector like IceCube. To address this drawback, MUONGUN [4] was developed to simulate single muons more efficiently and economically by generating them directly around the detector volume. In the context of HESE (which will be discussed in Section 1.2), the primary background arises from single muons, as muon bundles produce a more continuous light deposition, resulting in a higher likelihood of being vetoed upon entering the detector. Since flux models more complex than a simple power law are often required, NuGen simulations can be re-weighted to match any arbitrary flux. A weight is assigned to each event that reflects the ratio between the desired flux $n_{\text{expected}} = \Phi(E)$ and the generated fluence of neutrinos. The generated fluence can be expressed as,

$$n_{\text{generated}} = \frac{N(E)}{\Omega A_{\perp}} \quad (1.1)$$

where A_{\perp} is the projected area of the detection surface for each neutrino, and Ω is the solid angle covered by the simulation, typically 4π for neutrinos coming from the entire sky. $N(E)$ represents the energy distribution of simulated neutrinos, which, for a power-law distribution with N_0 events and a power-law index γ , spanning from energy E_{min} to E_{max} , is given by:

$$N(E) = \frac{N_0 E^{-\gamma}}{\int_{E_{\text{min}}}^{E_{\text{max}}} E^{-\gamma} dE} \quad (1.2)$$

Here, N_0 refers to the number of neutrino or antineutrino events, and not the total, when separate fluxes for neutrinos and antineutrinos are known. This implies that N_0 represents half of the total number of events generated for each neutrino flavor. Finally, accounting for the interaction weight, the total weight assigned to each neutrino (in units of Hz) is:

$$\begin{aligned} w &= w_{\text{int}} \frac{n_{\text{expected}}}{n_{\text{generated}}} \\ &= w_{\text{int}} \frac{A_{\perp} \Omega \Phi(E)}{N(E)} \end{aligned} \quad (1.3)$$

By summing these weights over all simulated events that pass the event selection, the expected event rate for any desired flux model can be calculated.

Secondary Charged Particle Propagation

Once a particle interaction occurs within the detector volume, the next step is to generate and propagate secondary particles through the ice. Depending on their nature, these secondary particles may undergo further interactions within the ice, with some of them producing detectable Cherenkov light in the detector volume (see Section ?? for details). Both atmospheric muons from air showers and secondary leptons, such as electrons, muons, and taus from CC neutrino interactions, are propagated

[4]: Santen (2014), *Neutrino Interactions in IceCube above 1 TeV: Constraints on Atmospheric Charmed-Meson Production and Investigation of the Astrophysical Neutrino Flux with 2 Years of IceCube Data taken 2010–2012*

a block diagram of simulation chain here

[5]: Koehne et al. (2013), *PROPOSAL: A tool for propagation of charged leptons*

[6]: Chirkin et al. (2004), *Propagating leptons through matter with Muon Monte Carlo (MMC)*

[7]: Voigt (2008), *Sensitivity of the IceCube detector for ultra-high energy electron-neutrino events*

[8]: Radel et al. (2013), *Calculation of the Cherenkov light yield from electromagnetic cascades in ice with Geant4*

[9]: R  del et al. (2012), *Calculation of the Cherenkov light yield from low energetic secondary particles accompanying high-energy muons in ice and water with Geant 4 simulations*

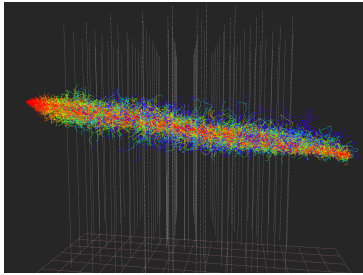


Figure 1.1: Light emission pattern of a simulated muon track event, using the direction propagation program *CLSim*. The colored lines show individual photon paths through ice, with red indicating earlier and blue indicating later compared to an unscattered photon. Figure taken from [10]

[11]: Kopper (n.d.), *CLsim*

[12]: Chirkin (2013), *Photon tracking with GPUs in IceCube*

3: Three for the source position, three for the DOM position, two for the light source orientation, and one for time.

through the ice after they are produced. The software used for lepton propagation is called *PROPOSAL* (Propagator with Optimal Precision and Optimized Speed for All Leptons) [5] and is based on the previous implementation *MMC* (Muon Monte Carlo) [6]. The lepton production is simplified by assuming that the emission angle is aligned with the incident angle of the primary particle, and that it travels at the speed of light, which are both reasonable assumptions above the energy threshold of 100 GeV. The various propagation effects of different particle types and energies, as described in ??, are taken care of by *PROPOSAL*. In particular, highly energetic muons are simulated to have long tracks that are predominantly characterized by stochastic energy losses. Electromagnetic and hadronic cascades, as described in Section ??, are simulated by *CMC* (Cascade Monte Carlo) [7]. It generates individual particle showers by randomly sampling energy losses from the energy-dependent shower parametrization and also takes the LPM-effect into account. The shower parametrizations have been determined by fitting the Cherenkov light yield for a full shower simulation using *GEANT4* (Geometry And Tracking) [8, 9].

Photon Propagation

Once all primary and secondary particles have traversed the detector, the next phase of the simulation process involves the emission and propagation of Cherenkov photons from all visible particles or energy losses (as discussed in Section ??). The number of Cherenkov photons is proportional to the combined track length of all charged particles, and the refraction index of ice. Individual photon propagation is traced through an *OpenCL*-based photon-tracking simulation (as shown in Figure 1.1), known as *CLSim* [11], derived from *Photon Propagation Code* (*PPC*) [12]. The *SPICE* models (as detailed in Section ??) are used to describe the scattering and absorption of photons. Each photon is tracked through multiple scatterings until it either reaches the collection area of a DOM or, more often, is absorbed. *CLSIM* harnesses GPUs for photon propagation due to their efficiency in running numerous simple operations (such as photon scattering) in parallel [12].

Since the direct propagation of photons even by using GPUs can be extremely time and power consuming, an alternative method is used in IceCube that creates a look-up table that stores the expected timing distribution of photoelectrons at a Digital Optical Module (DOM) for various configurations of the light source and DOM. The concept involves simulating a light source (cascade, track, or flasher) at specific depths and directions multiple times, while tracking the photon yield around the source. Initially, the challenge of creating this table seemed daunting due to the complexity of the problem, as it required a table with 9 dimensions³. However, One can take advantage of the approximate horizontal translational and azimuthal symmetry of the ice to reduce the dimensions to 6: depth of the source in ice, zenith angle of the source, displacement vector of the DOM from the source, and time. It is important to note that this approach has its limitations, as it disregards certain effects such as ice layer tilt and anisotropic scattering, which do not adhere to the symmetry assumptions. In recent years, these limitations have been overcome by introducing corrections to scattering lengths (the

so-called *effective distance correction*), which was done while developing the double cascade reconstruction [13] that will be explained in Section 1.4, and also by introducing corrections directly in modelling of the ice to account for ice anisotropy and tilt corrections, see Section ?? for details. Initially, `Photonics` was used to predict and store the expected photon flux in a multi-dimensional histogram structure, but this method had drawbacks such as binning issues and inaccuracies at great distances. Currently, a more effective approach involves fitting the photoelectron distribution obtained from `CLSim` or `PPC` to a tensor product B-spline surface [14]. This offers the advantage of having a smooth function of all 6 coordinates and can address unphysical fluctuations caused by limited statistics through the use of regularization.

Detector Simulation

The detector's response is the final step in the simulation process. The PMT's sensitivity depends on the wavelength and angle of the incoming photon, as well as its quantum efficiency. This means that not every photon will trigger the PMT. The simulation takes into account the varying PMT sensitivity for each photon. Additionally, the simulation considers the angular acceptance of photons, accounting for local scattering variations in the ice. The PMT hardware has been thoroughly calibrated and studied in the lab [15], and these results have been incorporated into the simulation. It's important to model the transit time and jitter of the PMT in the simulation, as these factors affect the timing and width of the pulse. Furthermore, all triggers used in real-time data collection at the South Pole are also included in the simulation. This final step in the simulation process completes the creation of a simulated event.

1.1.2 SnowStorm Simulation

As described in previous section, specifically for photon propagation stage precise knowledge of ice is important. While we use calibration measurements to estimate the detector properties, this only provides limited precision. When conducting simulations, which are crucial for estimating the detector's response, one need to be careful not to assume specific detector properties. For most of the IceCube analyses so far, variations of the detector response were included using a particular strategy: A set of Monte Carlo simulations with *baseline* values of all systematic parameters was created to estimate event rate in the analysis. The baseline value of a systematic parameter is its most likely value determined from calibration. Variations of this baseline event rate caused by a different, *off-baseline*, detector response were estimated using different *discrete systematics sets*. The combination of discrete baseline and systematics sets allows the estimation of the analysis variables as well as their variation with the detector systematics. This variation is typically assumed to be small and estimated with a low-order Taylor expansion. The off-baseline systematics sets are then used to estimate the coefficients of this expansion.

A new approach to model detector systematic uncertainties has been developed in IceCube called, **SnowStorm Method** [16]. The significant difference compared to the discrete systematics approach described above

[13]: Usner (2018), *Search for Astrophysical Tau-Neutrinos in Six Years of High-Energy Starting Events in the IceCube Detector*

[14]: Whitehorn et al. (2013), *Penalized splines for smooth representation of high-dimensional Monte Carlo datasets*

[15]: Abbasi et al. (2010), *Calibration and characterization of the IceCube photomultiplier tube*

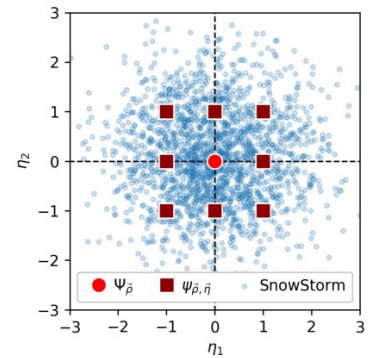


Figure 1.2: Illustration of the SnowStorm method described in the text. It depicts the contrast between numerous discrete shifts in nuisance parameters (indicated by red squares), each necessitating an entire Monte Carlo set, in comparison to a single SnowStorm Monte Carlo (represented by small blue dots). Figure taken from [16]

[16]: Aartsen et al. (2019), *Efficient propagation of systematic uncertainties from calibration to analysis with the SnowStorm method in IceCube*

[17]: Ganster (2024), *Measurement of the high-energy astrophysical neutrino energy spectrum combining muon tracks and cascades measured at the IceCube Neutrino Observatory*

[18]: Naab (2024), *Evidence for a Break in the Diffuse Extragalactic Neutrino Spectrum*

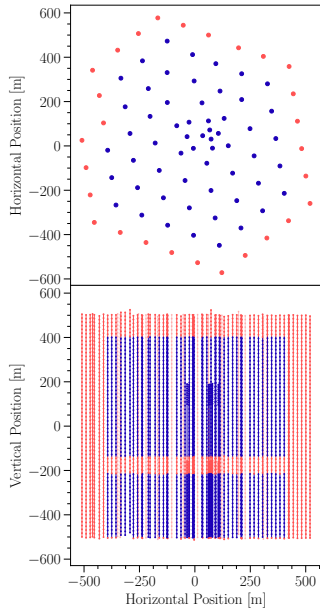


Figure 1.3: The top view (above) and side view (below) display the veto DOMs and the DOMs within the fiducial volume for HESE. DOMs highlighted in red represent the veto region, while those in blue define the fiducial volume. Events where the initial detected light comes from the veto region are excluded from the analysis. Figure taken from [19].

[20]: Aartsen et al. (2013), *Evidence for High-Energy Extraterrestrial Neutrinos at the IceCube Detector*

[19]: Abbasi et al. (2021), *IceCube high-energy starting event sample: Description and flux characterization with 7.5 years of data*

[21]: Abbasi et al. (2022), *Detection of astrophysical tau neutrino candidates in IceCube*

is that each detector systematic parameter continuously varied while generating the MC events, as visualized in Figure 1.2. Using the SnowStorm method, one obtains a single MC set representing all variations in the detector response. This can help an analysis by reducing the bookkeeping effort necessary for using multiple discrete sets, studying variations in a large number of detector systematic parameters at once without loss in statistics, and allowing analyses of different event selections to use the same MC set and "marginalize" over all detector systematic parameters that are not relevant for a single analysis.

The analysis presented in this thesis uses simulations generated using this aforementioned novel method. It involves uniform and independent sampling distributions for all relevant parameter uncertainties in the flavor analysis. These simulations cover all three flavors of neutrinos and were created using the SPICE-3.2.1 icemodel. They were designed for general use and were also utilized by several other IceCube analyses simultaneously, see [17] and [18] for details. The simulation sets were developed for primary neutrinos in the energy range of $E_\nu = [100 \text{ GeV} - 1 \text{ PeV}]$ assuming a single power law of $E_\nu^{-1.5}$, and in the range $[1-100 \text{ PeV}]$ with a E_ν^{-1} spectrum. The harder spectrum is generally chosen, particularly for higher energy datasets, to ensure a sufficiently large number of events at those energies. Using the weighting method described previously, one can reweight the neutrino events to match any desired spectrum.

1.2 High Energy Starting Event (HESE) sample

The High Energy Starting Events (HESE) selection is a comprehensive, all-sky, all-flavor sample of astrophysical and atmospheric neutrinos observed in IceCube. This selection process led to IceCube's first significant milestone: the discovery of an astrophysical neutrino flux [20]. Subsequently, a particle identifier was developed using this sample with added years of data, eventually finding two tau neutrino candidates in IceCube [19, 21]. For the analysis presented in this thesis, this sample was again used, along with some updates in Self-Veto calculations, that shall be introduced in Section 1.2. The concept behind HESE is to establish a veto region on the detector's outer edges to select only events where the initial Cherenkov photons are detected inside the fiducial volume. As shown in Figure 1.3, the veto region includes the outer strings, a top layer of 90 m, a central layer of 80 m around the dust layer, and a 10 m bottom layer. The very thicker veto at the top is essential for filtering out atmospheric muons entering from above. However, the veto can be thinner at the bottom of the detector since up-going atmospheric muons do not exist. The inclusion of a veto around the dust layer is crucial, as horizontal events passing through this highly absorptive region can mimic starting events. To pass the veto, events must deposit fewer than 3 photoelectron (PE) in the veto region out of the first 250 PE recorded within the fiducial volume, and a minimum total charge of 6000 PE is required to ensure high-energy events are selected.

The HESE selection is particularly powerful due to its simplicity, as it does not rely on complex reconstructions, making it robust against changes in filtering or reconstruction algorithms. The fact that it is an all-flavour

sample, can help break degeneracies caused by different neutrino flavors producing similar event patterns. Additionally, the all-sky nature of HESE allows for the study of the zenith distribution of events, which can distinguish between atmospheric and astrophysical neutrinos. However, HESE does have limitations: the high-energy threshold introduces uncertainty in estimating background contributions and astrophysical parameters, and the veto region reduces the detector's effective volume. An extension of HESE to lower energies, known as Medium Energy Starting Events (MESE), has been developed [22] (and recently updated [23]) to overcome some of these limitations.

Despite of rejecting a significant fraction of atmospheric background, HESE retains the majority of astrophysical neutrinos within its fiducial volume. The neutrino effective area of the HESE sample, increases with neutrino energy due to the larger amount of visible light deposited (see Figure 1.11). At energies above a few hundred TeV, the effective areas become similar across all flavors, except the Glashow resonance of $\bar{\nu}_e$ at 6.3 PeV. However, at lower energies, the effective area varies by flavor due to differences in energy deposition during charged-current interactions, with electron neutrino interactions producing the highest effective area due to the nearly complete energy deposition in electromagnetic and hadronic cascades. For different zenith angles, the effective area decreases as the zenith angle increases, particularly in the up-going region at high energies. This is a result of Earth absorption, which becomes significant for neutrinos above approximately 1 PeV. The distinction between tau neutrinos and other flavors at the highest energies is due to the phenomenon of tau regeneration, where the tau neutrino regenerates after the decay of a tau lepton. Muon neutrino interactions, on the other hand, produce muons that deposit only part of their energy before escaping the detector, resulting in a higher detection threshold. Neutrino interactions, especially for ν_τ , exhibit effective areas between those of ν_μ and ν_e .

Atmospheric Neutrino Self-Veto

As mentioned in Section ??, high-energy cosmic ray showers produce many neutrinos and muons, which are the only particles able to reach underground detectors such as IceCube. When atmospheric neutrinos reach the detector, they are typically accompanied by other particles from the same CR shower, mostly muons. The chance of a detectable muon accompanied with an atmospheric neutrino is called **the atmospheric self-veto probability**. Several things affect this probability, such as the type, energy, and direction of the neutrino. In the case of high-energy CR showers, some muons may reach the detector and *trigger* the veto that marks the event as background. The likelihood of rejecting an atmospheric neutrino through this self-veto mechanism increases with higher neutrino energy and more vertical shower angles. With such a modelling, one effectively suppresses the flux of atmospheric neutrinos, in down-going region⁴. **The passing fraction** of atmospheric neutrinos—defined as the fraction that is not accompanied by a detectable muon from the same CR shower—varies with both neutrino energy and zenith angle [24]. It tends to increase at larger zenith angles, as muons must travel farther through the atmosphere to reach IceCube, as shown in Figure

[22]: Aartsen et al. (2015), *Atmospheric and astrophysical neutrinos above 1 TeV interacting in IceCube*

[23]: Basu et al. (2023), *From PeV to TeV: Astrophysical Neutrinos with Contained Vertices in 10 years of IceCube Data*

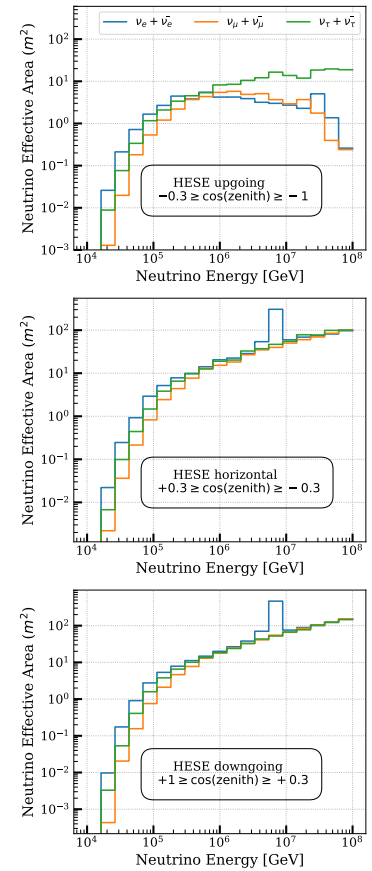


Figure 1.4: The neutrino effective areas for the high-energy starting event selection as a function of neutrino energy. The distributions are shown for all neutrino flavors, broken down by various zenith angle ranges.

4: This process only applies to downward-moving atmospheric neutrinos because muons cannot reach IceCube from below the Earth

[24]: Argüelles Delgado et al. (2018), *Unified atmospheric neutrino passing fractions for large-scale neutrino telescopes*

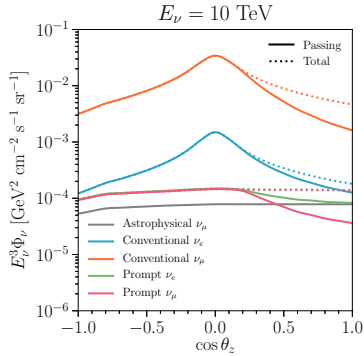


Figure 1.5: The Atmospheric neutrino fluxes at $E_\nu = 10$ TeV. The plot shows the fraction of the flux that is **not** vetoed, known as **passing fluxes** (solid lines), alongside the total flux entering the detector (dashed lines) as a function of the cosine of the zenith angle. Figure is adapted from [24].

[24]: Argüelles Delgado et al. (2018), *Unified atmospheric neutrino passing fractions for large-scale neutrino telescopes*

[25]: Yuan et al. (n.d.), *nuVeto*

[26]: Fedynitch et al. (2015), *Calculation of conventional and prompt lepton fluxes at very high energy*

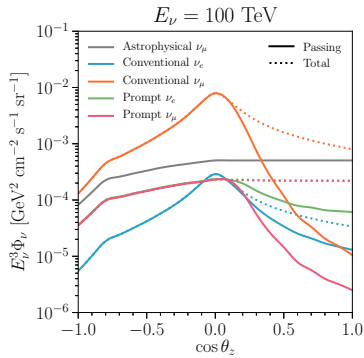


Figure 1.6: The atmospheric neutrino fluxes and the effect of self-vetoing are displayed for a neutrino energy level of $E_\nu = 100$ TeV, see caption of Figure 1.5. Figure taken from [24].

[27]: Aartsen et al. (2014), *Energy Reconstruction Methods in the IceCube Neutrino Telescope*

[14]: Whitehorn et al. (2013), *Penalized splines for smooth representation of high-dimensional Monte Carlo datasets*

[13]: Usner (2018), *Search for Astrophysical Tau-Neutrinos in Six Years of High-Energy Starting Events in the IceCube Detector*

5: to account ice layer tilt and anisotropy due to birefringence (see Section ?? for details) separately

[28]: Yuan (2023), *Detecting neutrinos in IceCube with Cherenkov light in the South Pole ice*

1.5. At neutrino energies greater than 100 TeV, the contribution from astrophysical neutrinos begins to outweigh the atmospheric background, improving IceCube’s ability to detect astrophysical neutrinos as indicated in Figure 1.6.

The passing fractions used in the analysis presented in this thesis is based on the calculations derived in [24] a formalism used in 7.5 years of HESE analysis [19] through the *nuVeto* package [25]. The previously used calculations are further updated using *MCEq* package, *MCEQ*, a tool designed to solve the cascade equations governing cosmic ray-induced showers, allowing for more precise and computationally efficient predictions of atmospheric lepton fluxes [26].

1.3 Maximum Likelihood Event Reconstruction

With the aforementioned HESE sample, next step is to infer the properties of these events—primarily energy, direction, and the deposited light pattern (morphology). To do so, it is necessary to *reconstruct* each individual event. The reconstructed properties are then used to create probability density functions (PDFs) that facilitate likelihood fits for making the desired physics measurements (as outlined in Section 2.1). Therefore, it is crucial to reconstruct the event properties as accurately as possible. The analysis presented here utilizes a maximum-likelihood estimation (MLE) approach, called *millipede* for event reconstruction.

millipede aims to maximize the likelihood of the observed light pattern from an event, given a specific source hypothesis. The input data comprises individual pulses detected by Digital Optical Modules (DOMs), expressed in terms of charge (measured in photoelectrons (PEs)) and time. These pulses are deconvolved from the digitized waveforms using established single-photoelectron (SPE) pulse templates. The likelihood function compares the observed data to the expected data for a given hypothesis and adjusts the parameters to maximize this likelihood, details of which can be found in [27].

The expected number of photons detected at DOM j follows a Poisson distribution characterized by a mean $\lambda_j = \Lambda_j E$, where Λ_j represents the expected photon yield from a 1 GeV cascade at DOM j , and E signifies the cascade’s energy, stored in tabulated form as photo splines [14], which were originally developed and used in an analysis similar to one presented in this thesis [13] and now have been updated with newer *icemod*⁵ [28] *. The likelihood of detecting k_j photons at DOM j for a cascade with energy E is given by:

$$L_j = \frac{(E\Lambda_j)^{k_j} e^{-E\Lambda_j}}{k_j!} \quad (1.4)$$

By taking the logarithm and summing over all DOMs, including noise hits ρ_j , along with an expansion to include multiple light sources i and timing information, the log-likelihood can be expressed as:

* These updated tables are used in the analysis presented in this thesis

$$\ln L = \sum_{i,j,t} (k_{jt} \ln(E_i \Lambda_{ijt} + \rho_{jt}) - (E_i \Lambda_{ijt} + \rho_{jt}) - \ln(k_{jt}!)) \quad (1.5)$$

The hypothesis to be compared encompasses the event parameters $(x_s, y_s, z_s, t_s, \theta_s, \phi_s, E_s)$, which define the source's location, time, direction, and energy respectively.

`millipede` offers a comprehensive set of configurations that allow users to define how photons are organized in terms of time bins, the magnitude of changes in various parameters, and the exclusion of specific modules from the likelihood calculation. One crucial aspect of these settings is the selection of an ice model for data reconstruction. This model plays a vital role in predicting the expected number of photons that will reach a DOM based on variables such as distance and direction from the source. Additionally, the ice model can influence the timing information of these photons [29], which is critical for accurate event reconstruction.⁶ As for exclusions of certain modules, **bright DOMs** and **Saturated DOMs** are excluded from the likelihood fit because they may introduce bias by contributing excessively to Equation 1.5. These particular DOMs generally account for a significant portion of the total observed charge. Hence, bright and saturated DOMs along with other DOMs that may have failed during the Run are generally labelled as *Bad DOMs* and are collectively excluded from the reconstruction. `millipede` framework helps reconstruct single and double cascades, along with track source hypotheses. Although they all use the same likelihood from Equation 1.5, they each have different ways to define sources. The hypothesis that fits the observed data best is found by comparing maximum likelihood values, which gives an idea of the interaction type in the detector.

monopod: `monopod` does a simple one-particle cascade energy fit, in other words it assumes a single light source. It minimizes parameters such as the cascade's deposited energy, neutrino direction (azimuth and zenith), cascade vertex position (x, y, z) , and vertex time, represented as, $\vec{h} = (x, y, z, t, \theta, \phi, E)$ [4]. The reconstructed vertex here refers to the shower maximum, which is the peak of the longitudinal energy loss profile and is typically displaced from the interaction vertex by several meters in the considered energy range.

taupede: The double cascade fitting algorithm, `taupede`, maximizes the likelihood of two energy depositions with energy E_1 and E_2 respectively, separated by distance L_{dc} . The second cascade's direction matches the first, and its vertex is determined by the first cascade's vertex, direction, and double cascade length L_{dc} . The parameters for the double cascade hypothesis are $\vec{h} = (x_1, y_1, z_1, t_1, \theta, \phi, E_1, L_{dc}, E_2)$, with the tau traveling in the same direction as the incoming neutrino due to Lorentz boosting. The light yield and timing at each Digital Optical Module (DOM) are compared with expected values from the two energy depositions. For the second cascade's timing, the conditions are $|\vec{x}_2 - \vec{x}_1| = L_{dc}$, $t_2 - t_1 = cL_{dc}$ ⁷.

mumillipede: Track-like events are parameterized as multiple cascades along its path. The total deposited energy is given by $E_{dep} = \sum_k E_k$. Although the deposited energy is not a reliable indicator of the primary neutrino energy, the parameters related to direction and time are vital for neutrino point-source searches.

Bright DOM

A Bright DOM generally refers to a situation where a high energy event occurs close to a string, and in first pulse itself, a large amount of charge is observed. Emperically, this *large amount of charge* is assumed to be 10 times the average observed charge of the event.

Saturated DOM

A DOM is considered saturated if its PMT reaches saturation. This can happen if an event occurs close to a string or a very high energy interaction occurs, producing many photons that gets collected by the PMT. These DOMs generally don't have a *complete* digitized waveforms, making them unsuitable to be used in likelihood based reconstruction.

[29]: Abbasi et al. (2024), *In situ estimation of ice crystal properties at the South Pole using LED calibration data from the IceCube Neutrino Observatory*

6: Different approaches to model the ice at the South Pole can significantly affect the reconstructed properties of an event, in particular the double cascade reconstruction using `taupede` (see Section 1.5 at the end of this chapter for such detailed checks)

DeepCore DOM exclusion

DeepCore DOMs have traditionally been excluded from high-energy reconstruction methods like `millipede` because it uses spline tables that assume a uniform single photoelectron (SPE) template for all DOMs. However, the higher quantum efficiency of DeepCore DOMs results in significantly different charge collection, meaning their SPE templates differ from those of other DOMs. Recent efforts have updated simulations to address this issue (as will be discussed in Section ??).

[4]: Santen (2014), *Neutrino Interactions in IceCube above 1 TeV: Constraints on Atmospheric Charmed-Meson Production and Investigation of the Astrophysical Neutrino Flux with 2 Years of IceCube Data taken 2010–2012*

7: assuming tau travels through the ice at the speed of light c .

8: All algorithms are run multiple times, starting with a provided `seed`, where each subsequent iteration uses the output from the previous one, as explained in Section 1.4.

[13]: Usner (2018), *Search for Astrophysical Tau-Neutrinos in Six Years of High-Energy Starting Events in the IceCube Detector*

The algorithm outlined above relies on the quality of the seed, which serves as the initial hypothesis \vec{h}_0 . This seed is adjusted until a satisfactory match is achieved between the expected and actual light yield. This process has proven challenging, especially in the case of `taupede`, where the seed combines aspects of both a cascade and a track. Locating an appropriate seed is difficult, and the reconstruction process is influenced by the choice of seed. To reduce this influence, one can either modify the seed or increase the number of iterations⁸; however, both approaches result in greater computational expenses. To tackle the challenges associated with reconstructing double cascade events, an improved method for implementing the `taupede` fit was developed [13]. This method effectively converts the fitting process into a *brute-force* approach, where multiple hypotheses are explored and evaluated.

Simple reconstruction methods like **LineFit** and **SPEFit** provide fast initial estimates for event properties. These methods use limited event information, such as the first photon arrival time or total photoelectrons, without relying on detailed ice properties. The results are then used as seeds for more refined algorithms like `millipede`. For cascade-like events, simpler MLE methods are used to find a charge-weighted mean position of the source, providing an efficient first estimate.

1.4 Particle Identification of High Energy Neutrinos

Event reconstruction is performed using the aforementioned `millipede` framework, which enables the identification of different interaction types by assigning a **particle identifier (PID)** to each reconstructed event. The PID provides the probability that an event corresponds to a particular type of interaction. A **ternary topology identifier** has been developed (initially developed in [13] and later used to find first two tau candidates in IceCube [21]) based on the three event topologies—single cascade, double cascade, and track. By using these IDs, Monte Carlo templates are constructed to extract the contribution fractions from each neutrino flavor (see Chapter 2).

[21]: Abbasi et al. (2022), *Detection of astrophysical tau neutrino candidates in IceCube*

The analysis presented in this thesis has two main goals: to identify double cascades produced by tau neutrinos and to determine the flavor composition of astrophysical neutrinos. Given the complexity of detecting double cascades and the susceptibility of the reconstruction algorithm to failures and dependence on the initial seed hypothesis, the classification process uses a combination of algorithms offered by the `millipede` framework, which run in parallel on each of the HESE events that provides likelihood for the three event morphologies.

As mentioned before, these methods are `seed` dependent, hence to start with, all selected HESE events are reconstructed using first-guess algorithms to determine their vertex and direction. Result of these quick methods provides an initial fit for the event’s position and trajectory, serving as a seed for `monopod`, which performs a fit with four iterations.

Generating a reliable seed for `taupede` is more complex. Multiple seeds are constructed using the `monopod` fit and generated with varying

lengths (10, 25, 50, and 100 meters), each shifted forward, backward, or centered along the direction of the seed in bruce-force way [13]. An amplitude-only *taupede* fit is performed for each of the 12 seeds⁹, and the three best-performing seeds are selected for a full fit, performing 4 iterations of fits again, which incorporates photon arrival times at the Digital Optical Modules (DOMs). This method accounts for the diverse photon arrival patterns produced by scattered photons in single energy depositions [30]. The tracks are reconstructed using the *SPEFit* algorithm, which iteratively (16 times) fits a track based on the first photoelectron detected at each DOM. Although the *mumillipede* algorithm could also reconstruct tracks, it is computationally intensive, so *SPEFit* is preferred. Finally, *mumillipede* unfolding is performed along the directions determined by each topology fit (*monopod*, *taupede*, and *SPEFit16*), allowing for a comparison of likelihood values for each hypothesis. The best fit is selected for final classification based on the highest likelihood value.

Since identifying tau-induced double cascades is main goal of this process, the comparisons of the three likeelihoods is not the only proxy by which the classifier selects a double cascade event. First, the *taupede* fit is vetted through **Quality Criteria**, on the basis of containment, and reconstructed properties. If these criteria are satisfied¹⁰, further classification is performed using additional selection criteria based on observables derived from reconstructed quantities, described below:

The reconstructed direction of a particle is indicated by its zenith and azimuth angles. The azimuthal angle is not useful for distinguishing between atmospheric and diffuse astrophysical neutrino fluxes since both are isotropically distributed. However, it is important for addressing systematic uncertainties in reconstructed track length due to anisotropic light scattering in the ice. However, zenith angle provides a reliable estimate of the neutrino's initial trajectory, especially for tracks, which can be reconstructed more accurately than cascades.

The total deposited energy (E_{tot}) refers to the visible energy in the detector, calculated as the sum of all contained energy losses along the best-fit hypothesis. The total deposited energy serves as a lower limit for neutrino energy and is used as a direct observable in the likelihood fit (see Section 2.2.2). Not all energy is deposited in the detector; some may be carried away by secondary neutrinos from tau decays or by muons that leave the detector, while some energy may remain invisible during hadronic showers. Therefore, the sensitivity of total deposited energy to primary neutrino energy varies by event morphology. In single and double cascade topologies, the initial energies of electron and tau neutrinos can be constrained more accurately than those of muon neutrinos, as muon usually leaves the detector and also the energy losses are stochastic, making the proxy weaker.

The Reconstructed length (L_{reco}), represents the distance between two cascades in double cascade events, is a critical observable for tau-neutrino interactions.

The energy asymmetry (E_A) measures the distribution of deposited energy between the two cascades in a double cascade event. It is defined as,

$$E_A = \frac{E_1 - E_2}{E_1 + E_2} \quad (1.6)$$

[13]: Usner (2018), *Search for Astrophysical Tau-Neutrinos in Six Years of High-Energy Starting Events in the IceCube Detector*

9: 4 length seeds shifted 3 times, giving total of 12 seeds

[30]: Stachurska (2020), *Astrophysical Tau Neutrinos in IceCube*

Quality Criteria for *taupede* fit

The final-best fit of *taupede* is accepted only if all the following criteria are satisfied:

taupede Fit is converged
Energies of both of the fitted cascades $E_1, E_2 \geq 1 \text{ TeV}$
Both cascades are *softly* contained
(vertex $\leq 50 \text{ m}$ outside detector)
Opening angle between *taupede* and *mumillipede* fit $\leq 30^\circ$

10: If any of the quality checks are failed, the event is assigned track or cascade morphology depending on which of the fit's likelihood is higher.

Direction definitions in IceCube

The *zenith angle* (θ) gives the direction of particle origin with respect to the vertical axis that points towards the surface of the ice and upward from the South Pole.

A zenith angle of 0° indicates a particle moving directly downward in the detector, 90° corresponds to horizontal propagation, and 180° signifies a particle moving directly upward.

The *azimuth angle* (ϕ) gives the direction of particle origin with respect to the horizontal x-axis of the IceCube coordinate system (see Section ??)



Figure 1.7: A sketch of energy asymmetry, it is a measure of the relative distribution of total deposited energy between the two cascades, as defined in 1.6. Sketch is adapted from [13].

11: since there is no second energy deposition technically, $E_2 = 0$ for a true single cascade

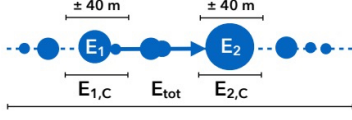


Figure 1.8: A sketch of Energy Confinement, it is a measure of how confined are reconstructed energy depositions E_1 and E_2 are within their reconstructed vertices. The confinement, as shown in the sketch is checked within 40 m of the vertices. Sketch is adapted from [13].

classification Criteria Based on Reconstructed Quantities

After meeting Quality requirements, an event is classified as,

a track if $E_C < 0.99$

a single cascade if $E_C \geq 0.99$ and ($E_A < -0.98$ or $E_A > 0.3$ or $L_{\text{reco}} < 10$)

a double cascade if $E_C \geq 0.99$ and $-0.98 \leq E_A \leq 0.3$ and $L_{\text{reco}} \geq 10$

where E_1 and E_2 are reconstructed energies of the first and the second cascades. A *true*[†] single cascade has an energy asymmetry of 1¹¹, while a double cascade can have any value between -1 and 1, depending on the kinematics of the neutrino interaction. This variable hence, is an excellent estimator to distinguish between a single and a double cascade.

The energy confinement (E_C) measures how much of the total energy is localized near the cascade vertices. It uses the two cascade vertices fitted by $\tau_{\text{aupe}}d$ and deconvolves the energy depositions within 40 m of each of them. It is defined as,

$$E_C = \frac{E_{1,c} + E_{2,c}}{E_{\text{tot}}} \quad (1.7)$$

where, $E_{1,c}$ and $E_{2,c}$ are the deconvolved energy depositions within 40 m distance of first and second cascades respectively and E_{tot} is the total deposited energy as defined above. Note that from Equation 1.7, $E_C = 1$ (with $E_{1,c} + E_{2,c} = E_1 + E_2 = E_{\text{tot}}$) for a $\nu\mu\tau$ induced double cascade, as opposed to tracks which have energy depositions outside the region around the double cascade vertices. It is therefore a suitable estimator to separate single cascades and double cascades from tracks,

The classification chain uses several variables to categorize events into three morphologies. If the $\tau_{\text{aupe}}d$ fit meets all the quality criteria, a series of selection cuts is applied. If the event passes all these cuts, it is classified as a double cascade, as illustrated in Figure 1.9. Initially, only high-energy starting events (HESE) with a total energy $E_{\text{tot}} \geq 60$ TeV are selected to almost entirely eliminate atmospheric muons. If the quality criteria fail based on the likelihood value, the event is assigned either a single cascade or track morphology. The next step ensures that the reconstructed length $L_{\text{reco}} \geq 10$ m. This condition is necessary because while a double cascade with a length below this threshold could be genuine, the resolution of the reconstruction algorithm does not allow for a definitive classification. Therefore, if the length is below 10 meters, the event is classified as a single cascade. As stated before, cuts on E_A and E_C are applied afterward to further filter out single cascades and tracks from the double cascade samples, respectively. Notably, after the quality cut, it is assumed that the event is a double cascade until any of the selection criteria based on reconstructed properties fail.

A noteworthy point is that none of the events in the HESE sample, with $E_{\text{tot}} \geq 60$ TeV, are discarded. They are only separated into three sub-samples based on their tagged morphology. All the cuts and selection criteria introduced so far were determined by evaluating the signal-to-background ratio in the distributions of these variables [13]. The cut values were not strictly enforced to allow for some background contribution in the final sample. The rationale behind this selection is that the analysis performed using these three sub-samples is a forward-folding fit (see Section 2.1). This analysis employs Monte Carlo PDFs that utilize the shapes of signal and background distributions to compare them with data events. Therefore, it is essential to have a sufficient amount of background simulation present in the sample.

[13]: Usner (2018), *Search for Astrophysical Tau-Neutrinos in Six Years of High-Energy Starting Events in the IceCube Detector*

[†] *true* event morphologies are assigned by going through produced charged particles at Secondary Charged Particle Propagation stage of the simulation chain (see Section 1.1.1). Looking at the type of particles, their energy depositions and positions within the detector volume, a morphology is assigned to the event.

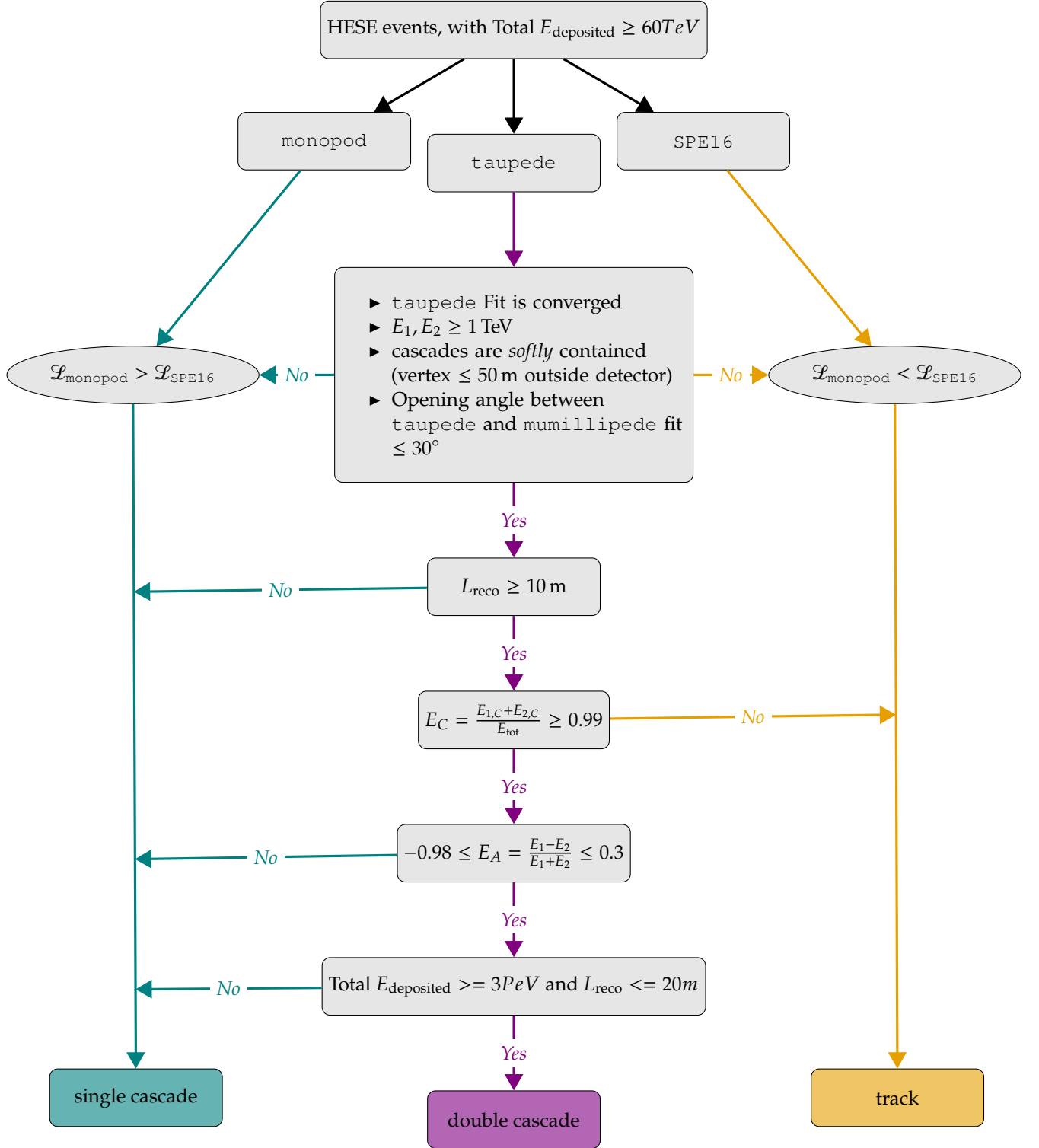


Figure 1.9: The event classification scheme for the Ternary PID. The first level evaluates reconstruction quality; if the criteria are not met, events are classified as single cascades or tracks based on the likelihood values $\mathcal{L}_{\text{monopod}}$ and $\mathcal{L}_{\text{SPE16}}$. The second level considers the reconstructed length, using a threshold below which distinct vertices of double cascades appear as a single cascade. The third and fourth levels focus on energy confinement and energy asymmetry, respectively. The last level is added to improve purity of the double cascade sample at high energies where misclassification is prominent due to glashow events.

So far, all the explained sample selection and Ternary classification has been taken (with updates in simulations and reconstruction tables) as it was done and used in previous iterations of HESE flavour measurements

[13]: Usner (2018), *Search for Astrophysical Tau-Neutrinos in Six Years of High-Energy Starting Events in the IceCube Detector*

[30]: Stachurska (2020), *Astrophysical Tau Neutrinos in IceCube*

The Sampling correction here refers to changing the weight of the simulated neutrino, and not changing the HESE sample itself. The weight of a simulated neutrino, as discussed in Section 1.1 takes into account various probabilities, such as interaction type, propagation through earth etc. Most of these probabilities are derived from underlying theoretical models of particle interactions [31]. The correction applied here refers to updates in calculations of these models that affects shape of the underlying cross-section and kinematics of the interactions, that may result in difference in reconstructed variable distributions.

[32]: Glashow (1960), *Resonant Scattering of Antineutrinos*

[13, 30]. For the analysis presented in this thesis, some changes were made both in **sampling** and classification schemes that are discussed in the following subsections.

1.4.1 Reclassification of PeV Double Cascades

The Double Cascade sample is crucial for flavor measurement, necessitating a more comprehensive assessment. Using the ternary classification described, the **Flavour Purity** of this sample can be determined. Flavour purity is defined as the fraction of a *desired* neutrino flavor within a given morphology sample. This concept is illustrated in Figure Figure 1.10, which displays the reconstructed energy distribution of the Double Cascade sample for each neutrino flavor. Ideally, one would want that each bin in this plot reflects a 100% contribution from the ν_τ flavor. While it does not achieve 100%, it is evident that the Double Cascade sample is predominantly made up of ν_τ events across the energy range. However, a rapid decrease in purity is observed at high energies (around 6 PeV), where the sample becomes dominated by ν_e events (see the left panel of Figure Figure 1.10). This shift is due to the Glashow resonance of $\bar{\nu}_e$, which significantly influences the cross-section of neutrino interactions at these energies [32]. These events are categorized as Double Cascades because of their high energy deposition over a short distance, but they are misclassified as single cascades.

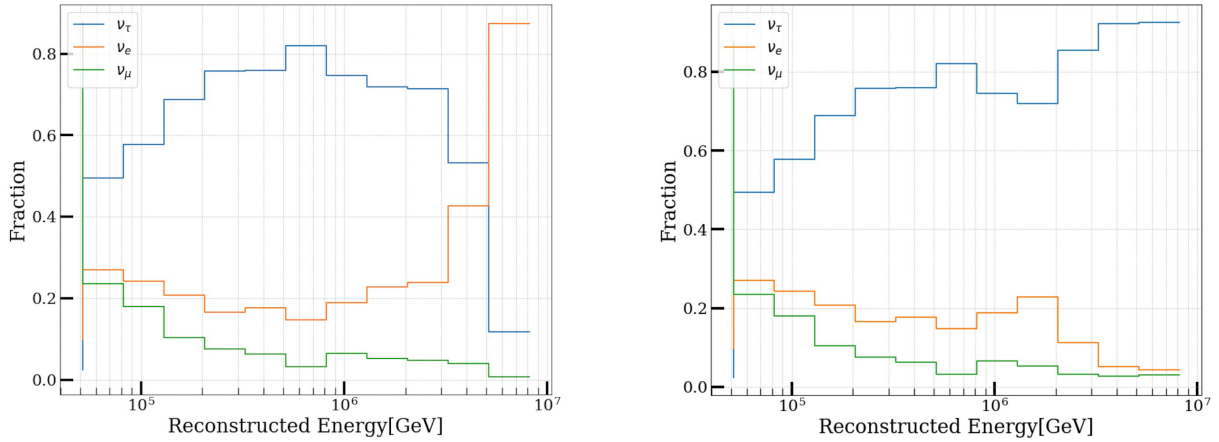


Figure 1.10: Fraction of flavor content per bin in double cascade events. The left panel shows the distribution without the criteria of Total $E_{\text{deposited}} \geq 3$ PeV and $L_{\text{reco}} \leq 20$ m, indicating *purity contamination* at high energies from $\bar{\nu}_e$ Glashow events. The right panel presents the distribution after reclassifying double cascades as single cascades under these conditions.

To address this, a **reclassification** mask was introduced at the end of the classification chain outlined in Figure Figure 1.9. If an event is classified as a Double Cascade with a reconstructed energy of $E_{\text{tot}} \geq 3$ PeV and a reconstructed length $L_{\text{reco}} \leq 20$ m, it is reclassified as a single cascade. These thresholds were chosen based on the purity distribution to maximize the signal-to-background ratio, even at these energies. The distribution before and after applying this mask is shown in the right panel of Figure Figure 1.10. As anticipated, the lower energy distributions remain nearly identical, while purity is restored at higher energies. It is important to note that the fraction of ν_μ remains unchanged in both figures, due to the involvement of only electron neutrinos—technically electron anti-neutrinos—in Glashow interactions, which contribute to

the purity contamination. Since this is merely a reclassification, the total High-Energy Starting Event (HESE) sample remains unchanged.

1.4.2 Tau Polarisation

As discussed in ??, ν_τ -CC interaction always produces a tau lepton, which has various decay modes. The tau lepton produced in this interaction is polarised, which can significantly alter the kinematics of the tau decay [33, 34]. Whether the decay mode is leptonic or hadronic, the fraction of energy going to the decay products ($\frac{E_{\text{hadrons/leptons}}}{E_\tau}$), is affected if non-zero tau Polarisation is not taken into account. The PRPOSAL software used in simulation presneted in this thesis, to simulate secondary charge particle production, propagation and energy losses does not take into account this factor. That is, the Taus produced in a ν_τ -CC interaction is assumed to be produced with no polarisation. Since, the signature which is used for identification of this analysis relies on both, the neutrino interaction cascade and tau decay cascade, not taking in account this correction can lead to an *incomplete* simulation of energy loss profiles. Mainly the energy reconstruction of the second decay cascade, may get affected, which can further alter the Energy asymmetry (E_A) of the event, which is used as a selection variable in Ternary Classifier (see Figure 1.9).

The idea is to test the impact of tau polarisation on analysis variables by reweighting the monte carlo events. The calculations provided in [33], are used to get theoretical fractional energy loss of the electromagnetic equivalent visible energy losses, for both polarised and unpolarised states. The ratio of this is multiplied with the simulated fractional energy (which assumed unpolarised taus), to get a new reweighting factor. The change introduced minor difference in the overall observable distributions, hence this was left as a weight correction only and no further analytical checks were performed.

1.4.3 Glashow Cross-Section correction

The resonance enhancement of $\bar{\nu}_e e^-$ scattering at an energy of approximately 6.3 PeV, known as the *Glashow resonance*, was discussed in Section ??. The cross-section for this process at this energy is significantly larger—about two orders of magnitude greater—than that of Deep Inelastic Scattering (DIS). Since this energy range is relevant to the thesis presented in this work, it is crucial to consider second-order QCD corrections, which can significantly alter the Glashow cross-section [35].

The corrections applied to the cross-section, as described in [35], include *Initial State Radiation (ISR)* [36, 37] and the *Doppler broadening effect* [38]. ISR becomes more prominent when the center of mass (COM) energy of the system is much higher than the mass of the initial lepton—since W^- is substantially more massive than e^- , this leads to an enhancement factor of approximately $\frac{M_W}{m_e} \sim 12$ in radiation, on top of contributions from the fine structure constant (α). This results in collinear photon emission. Doppler broadening occurs due to the motion of atomic electrons, where the typical velocity of the electron is assumed to be close to the speed of light. This motion causes the COM energy to shift by a factor of

[33]: Garg et al. (2023), *Neutrino propagation in the Earth and emerging charged leptons with nuPyProp*

[34]: Argüelles et al. (2022), *Tau depolarization at very high energies for neutrino telescopes*

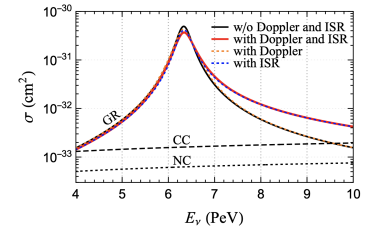


Figure 1.11: The cross section for the Glashow resonance process $\bar{\nu}_e + e^- \rightarrow W^- \rightarrow X$ is shown with and without initial state radiation and Doppler broadening. The black curve represents the cross section without these effects, the blue dotted curve includes initial state radiation, the orange dotted curve shows Doppler broadening, and the red curve combines both effects. Figure taken from [35].

[35]: Huang et al. (2023), *Inferring astrophysical neutrino sources from the Glashow resonance*

[36]: Garcia et al. (2020), *Complete predictions for high-energy neutrino propagation in matter*

[37]: Gauld (2019), *Precise predictions for multi-TeV and PeV energy neutrino scattering rates*

[38]: Loewy et al. (2014), *The Effect of Doppler Broadening on the 6.3 PeV W^- Resonance in $\bar{\nu}_e e^-$ Collisions*

[27]: Aartsen et al. (2014), *Energy Reconstruction Methods in the IceCube Neutrino Telescope*

[39]: Chirkin et al. (2013), *Evidence of optical anisotropy of the South Pole ice*

12: Technically it coincides within 1° of the ice flow axis, hence this axis was given a special name, *the anisotropy axis*. The axis along which scattering is reduced is called *the major anisotropy axis* and the one perpendicular to it where scattering is enhanced is known as *the minor anisotropy axis*.

While the SpiceBfr model agrees much better with the data, compared to Spice-3.2.1, it is important to note that on the analysis level, where one uses reconstruction algorithms based on all of the pulse information from the DOMs, the ever so significant effects on charge and time level may get smeared off from overall observable distributions. Going from Spice-mie to Spice-Lea was a breakthrough as the former did not consider this anisotropic behavior of photon propagation. But going from Spice-3.2.1 to Spice-Bfr was more in the direction of inherent modeling of the ice (crystal) property, to explain the anisotropy, while Spice-3.2.1 and Spice-Lea used an approximated solution in the form of effectively mimicking an anisotropic scattering of photons.

[13]: Usner (2018), *Search for Astrophysical Tau-Neutrinos in Six Years of High-Energy Starting Events in the IceCube Detector*

13: This icemodel is almost identical to the one used in previous iteration of this analysis [30]

$(1 - \beta \cos \theta)$, where θ is the angle between the electron's velocity (β) and the incoming neutrino in the lab frame [38].

The combined results of these effects, based on calculations from [35], were used to adjust the *total weight* of neutrinos. As noted in [35], these effects are smoothed out by the energy resolution of IceCube [27], and the impact of this reweighting on energy distributions and sensitivity was negligible. Nevertheless, the reweighting was retained, similar to the correction for Tau polarization.

1.5 Influence of South Pole Ice properties on Double Cascades Reconstruction

The identification of ν_τ -induced double cascades in the IceCube detector faces significant systematic uncertainties due to the anisotropy of the ice. As discussed in Section ??, the Anisotropy at the south pole ice has been established since 2013 [39]. This phenomenon causes photons to have a directional dependence while scattering, with enhanced scattering occurring perpendicular to the ice flow axis¹² and reduced scattering along it.

Such a direction dependednt scattering pattern can cause a bias in reconstructing specifically a double cascade event using `taupede`, as this algorithm looks for energy depositions around vertices along a given seed direction (see Section 1.4), which can cause bias in length reconstruction. When a single cascade aligns with this major anisotropy axis, reduced scattering can elongate its apparent size, mimicking double cascade characteristics due to altered light timing at the DOMs. Conversely, if a true double cascade aligns with one of the minor anisotropy axes, it may be compressed, increasing the risk of misidentification as a single cascade. Without accounting for anisotropy, true single cascades could be misclassified as double cascades, while genuine double cascades along minor axes might be missed.

Reconstructing these events relies on photo-spline tables introduced in Section 1.3, which provide tabulated light yields for simulated 1 GeV cascades. These cascades are placed in the detector's center at intervals of $\Delta z = 20$ m, between depths of -600 to 600 m and zenith angles from 0° to 180° . The initial model primarily considers the ice layer's depth and zenith angle for light propagation, but an additional azimuthal dimension was necessary to account for anisotropy. A key advancement was the development of **the effective distance spline tables**, which adjusted for anisotropy by using an isotropic-ice-equivalent position instead of position of the DOMs to look-up for the light yield, which resulted in a significant enhancing of length reconstruction accuracy [13].

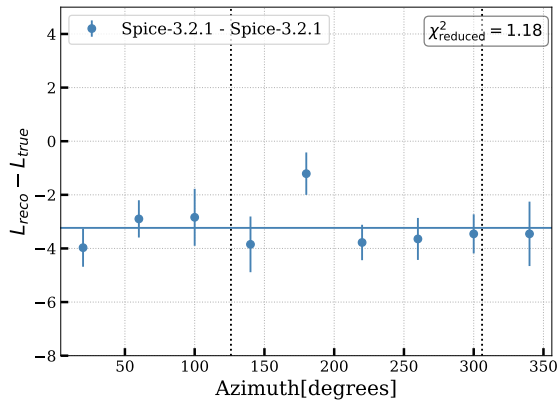
Recent developments in icemodel studies have revealed that the directional behavior of light in ice, is due to its molecular structure, a phenomenon known as *birefringence* as already introduced in Section ??. This is now incorporated into the new ice model, called as, **SpiceBfr**. However, during the development stage of the analysis presneted in this thesis, the only large-scale Monte Carlo simulations available was the one produced using an earlier icemodel, **Spice-3.2.1**¹³. Naturally, the question

Table 1.1: The four comparison scenarios that were analyzed. The First icemodel in the name always refers to the one used in simulation (second column) and the second refers to the one used in reconstruction (reconstruction). Last column points to corresponding figures.

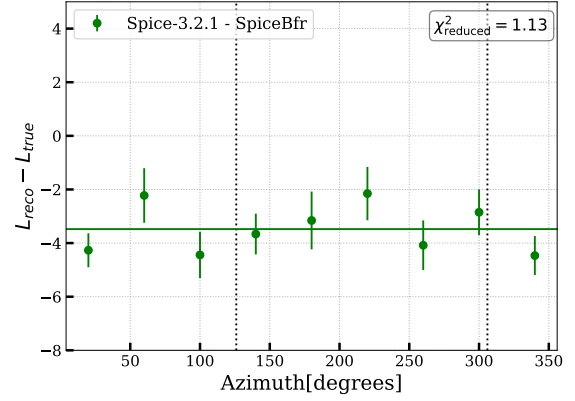
Name	Simulation Icemodel	Reconstruction Icemodel	
Spice-3.2.1-Spice-3.2.1	Spice-3.2.1	Spice-3.2.1	Figure 1.12a
Spice-3.2.1-SpiceBfr	Spice-3.2.1	SpiceBfr	Figure 1.12b
SpiceBfr-Spice-3.2.1	SpiceBfr	Spice-3.2.1	Figure 1.12c
SpiceBfr-SpiceBfr	SpiceBfr	SpiceBfr	Figure 1.12d

arises, if SpiceBfr can further improve reconstruction (or discover any previously unknown biases), hence a comparison was needed.

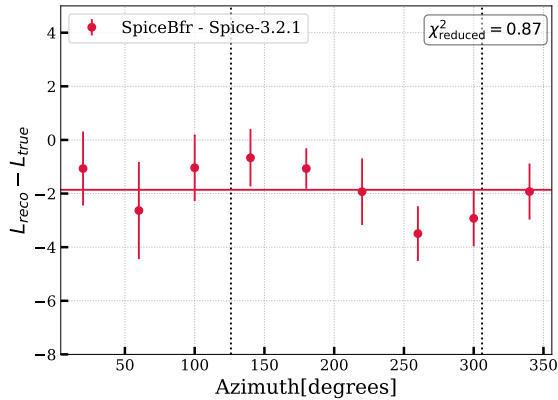
Such a check between Spice-3.2.1 and SpiceBfr was feasible since the spline tables for SpiceBfr were already available. To facilitate cross-comparison, a small statistics (one-third of the full available statistics) simulation set was produced using SpiceBfr. The successfully identified true double cascades are considered, and median length bias ($L_{\text{Reco}} - L_{\text{true}}$) is calculated per azimuth bin (see Figure 1.12). An effective reconstruction algorithm should show no bias (i.e. the difference in length should be zero), unless unaccounted asymmetries exist.



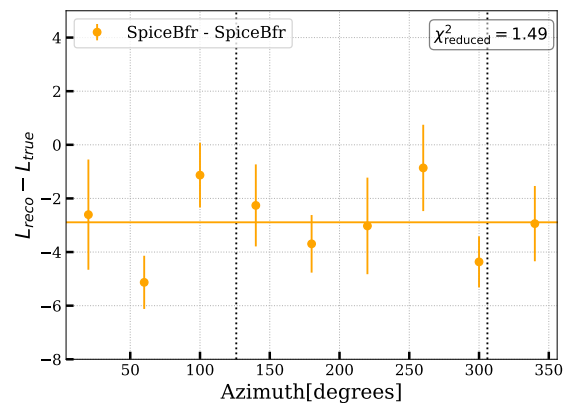
(a) Simulation using Spice-3.2.1 and reconstruction using Spice-3.2.1



(b) Simulation using Spice-3.2.1 and reconstruction using SpiceBfr



(c) Simulation using SpiceBfr and reconstruction using Spice-3.2.1



(d) Simulation using SpiceBfr and reconstruction using SpiceBfr

Figure 1.12: Length Bias of true double cascades, classified as double cascades, as function of Azimuth angle. Vertical lines shows the direction of the major anisotropy axis. Caption below each figures shows which combination of icemodel is used in simulation and reconstruction respectively. Each figure also shows reduced value of χ^2 calculated by fitting the showed horizontal line, see text for details.

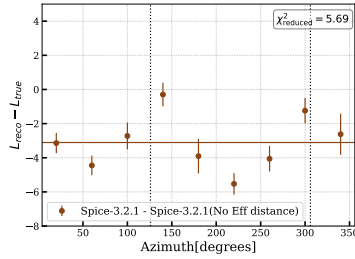


Figure 1.13: Simulation using Spice-3.2.1 and reconstruction using Spice-3.2.1 but no effective distance. See caption of Figure 1.12 for details.

Since all cases involve either the effective distance correction or an inherent anisotropy parametrization (via birefringence), minimal bias was expected along the major anisotropy axis. As shown in the results, only minor structures were observed, and none were deemed statistically significant, particularly along the anisotropy axis. To probe further, a χ^2 goodness-of-fit (gof) test was performed to fit a horizontal line, with the reduced χ^2 calculated for each of the four cases (values indicated on all figures). The results indicated that all four combinations fit well to a horizontal line, signifying no significant biases were present. However, the plots corresponding to the simulation produced using SpiceBfr (both reconstructed with SpiceBfr (Figure 1.12d) and Spice-3.2.1 Figure 1.12c) showed signs of over/underfitting, likely due to the low statistics of the generated SpiceBfr simulation set.

This observed lack of obias aligns with expectations, as Spice-3.2.1 effectively handles anisotropy through the effective distance parameterization. The final step thus, was to verifying if the lack of bias was truly due to the effective distance splines. In Figure 1.13, a distribution is shown where events are simulated using Spice-3.2.1 but reconstructed without the effective distance correction. The resulting reduced χ^2 of 5.69 indicates a poor fit, and a clear bias is visible along the anisotropy axis, as was observed in [13]. This conclusively demonstrates that both Spice-3.2.1 and SpiceBfr, both with appropriate effective distance corrections are well-suited for analyzing ν_τ -induced double cascades in the presence of ice anisotropy.

Since the SpiceBfr model represents the best current understanding of South Pole ice, the decision was made to proceed with simulations using Spice-3.2.1, reconstructed with the SpiceBfr model. This choice is further supported by the reduced χ^2 values across the four cases, where the combination of Spice-3.2.1 simulation and SpiceBfr reconstruction produced the value closest to 1, indicating the most accurate fit. Consequently, the analysis continued with this combination, ensuring the best possible handling of ice anisotropy in the event reconstruction.

Given that the SpiceBfr model represents the best current understanding of the South Pole ice, the decision was made **to proceed with Spice-3.2.1 simulations reconstructed using the SpiceBfr model**. This approach is further supported by the reduced χ^2 values across the four cases, with the Spice-3.2.1 simulation and SpiceBfr reconstruction yielding the value closest to 1, indicating the most accurate fit. Hence, from here-on, it is to be

Using the High Energy Starting Event (HESE) sample introduced in Chapter 1, that classifies high-energy neutrino events into one of three distinct morphologies (Single Cascades, Tracks and Double Cascades), a flavour measurement of the high energy diffuse neutrino spectrum can be performed. This chapter focuses on the methods and various ingredients used to make this flavour measurement.

The chapter begins by detailing these statistical techniques, with a focus on forward folding likelihood fits, which plays a crucial role in distinguishing signal from background in measuring the flavor composition of the astrophysical neutrino flux. The modelling of signal and background events, enhanced for the iteration of this analysis performed in this thesis are explained subsequently. Finally, the chapter evaluates the sensitivity of the analysis, providing estimates of detection limits.

2.1 Statistical Methods	19
2.1.1 Binned Maximum-likelihood Fits	19
2.1.2 SAY Likelihood	21
2.2 Components of the Likelihood Fit	22
2.2.1 Model parameters	23
2.2.2 Analysis Observables and their Distributions	28
2.3 Analysis Sensitivity . . .	31

2.1 Statistical Methods

This analysis utilizes a binned maximum likelihood estimation (MLE) approach to perform statistical inference based on the observed data. Binning the data offers computational efficiency as computing probability densities for an unbinned likelihood is not trivial in the case of finite MC statistics. One need to somehow parametrize them as a function of the signal and nuisance parameters. Forward-folding circumvents this by directly re-computing the distributions corresponding to a certain parameter set. Each analysis bin contains data points from a specific range of measured quantities, such as energy or angular distributions. To incorporate the complexities of detector response and model uncertainties, the concept of forward folding is employed. Forward folding integrates theoretical model predictions with the response of the detector, producing distributions of the expected event rate that can be directly compared to the binned observed data. This method allows for testing different flux models of arbitrary shape, along with the systematic uncertainties of these models as well as the detector responses, all folded into the predicted likelihood.

2.1.1 Binned Maximum-likelihood Fits

When fitting a data sample with a large size (large N), it is common practice to bin the data in order to enhance the computational efficiency of the likelihood function calculation. This binning procedure groups the data into discrete intervals, or *bins*, based on one or more *observables* (derived from reconstructed properties of the neutrino events), such as energy or zenith. This simplification is not harmful as long as the variation of the probability density function (PDF), $f(x|\theta)$, within each bin is insignificant compared to its variation across the neighbouring bins. In other words, the binning should not discard crucial information about

the parameter vector θ that governs the underlying physical model. If a binning is applied appropriately, the fit retains the ability to accurately infer the parameters of interest while significantly speeding up the computational process, particularly in high-dimensional analyses where unbinned likelihood fits may be computationally prohibitive.

The binned likelihood method works by comparing the number of observed events in each bin to the expected number of events, which are typically predicted through Monte Carlo simulations. In the analysis, these Monte Carlo templates are created for various theoretical flux components, such as astrophysical, atmospheric etc. that constitute signal and background to the measurement. Each template provides a predicted event distribution based on specific values of the *signal* parameters θ along with *nuisance* parameters, ξ , which describe the physical processes being studied. These templates are obtained from forward folding, meaning they incorporate the effects of the detector response, before being compared to the observed data. By adjusting the model parameters, the predicted event counts in each bin can be varied to find the *best fit* to the data. The number of observed events n_i in each bin i (n_i), is assumed to follow a Poisson distribution¹ [40]. The expected number of events in bin i , $\mu_i(\theta, \xi)$, represents the sum of contributions from all signal and background components. The Poisson likelihood for a given bin is defined as:

1: This is a good assumption because what we are doing here is essentially a counting experiment in every bin.

[40]: Behnke et al. (2013), *Parameter Estimation*

$$P(n_i|\mu_i(\theta, \xi)) = \frac{\mu_i(\theta, \xi)^{n_i} e^{-\mu_i(\theta, \xi)}}{n_i!} \quad (2.1)$$

where $\mu_i(\theta, \xi)$ is the expected number of events in bin i and n_i is the observed number. The total likelihood for the entire dataset is then the product of the likelihoods for all bins:

$$\mathcal{L}(n|\mu_i(\theta, \xi)) = \prod_{i=1}^N P(n_i|\mu_i(\theta, \xi)) \quad (2.2)$$

Incorporating systematic uncertainties into the likelihood function is crucial for obtaining realistic results, as these uncertainties often arise from imperfect detector calibration or background estimations. Such systematic uncertainties are modeled as nuisance parameters in the likelihood fit. These parameters are typically constrained by prior knowledge and treated as additional variables in the fitting process. For each of the k nuisance parameters, ξ_j , a Gaussian prior is introduced, penalizing deviations from the central value $\bar{\xi}_j$ by an amount proportional to the known uncertainty σ_{ξ_j} , extending the likelihood to:

$$\mathcal{L}(n|\mu_i(\theta, \xi)) = \prod_{i=1}^N P(n_i|\mu_i(\theta, \xi)) \prod_{j=1}^k \exp\left(-\frac{1}{2} \left(\frac{\xi_j - \bar{\xi}_j}{\sigma_{\xi_j}}\right)^2\right) \quad (2.3)$$

By maximizing this likelihood, the best-fit parameters θ can be found. In practice, the fit is performed by minimizing $-\ln \mathcal{L}$, as it simplifies the computation (see 2.4).

$$\ln(\mathcal{L}(n|\mu_i(\theta, \xi))) = \sum_{i=1}^N [n_i \ln(\mu_i) - \ln(n_i!) - \mu_i] - \sum_{j=1}^k \frac{1}{2} \left(\frac{\xi_j - \bar{\xi}_j}{\sigma_{\xi_j}} \right)^2 \quad (2.4)$$

Once the likelihood function is constructed, the next step is hypothesis testing. A specific model hypothesis can be tested by using a likelihood ratio test. The likelihood ratio compares two hypotheses: the test model (with parameters θ_t) and the best-fit model (with parameters $\hat{\theta}$):

$$-2\Delta \ln \mathcal{L} = -2 \ln \left(\frac{\mathcal{L}(n|\mu(\theta_t, \xi_t))}{\mathcal{L}(n|\mu(\hat{\theta}, \hat{\xi}))} \right) \quad (2.5)$$

The factor -2 is included for convenience, as the thus constructed test statistic follows a χ^2 distribution under certain regularity conditions [**profile_llh**]. Now, according to Wilks' theorem [41], this enables the calculation of confidence levels (CL) of the parameter of interest without the need for calculating the sampling distribution of $-2\Delta \ln \mathcal{L}$ based on pseudo-experiments, which can be computationally expensive. However, Wilks' theorem is only valid when the dataset is large and the model parameters are unbounded. If either condition is not met, the test statistic may deviate from a χ^2 -distribution, necessitating the use of Monte Carlo pseudo-experiments to determine the confidence intervals via the so-called *Feldman Cousins* method [42], with an extension to incorporate nuisance parameters [43, 44].

The test statistic derived from the likelihood ratio, defined in Equation 2.5 can be used to construct confidence regions for the parameters of interest, the process known as a **profile likelihood test**. For instance, in one-dimensional profile likelihood test, the confidence interval is obtained by comparing the test statistic to the cumulative distribution of a χ^2 -distribution with one degree of freedom. When scanning over two or more parameters, calculating the profile likelihood ratio on a multi-dimensional grid of parameter values is required, which significantly increases the computational complexity. In some cases, the Asimov dataset [44]—a single dataset representing the median outcome of many pseudo experiments—can be used to estimate the median sensitivity of the analysis. This method provides an efficient way to estimate confidence intervals and test the sensitivity of the analysis without the need for exhaustive Monte Carlo pseudo-experiments. The Asimov dataset and Wilks' theorem are both used to derive the sensitivity of the analysis as presented in 2.3. It is important to point out that the primary parameters of interest in this analysis are the astrophysical neutrino flavour fractions. The number of ν_τ events, which provide the strongest constraint on astrophysical ν_τ fraction in the flux, is small. Additionally, the flavour fractions in the likelihood fit are constrained to be non-negative always, therefore the applicability of Wilk's theorem is evaluated as needed.

2.1.2 SAY Likelihood

The likelihood construction described in section 2.1.1 relies on the Poisson likelihood, which assumes that the expectations for each bin, μ_i , to be

profile_llh

[41]: Wilks (1938), *The Large-Sample Distribution of the Likelihood Ratio for Testing Composite Hypotheses*

[42]: Feldman et al. (1998), *Unified approach to the classical statistical analysis of small signals*

[43]: Sen et al. (2009), *On the unified method with nuisance parameters*

[44]: Cowan et al. (2011), *Asymptotic formulae for likelihood-based tests of new physics*

known exactly. This assumption holds when the Monte Carlo simulations used in generating the expected distributions have large statistics, so that the uncertainty on μ_i due to finite MC statistics is small compared to the uncertainty on the observed data counts. However, MC simulations inherently come with their own uncertainties due to finite statistics, particularly in high energy bins where the difficulty to populate them becomes larger due to increase in computational costs.

In binned forward-folding fits, statistical inferences are made by comparing observed data counts in each bin to the expected counts derived from the simulations. As outlined in Equation 2.1, the Poisson likelihood assumes that μ_i , the expected value per bin, is well-determined. However, this is often not the case in analyses like the one performed in this thesis, where overall event rates are low, and individual bin expectations may fluctuate significantly due to limited MC statistics. This mismatch can lead to overconfident predictions if these fluctuations in μ_i are not correctly accounted for.

[45]: Argüelles et al. (2019), *A binned likelihood for stochastic models*

To address this issue, an extended form of the Poisson likelihood (\mathcal{L}_{eff}), or the so-called **SAY likelihood**, is used in this analysis [45]. This likelihood incorporates the uncertainty from the limited MC statistics and provides more appropriate coverage for parameter estimates based on this likelihood. Specifically, the distribution of MC event weights in each bin is modeled using a scaled Poisson distribution, which introduces an additional uncertainty term, σ_j^2 , for each bin. This term depends on the weights w_j of the simulated MC events j in the i -th bin and is defined as:

$$\sigma_i^2 = \sum_j (w_j^i)^2 \quad (2.6)$$

This uncertainty term, σ_i^2 , is larger in bins with low statistics, and smaller in bins with higher statistics, ensuring that fluctuations in low-stat bins are adequately covered. This formalism results in more conservative limits, with generally wider contours for the final result, as the additional statistical uncertainty is incorporated into the fit. One limitation of this approach is that the Asimov dataset [44], described in the previous section, cannot be constructed when using the SAY likelihood. This is because the σ_j term can significantly skew the distribution $\mathcal{L}_{\text{eff}}(\mu_i | \sigma_i, d_i)$ so that the maximum is not at $\mu_i = d_i$, which is the defining property of the Asimov set. As a result, deviations from injected values may appear, especially in cases like the simulation produced for single atmospheric muons (MuonGun, explained in Section 1.1.1), which exhibits lack of high statistics due to high energy threshold of HESE sample, used in this work. Alternatively, the standard Poisson likelihood can be used, though the resulting limits may be overconfident.

[44]: Cowan et al. (2011), *Asymptotic formulae for likelihood-based tests of new physics*

2.2 Components of the Likelihood Fit

The choice of the likelihood function and its subsequent requirements (the SAY likelihood) was outlined in the previous section. In this section, the focus shall be on the essential components involved, and their modeling. The construction proceeds as follows:

1. The parameters to be measured, known as *signal parameters* (denoted by θ), along with all *nuisance parameters* (ξ), which may originate from uncertainties in the detector response or background modeling (such as atmospheric spectra), are identified and bounded where necessary.
2. These parameters are applied in the form of the neutrino *flux*, assigning each Monte Carlo event a specific *weight* based on the individual fluxes.
3. A set of observables that are most sensitive to the signal parameters, such as astrophysical neutrino fluxes, is selected and the simulated and experimentally observed events are accordingly binned for the analysis. The experiment is performed, and the observed data events n are sorted into the predefined bins of the analysis histograms.
4. A fit is conducted by varying each of the parameters (and, consequently, the fluxes) until the observed data events are optimally described.

prior prefers that the parameters remain within the 1σ prior region, pe-

values outside this range.

2.2.1 Model parameters

All the model parameters used in the fit, grouped by the flux component (astrophysical or atmospheric) that they affect, are listed in Table 2.2. Moreover, several nuisance parameters describing uncertainty in the detector response are included in the fit. Baseline models and their corresponding values, wherever applicable, are specified for each parameter, along with the choice of priors. The astrophysical flux parameters represent the high-energy neutrino contributions from distant sources, while atmospheric flux models account for neutrinos originating from cosmic ray interactions within in atmosphere of Earth.

The flux of astrophysical neutrinos is modeled as a single power law of the form

$$\Phi_{\nu+\bar{\nu}}^{\text{astro}}(E_\nu) = \Phi_0^{\text{astro}} \times (1 + s_{\nu_e} + s_{\nu_\tau}) \times \left(\frac{E_\nu}{100 \text{ TeV}} \right)^{-\gamma_{\text{astro}}} \quad (2.7)$$

where γ_{astro} is the spectral index, E_ν is the neutrino energy, and $\Phi_{\nu+\bar{\nu}}^{\text{astro}}$ is the all-flavor (including particle and anti-particle) normalization. Two scaling factors, s_{ν_e} and s_{ν_τ} , modify the flux of electron and tau neutrinos relative to the muon neutrino flux Φ_0 . These scaling factors relate to the flavour ratio $f_{\nu_e} : f_{\nu_\mu} : f_{\nu_\tau}$ as:

$$f_e = \frac{s_{\nu_e}}{(1+s_{\nu_e}+s_{\nu_\tau})}, \quad f_\mu = \frac{1}{(1+s_{\nu_e}+s_{\nu_\tau})}, \quad f_\tau = \frac{s_{\nu_\tau}}{(1+s_{\nu_e}+s_{\nu_\tau})} \quad (2.8)$$

The signal parameters for the flavor analysis are these two scaling factors, Φ_0 , and γ_{astro} . All other subsequent parameters explained are the nuisance parameters. In Eq. 2.13, it is assumed that each flavor has an identical spectral shape (γ_{astro}). This assumption is justified because the HESE sample used in this analysis is small and has limited power to constrain spectral properties resolved by neutrino flavor. For the sensitivity study described in ??, the benchmark spectral parameter values are taken from the previous iteration of this analysis [19], with $\gamma_{\text{astro}} = 2.87$ and

[19]: Abbasi et al. (2021), *IceCube high-energy starting event sample: Description and flux characterization with 7.5 years of data*

Table 2.1: Parameters used in the likelihood described in Equation 2.3. The gaussian priors on the parameters (if applicable) in terms of the mean (μ) and width (σ) are stated on the alongside.

Parameter	Prior (μ, σ)
Astrophysical Flux (Signal) Parameters	
astro. ν_μ normalisation [$10^{-18}\text{GeV}^{-1}\text{cm}^{-2}\text{sr}^{-1}\text{s}^{-1}$](ϕ_{ν_μ})	-
astro. spectral index (γ_{astro})	-
scaling factor to modify total flux norm ($\Phi_{\nu+\bar{\nu}}^{\text{astro}}$) relative to ϕ_{ν_μ} (s_{ν_e} astro. ν_e)	-
astro. ν_τ scaling factor to modify total flux norm ($\Phi_{\nu+\bar{\nu}}^{\text{astro}}$) relative to ϕ_{ν_μ} (s_{ν_τ})	-
Atmospheric Flux Systematics	
Conventional Flux normalisation (Φ_{conv})	(1.0,0.2)
Prompt Flux Normalisation (Φ_{prompt})	-
Interpolation between Cosmic Ray Models (ξ_{CR})	(0,1)
Cosmic Ray Spectral Index Shift ($\Delta\gamma_{\text{CR}}$)	(0,0.05)
Barr-parameter modifying the pion-contribution (H_{Barr})	(0,0.15)
Barr-parameter modifying the kaon-contribution (W_{Barr})	(0,0.40)
Barr-parameter modifying the kaon-contribution (Y_{Barr})	(0,0.30)
Barr-parameter modifying the kaon-contribution (Z_{Barr})	(0,0.12)
Muon Flux Normalisation (Φ_{muon})	(1,0.5)
Scale factor for Neutrino Nucleon Inelasticity weight (I_{scale})	(1,0.1)
Detector Systematics	
Optical Efficiency of DOMs (η_{domeff})	(1.0,0.1)
Ice Absorption Scaling (η_{abs})	(1.0,0.05)
Ice Scattering Scaling (η_{scat})	(1.0,0.05)
Parametrization for refrozen icecolumn ($\eta_{\text{h.ice-p0}}$)	(-0.27,0.5)
Parametrization for refrozen icecolumn ($\eta_{\text{h.ice-p1}}$)	(-0.042,0.05)
Ice Anisotropy Scaling (η_{aniso})	-

$\Phi_0 = 2.12 \times 10^{-18} \text{GeV}^{-1} \text{cm}^{-2} \text{sr}^{-1} \text{s}^{-1}$ assuming an equipartition of flavor ratios (i.e., $\nu_e : \nu_\mu : \nu_\tau = 1 : 1 : 1$).

Atmospheric flux components are constrained by priors because they are more accurately measured with other IceCube data samples. In contrast, the number of atmospheric events in the HESE selection is low due to the high efficiency in reducing atmospheric muons due to the veto requirement and the down-going atmospheric neutrinos from the same cosmic-ray-induced air shower, thanks to the self-veto effect.

Depending on the parent hadron type, the atmospheric neutrino flux is divided into two components: **The Conventional neutrino flux** (produced in the decay of charged pions and kaons) and **The Prompt Neutrino Flux** (produced in the decay of charmed mesons). The various models of atmospheric neutrino fluxes are detailed in ?? The atmospheric neutrino flux contribution is modeled using the Matrix Cascade Equation Solver (MCEq) [26]. The baseline primary cosmic-ray model for this calculation is H4a [46], combined with a hadronic interaction model SIBYLL2.3c [47], introducing conventional (Φ_{conv}) and prompt (Φ_{prompt}) flux normalizations to account for overall flux level uncertainties. Additionally, they are folded with the generalized self-veto probability, as described in 1.2, to account for the reduced rate of atmospheric neutrinos accompanying vetoed muons from the same cosmic-ray-induced air shower. Other nuisance parameters modifying the shape of these spectra include ξ_{CR} , which interpolates between two primary cosmic-ray models H4a and GST, an approach introduced in [48]. The cosmic-ray model uncertainty is the largest source of uncertainty in the overall atmospheric background. Furthermore, $\Delta\gamma_{\text{CR}}$ accounts for corrections in the spectral

[26]: Fedynitch et al. (2015), *Calculation of conventional and prompt lepton fluxes at very high energy*

[46]: Gaisser (2012), *Spectrum of cosmic-ray nucleons, kaon production, and the atmospheric muon charge ratio*

[47]: Riehn et al. (2018), *The hadronic interaction model SIBYLL 2.3c and Feynman scaling*

[48]: Abbasi et al. (2022), *Improved Characterization of the Astrophysical Muon-neutrino Flux with 9.5 Years of IceCube Data*

index of the primary cosmic-ray spectrum, see for e.g. [49]. Uncertainties in the hadronic interaction models, due to various π and K production cross-sections in different energy phases, introduce energy-dependent variations in atmospheric flux expectations [50]. These nuisance parameters, referred to as *Barr* parameters, are computed as described in [51]. A detailed discussion on implementing these parameters within the software framework can be found in [18].

As mentioned, the veto and charge/energy cuts effectively reduce the rate of atmospheric neutrinos. However, high-energy single muons can still enter the detector, contaminating the sample. **The atmospheric Muon Flux** component is constrained by a prior partially derived from experimental data. The spectral shape is determined using a dedicated simulation that produces a flux of single muons reaching the detector (MUONGUN, described in 1.1), weighted assuming the same baseline models used for atmospheric spectra (H4a). A pure-proton composition is chosen for these muons as it contributes the highest energy single muons. The normalization is estimated using the tagging method described in [19]. A separate nuisance parameter, Φ_{muongun} , is included in the fit to account for these muons. A prior derived from this study is applied in this analysis. The sensitive energy range of this analysis is high, and the sample is specifically designed to minimize background contamination from atmospheric neutrinos and muons (see Section 1.2). The available MUONGUN Monte Carlo was generated for various other IceCube analyses, that targeted lower energies as well, where background contributions are significantly higher. Most Monte Carlo events do not pass the strict cuts of this analysis, with no events at all in the cascade and double cascade bins (see Figure 2.4 and Figure 2.6). Consequently, the statistical uncertainty on this component is high, requiring a Kernel Density Estimate (KDE) for smoothing.

The remaining nuisance parameters are those arising from the imperfect knowledge of the detector response, such as the Digital Optical Modules (DOMs, see section ??), and the detection medium, which includes both the bulk ice and hole ice models (see section ??), denoted as from here-on as **Detector Systematics**. These detector systematics introduce uncertainties that can affect both the energy scale of the neutrino events and the shape of observable distributions, thereby altering the expected event rates from different flux components. Unlike previous iterations of this analysis [13, 30], which relied on discrete Monte Carlo simulation sets with different values for systematics that significantly impacted the analysis observables, the current approach uses the SnowStorm simulation technique (see section 1.1.2). The SnowStorm method [16] captures the full range of detector systematic variations in a single Monte Carlo dataset, avoiding the need for generating multiple datasets. It uses a first-order Taylor expansion of the observables, such as event counts in each bin, with respect to the detector systematics. The resulting gradient, called *the nuisance gradient* (\vec{G}), allows for efficient computation of observable values as these systematic parameters vary. The expectation value of per bin event count μ , for nuisance parameter variations $\vec{\eta}$ is given as,

$$\mu(\vec{\eta}) = \mu_{\text{baseline}} + \vec{\eta} \cdot \vec{G} \quad (2.9)$$

[49]: Niederhausen (2018), *Measurement of the High Energy Astrophysical Neutrino Flux Using Electron and Tau Neutrinos Observed in Four Years of IceCube Data*

[50]: Barr et al. (2006), *Uncertainties in Atmospheric Neutrino Fluxes*

[51]: Fedynitch et al. (2022), *Data-driven hadronic interaction model for atmospheric lepton flux calculations*

[18]: Naab (2024), *Evidence for a Break in the Diffuse Extragalactic Neutrino Spectrum*

[13]: Usner (2018), *Search for Astrophysical Tau-Neutrinos in Six Years of High-Energy Starting Events in the IceCube Detector*

[30]: Stachurska (2020), *Astrophysical Tau Neutrinos in IceCube*

[16]: Aartsen et al. (2019), *Efficient propagation of systematic uncertainties from calibration to analysis with the SnowStorm method in IceCube*

[18]: Naab (2024), *Evidence for a Break in the Diffuse Extragalactic Neutrino Spectrum*

2: For the analysis presented in this thesis, the gradients are computed using the best-fit values from the HESE-7.5 year analysis [19], with $\gamma_{\text{astro}} = 2.87$, the per-flavour flux normalization $\Phi_{\nu+\bar{\nu}}^{\text{astro}} = 2.12$, and an equipartition among all three flavour fluxes.

3: The appropriate range here refers to a set of spectral measurements made by various IceCube samples [ESTES, 19, 48, 58].

4: also, a negative number of expected events is unphysical anyway!

spicemie

where, μ_{baseline} is the expectation value of per bin count at baseline values of all detector systematic parameters (baseline values are the central value at which simulation was generated), when $\vec{\eta} = \vec{0}$. For this approach to be valid, it assumes that systematic effects are small enough to be treated perturbatively, allowing for a linear approximation. By marginalizing over the full ensemble of systematic variations, the prediction converges to that of the central model, effectively neglecting second-order effects. Because the dataset itself have finite statistics, appropriate uncertainty propagation is applied to the nuisance gradient (see [18] for details of calculations of this gradient, their uncertainties and incorporation within such fits).

For each analysis bin, both the expected number of events (μ_i) and the associated variance (σ_i) are computed, that enter the likelihood calculation, described in Equation 2.4. However, two important caveats should be noted with this method. First, the gradients are calculated based on a specific flux assumption² and are not recalculated at every minimization step. This significantly reduces the computational time of the minimization process but may introduce inaccuracies if the assumed fluxes deviate significantly from the true values in nature, which could substantially alter the resulting gradients. A potential solution is to compute the gradients over a range of flux assumptions to check for significant deviations in the results. For the analysis presented in this thesis, this was tested by varying single-power law parameters (index and normalisation) defined in Equation 2.13, in appropriate range³ and the results ensured that this was a higher order effect. The second caveat arises because the expected event counts per bin, calculated using the gradients as shown in Equation 2.9, are applied as an *additive* correction to the overall flux expectation. Since the gradient is a real valued vector, it can also take negative values. For softer spectra and the limited statistics of the HESE sample, this can result in negative bin counts when the expected values approach zero. This presents a problem for the likelihood fit used in the analysis, as the logarithm of a negative number⁴ cannot be computed (which the fitter will attempt to do at some point; see Equation 2.4). To avoid this numerical issue, the expectation value calculated via the gradients is clipped at $\mu = 0 + \epsilon$. This ad hoc correction is justified because, although μ_{baseline} may be zero in these bins, there remains significant statistical uncertainty, which typically dominates over the systematic variations.

The aforementioned gradient, can be constructed using 6 detector systematics simulated within the snowstorm ensemble. For the analysis presented in this thesis, it is constructed using 6 parameters, listed in the Table 2.2.

The DOM Efficiency (η_{domeff}) accounts for factors like the quantum efficiency of the PMT and shadowing by attached cables, reducing the efficiency by 1%. The overall uncertainty is estimated at $\pm 10\%$ [spicemie]. This impacts the reconstructed energy, as lower efficiency underestimates the photon light yield. This effect is relevant in the analysis, as it shifts the energy distribution across bins and the energy thresholds in particular.

Absorption (η_{abs}) and Scattering (η_{scat}) Scaling accounts for variations in scattering and absorption coefficients of the ice model, mapped across a depth grid of the south pole ice. The baseline model for

this mapping is SPICE-3.2.1, with priors set to a 5% width around the central value, based on the uncertainty derived from calibration data obtained using flasher LEDs [spicemie]. An increase in scattering coefficients extends the photon scattering path, increasing the chance of absorption before detection. Variations in ice scattering and absorption mainly affect energy reconstruction and may introduce minor directional bias, with the energy shift being the primary concern in this analysis.

hole ice parameters ($\eta_{\text{h.ice-p0}}$ and $\eta_{\text{h.ice-p1}}$) accounts for the differences in optical properties between the refrozen ice in the DOM deployment columns and the surrounding bulk ice. Uncertainties and priors are based on a recent study that analyzed flasher data [52].

Ice anisotropy discussed in detail in sections ?? and 1.5 affects the double cascade reconstruction greatly. For the icemodel used in simulation, this parameter is modelled as a modulation of the nominal scattering coefficient, analogous to that used in [21].

[52]: Eller et al. (2023), *A model independent parametrization of the optical properties of the refrozen IceCube drill holes*

[21]: Abbasi et al. (2022), *Detection of astrophysical tau neutrino candidates in IceCube*

Lastly, an additional nuisance parameter, affecting the DIS neutrino interaction cross section (discussed in Section ??) and thus all the neutrino fluxes (Astrophysical and atmospheric) is used. The so-called **Neutrino-Nucleon Inelasticity Scaling** (I_{scale}) parameter is introduced to account for inelasticity which is a measure of the fraction of the neutrino's energy that is transferred to the hadronic system in an inelastic neutrino nucleon scattering process, mathematically given as,

$$y = \frac{E_{\text{hadron}}}{E_{\nu}} \quad (2.10)$$

The Mean inelasticity $\langle y \rangle$ is the average value of the inelasticity y over many scattering events. It provides a statistical measure of the average fraction of the neutrino's energy that is transferred to the hadronic system. This is particularly relevant for starting tracks, as the mean inelasticity, $\langle y \rangle$, depends on the incoming neutrino energy. Since $\langle y \rangle$ evolves as a function of energy (see Section ??), it indicates the fraction of the neutrino's energy transferred to the hadronic system during the ν_{μ} charged-current (CC) interaction. Consequently, this also determines how much energy is imparted to the muon in starting tracks. Thus, variations in $\langle y \rangle$ with energy influence the overall energy distribution of the events. For this analysis, a scaling factor is introduced, which is based on formulation provided in [53], that allows to vary Normalisation N of the inelasticity distribution,

[53]: Aartsen et al. (2019), *Measurements using the inelasticity distribution of multi-TeV neutrino interactions in IceCube*

$$\frac{dp}{dy} = N (1 + \epsilon(1 - y)^2) y^{\lambda-1} \quad (2.11)$$

where N is the normalisation given as,

$$N = \frac{\lambda(\lambda + 1)(\lambda + 2)}{2\epsilon + (\lambda + 1)(\lambda + 2)} \quad (2.12)$$

The theoretical prediction of $\langle y \rangle$ from the CSMS model [31] is calculated for the mean inelasticity distribution for a given event. By fixing $\langle y \rangle$, λ 2.12 is fitted to apply a reweighting factor to *scale* the inelasticity (I_{scale}). Variations are permitted within 10% of their default value. The parameter is applied to all neutrino fluxes as via Deep Inelastic Scattering.

[31]: Cooper-Sarkar et al. (2011), *The high energy neutrino cross-section in the Standard Model and its uncertainty*

2.2.2 Analysis Observables and their Distributions

In forward folding fits, selecting appropriate observables is crucial for distinguishing between the signal and background hypotheses. The analysis uses all the HESE events above 60 TeV, further divided in 3 sub-samples of *Single Cascades*, *Tracks* and *Double Cascades*. These 3 sub-samples are binned in 2-dimensional Monte Carlo templates of appropriate observables, such that background and signal templates are clearly distinguishable. When measuring the spectrum of astrophysical neutrinos, the background consists of neutrinos produced in atmospheric air showers. Key observables that allow for effective differentiation between astrophysical and atmospheric neutrinos include the total deposited energy (E_{tot}) and the zenith angle (θ_{zenith}) of the interacting neutrino. The motivation for focusing on these variables stems from their distinct behavior in atmospheric and astrophysical neutrino spectra (see Section ??). In particular, down-going atmospheric neutrinos are efficiently suppressed due to the self-veto effect, while up-going atmospheric neutrinos, which cannot be reduced by this veto, become an irreducible background.

The astrophysical spectrum that is assumed for all the Monte Carlo templates and sensitivity is using a single-power law based on best-fit values of HESE-7.5 years spectrum measurements [19], given as,

$$\frac{d\Phi_{\nu+\bar{\nu}}^{\text{astro}}}{dE} = 6.98 \cdot 10^{-18} \left(\frac{E_{\nu}}{100 \text{ TeV}} \right)^{-2.87} \quad (2.13)$$

In units of $\text{GeV}^{-1} \text{ cm}^{-2} \text{ s}^{-1} \text{ sr}^{-1}$, with flavour composition of $\nu_e : \nu_{\mu} : \nu_{\tau} = 1 : 1 : 1$

The prompt component is missing from all templates as best-fit value of Φ_{prompt} of prompt flux normalization was 0.

For the analysis presented in this thesis, the primary goal is to measure the flavor composition of astrophysical neutrinos. A key component of this analysis, as highlighted in Section 1.4, is the identification and classification of ν_{τ} -induced double cascade events. Note that the PID assigned is not used as a proxy to tag flavour on an individual event bases, but through statistical analyses of the overall data set, Monte Carlo templates. Double cascades are a signature of ν_{τ} interactions, and their identification relies heavily on the observables E_{tot} and the reconstructed double cascade length (L_{dc}), which provide the most discriminatory power for separating the flavors of astrophysical neutrinos, see Figure 2.1. All double cascade events are binned into a two-dimensional Monte Carlo template, with one axis representing the reconstructed tau decay length (L_{dc}) and the other representing the reconstructed total deposited energy (E_{Tot}). The L_{dc} is divided into 10 bins ranging from 10 m to 1000 m, while E_{Tot} is divided into 13 bins spanning 60 TeV to 12.6 PeV, both using logarithmic spacing, as shown in Figure 2.1. It is important to note that adding a third dimension, such as energy asymmetry, offers significant discriminatory power by reducing the low-length single cascade background, enhancing the sensitivity to measure the flavor ratio [54]. However, a detailed study revealed that the limited Monte Carlo statistics and small size of the HESE sample resulted in many empty bins, which posed challenges for forward-folding fits. As a result, the third dimension was ultimately excluded from the analysis.

[54]: Lad et al. (2023), *Summary of IceCube tau neutrino searches and flavor composition measurements of the diffuse astrophysical neutrino flux*

Under the double cascade hypothesis, true single cascades are typically reconstructed with a small L_{dc} but with most of their energy concentrated in the first cascade (with the energy asymmetry $E_A \rightarrow 1$). Hence, misclassified single cascades tend to cluster around low L_{dc} and low E_{Tot} , with the distribution of L_{dc} falling off rapidly, as indicated by the verticle line, on right panel of Figure 2.1. In cases where a track is reconstructed under the double cascade hypothesis, the largest energy depositions are interpreted as the cascade vertices, leading to an arbitrary L_{dc} value. These tracks, when misclassified as double cascades, typically exhibit low E_{Tot} , consistent with the falling astrophysical spectrum. This is also visible in right panel of Figure 2.1.

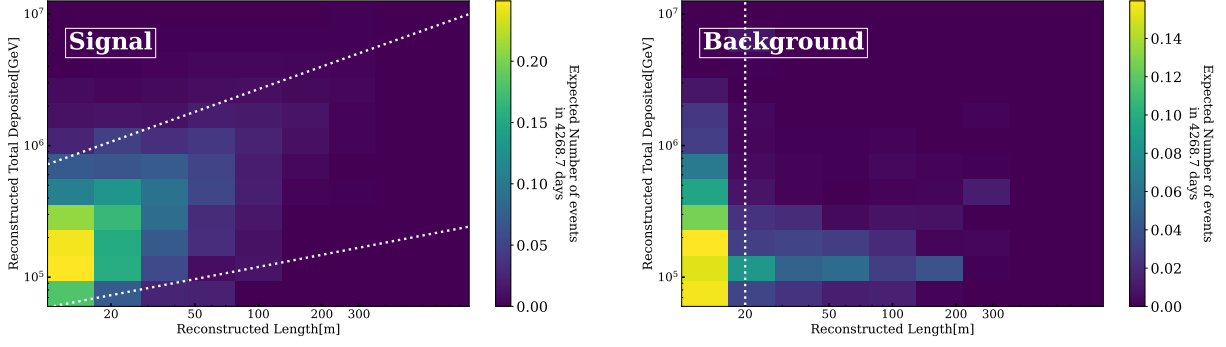


Figure 2.1: 2D Monte Carlo templates, constructed using reconstructed total energy (E_{Tot}) and double cascade length (L_{dc}) for events classified as **double cascades**. The signal (left), representing ν_τ -induced double cascades, shows a clear correlation between L_{dc} and E_{Tot} , with 68% of events within the indicated signal region (dotted white line). In contrast, the background (right), consisting of ν_μ and ν_e events, lacks this correlation and clusters at low L_{dc} , 68% of all the background events lying below the indicated white dotted verticle line.

True double cascades from ν_τ -CC interactions, on the other hand, exhibit a strong correlation between L_{dc} and E_{Tot} . This correlation between L_{dc} and E_{Tot} is primarily used to determine the compatibility of an event with a ν_τ interaction as opposed to another flavor. The Monte Carlo distributions (PDFs) of ν_τ -induced double cascades clearly show this correlation (see left panel of Figure 2.1, indicating 68% region of all classified true double cascade events).

For single cascades and tracks, the observables E_{Tot} (21 bins from 60 TeV to 12.6 PeV in log space) and $\cos(\theta_z)$ (10 bins from -1 to 1 in cosine space) are commonly used, as they offer the most significant discrimination between astrophysical and atmospheric neutrinos, as shown in Figure 2.2 for cascades and Figure 2.3 for tracks. In both Figures, the suppression of atmospheric neutrinos (right panel) ($\cos(\theta_z) > 0.25$, the so-called *down-going region* in IceCube) is clearly visible due to the self-veto effects, whereas astrophysical template (left panel) shows no such pattern^{-7cm}, indicating neutrinos from all directions are accepted.

^{-7cm}: Looking at the plot, it is not entirely true, as we do observe more events in the downgoing region $\cos(\text{zenith}) \geq 0.5$ because the up going region requires

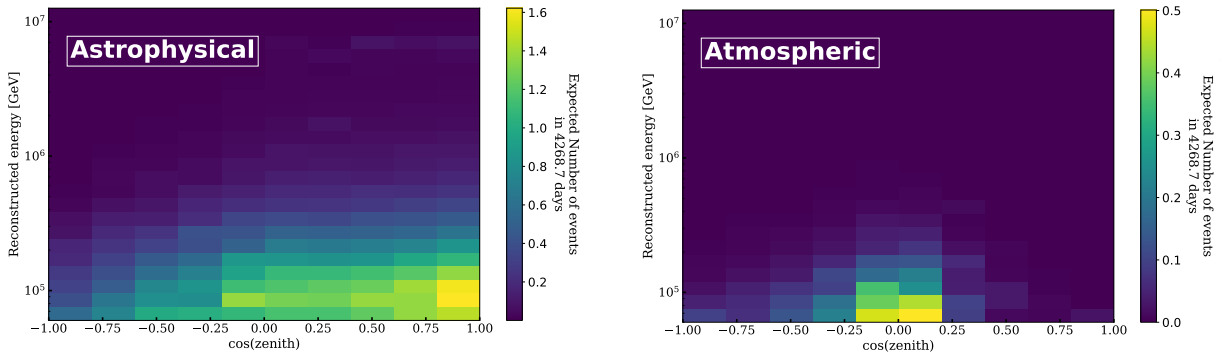


Figure 2.2: 2D Monte Carlo templates, constructed using reconstructed total energy (E_{Tot}) and reconstructed zenith ($\cos(\theta_z)$) for events classified as **single cascades**. The signal (left), representing *Astrophysical neutrinos* of the sample and the background (right), representing *Atmospheric neutrinos*, including conventional, prompt and single muon fluxes.

This becomes more evident in the one-dimensional (energy-averaged) distribution for both of these subsamples (Figure 2.4 for cascades and Figure 2.5 for tracks), where total expectation is broken down in individual flux contributions (as described in 2.2.1). In the case of Energy distribution of single cascades (right panel of Figure 2.4), except for lower energy bins (up to ~ 110 TeV), astrophysical single cascade events

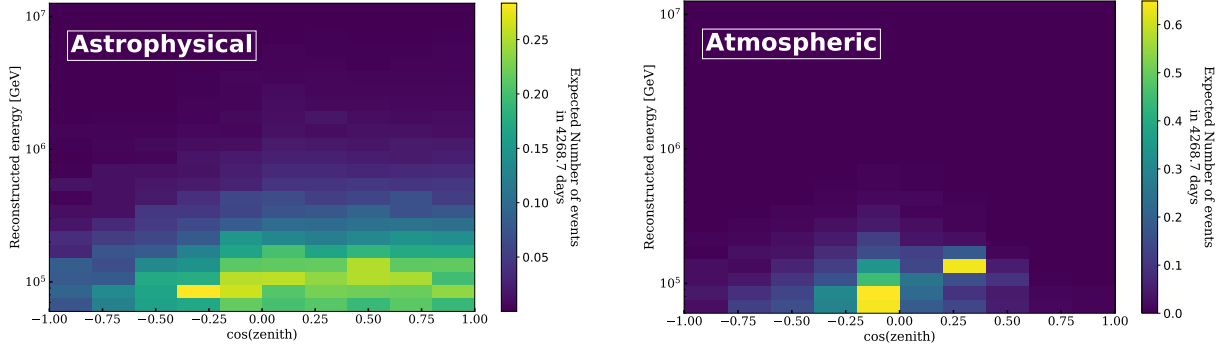


Figure 2.3: 2D Monte Carlo templates, constructed using reconstructed total energy (E_{Tot}) and reconstructed zenith ($\cos(\theta_z)$) for events classified as **tracks**. The signal (left), representing *Astrophysical neutrinos* of the sample and the background (right), representing *Atmospheric neutrinos*, including conventional, prompt and single muon fluxes.

5: recall that single cascades also show contributions from all flavour Neutral Current (NC) interactions

dominate. The Glashow peak due to the resonant interaction of $\bar{\nu}_e$ is clearly visible too. Note the missing muon component, due to lack of enough MUONGUN simulation, as described in 2.2.1. For Tracks (Figure 2.5), there is a similar suppression due to the self-veto effect. The contribution of single muons, simulated using MUONGUN events, is clearly visible, dominating in the same down-going region. As described before, the template is noisy due to large Monte Carlo uncertainties. In general, the tracks sample shows a larger contribution due to atmospheric fluxes compared to single cascades⁵. Similar one dimensional distributions of L_{dc} and E_{Tot} are shown for completeness in Figure 2.6, but as described before, double cascades do not show any striking contributions from going the atmospheric fluxes as the background for this sample is due to ν_e and ν_μ events.

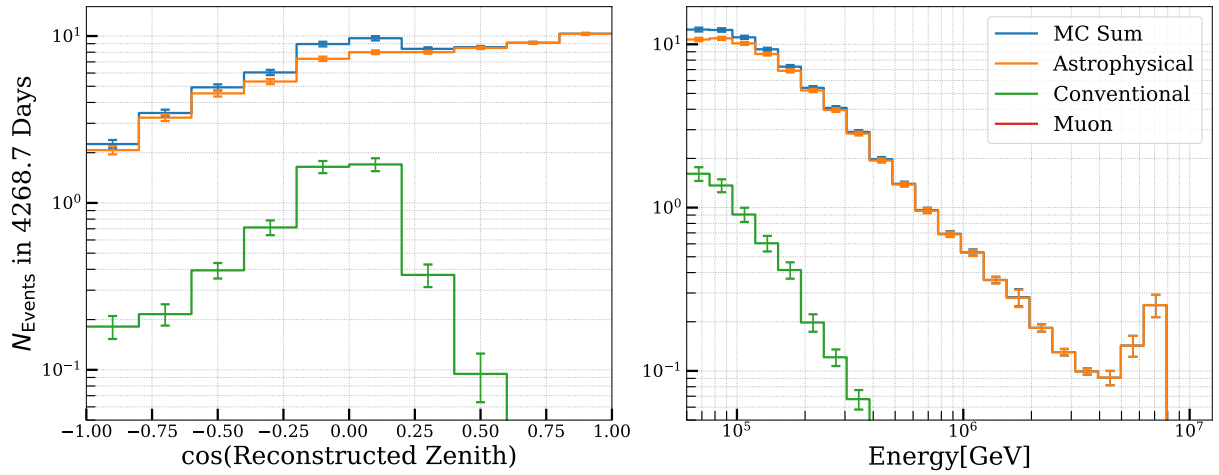


Figure 2.4: One-dimensional observable distribution, for HESE Single Cascades showing expected number of events as a function of reconstructed energy (right) and reconstructed zenith (left), broken down into different flux components, Astrophysical and Conventional Neutrinos and Muon (single muons). Only statistical errors of the MC simulation are shown.

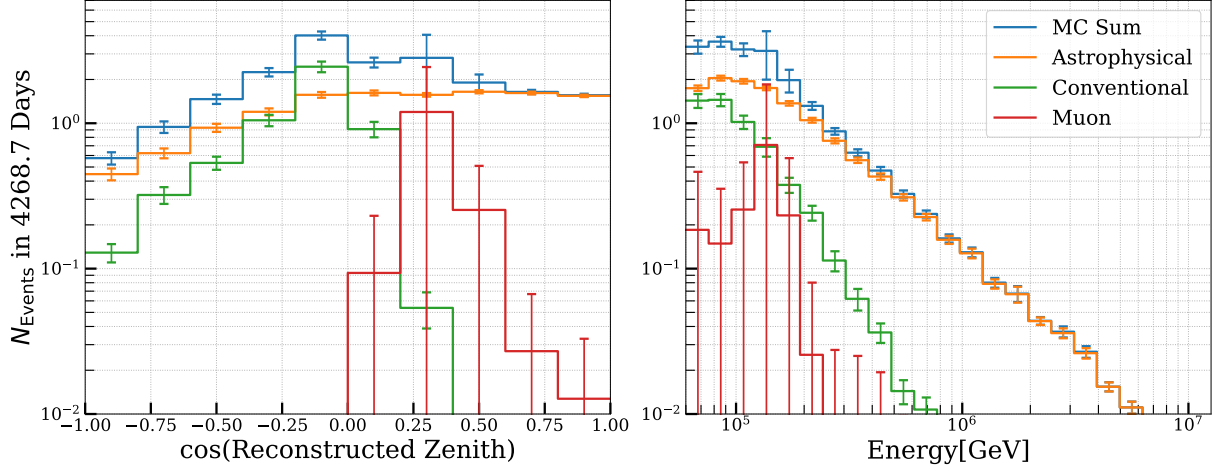


Figure 2.5: One-dimensional observable distribution, for HESE Tracks showing expected number of events as a function of reconstructed energy (right) and reconstructed zenith (left), broken down into different flux components, Astrophysical and Conventional Neutrinos and Muon (single muons). Only statistical errors of the MC simulation are shown.

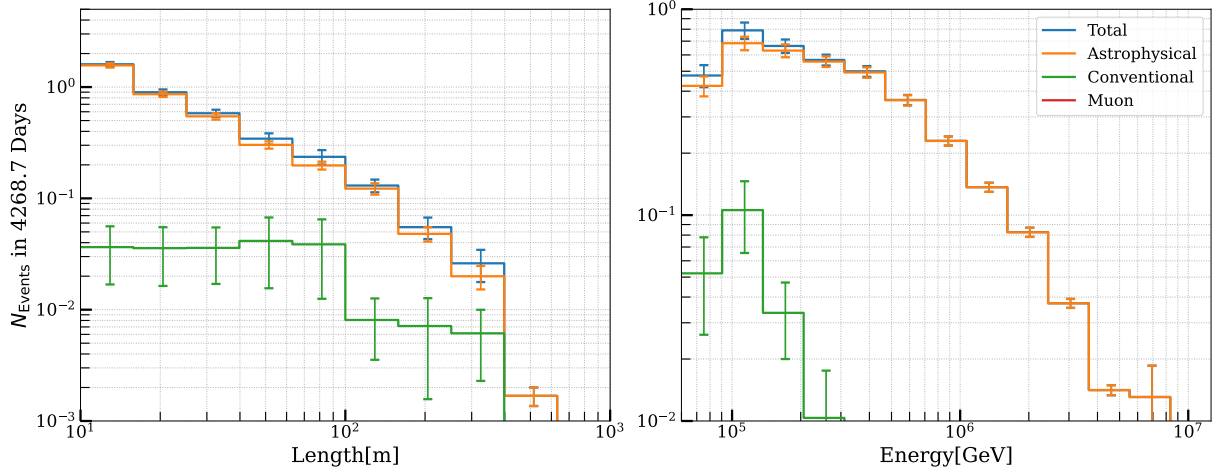


Figure 2.6: One-dimensional observable distribution, for HESE Double Cascades showing expected number of events as a function of reconstructed energy (right) and reconstructed tau decay length (left), broken down into different flux components, Astrophysical and Conventional Neutrinos and Muon (single muons). Only statistical errors of the MC simulation are shown.

2.3 Analysis Sensitivity

All fits and related calculations are carried out using a software toolkit called **NNMFit**. Developed within the IceCube collaboration, **NNMFit** has been applied in many other IceCube analyses. Essentially, the toolkit handles the statistical modeling required for forward-folding fits using high-energy neutrino data with binned likelihoods. It supports Monte Carlo event weighting, testing various flux models using signal and nuisance parameters, applying systematic detector uncertainties, and performing fits to data. The **aesara** backend [**aesara**] allows fast and efficient forward folding of Monte Carlo samples, even for large datasets, and offers automated differentiation that greatly assists in optimizing likelihood with gradient-aware minimizers [**LBFGSB**]. More details on this toolkit can be found in [17, 18].

aesara

LBFGSB

[17]: Ganster (2024), *Measurement of the high-energy astrophysical neutrino energy spectrum combining muon tracks and cascades measured at the IceCube Neutrino Observatory*

[18]: Naab (2024), *Evidence for a Break in the Diffuse Extragalactic Neutrino Spectrum*

Using all the ingredients constructed from signal and nuisance parameters, and following the described method, the flavor composition parameter space is scanned to obtain a two-dimensional confidence region for the flavor composition, as shown in Figure 2.7. To derive these limits, an Asimov dataset is constructed (see Section 2.1), assuming the benchmark astrophysical neutrino spectrum given in Equation 2.13. All other nuisance parameters are assumed to be at their baseline values listed in Table 2.2. The astrophysical neutrino flavor composition is constrained by evaluating the likelihood ratio in a profile likelihood scan, with confidence regions estimated using Wilks’s theorem. The expected number of events over 12 years of HESE data, assuming the spectrum in 2.13, is broken down by flux components and shown in Table ?? . The fitting procedure bins all HESE events above 60 TeV in reconstructed energy and further categorizes them into three subsamples based on morphology: single cascades, tracks, and double cascades. The three samples are fit jointly using the respective two-dimensional Monte Carlo templates, with the appropriate analysis variables shown in Figure 2.2, Figure 2.3, and Figure 2.1.

Table 2.2: The expected number of events from different flux components in the HESE sample, assuming a livetime of ~ 12 years, for single cascades, double cascades, and tracks categories. Only Monte Carlo uncertainties are included. The astrophysical spectrum assumed follows Equation 2.13.

	Single Cascades	Double Cascades	Tracks
Astrophysical	67 ± 1	4 ± 0.2	13 ± 0.5
Conventional	5 ± 0.7	0.2 ± 0.1	5 ± 0.6
Atm. Muons	-	-	2 ± 3
MC Sum	72 ± 2	4 ± 0.3	20 ± 3

The sensitivity results in Figure 2.7 reveal that none of the standard source scenarios discussed in Section ?? can be rejected with high significance. For instance, the neutron beam scenario (represented by the dark blue triangle) is barely excluded at the $\sim 1\sigma$ level. It is important to recall that the sensitivity of this analysis to the astrophysical tau-neutrino flux depends strongly on the assumed spectral shape of the neutrino flux. This sensitivity arises from the energy-dependent identification efficiency of tau-neutrino interactions. In interactions at higher neutrino energies, more energy is transferred to the secondary tau, increasing its decay length and enhancing identification efficiency. A softer spectrum, however, leads to more tau-neutrino interactions at lower energies, where they are harder to identify. Additionally, the sudden disappearance of line segments in the 95% confidence contours, particularly in regions where the ν_μ fraction approaches zero, is a result of the flavor fit parameterization (see Equation 2.8). By construction, this fraction cannot be zero, meaning that this phase space is inaccessible to the fit*.

While earlier versions of this analysis explored alternative flux models (for example, a broken power law introduces a break in the conventional single power law, resulting in different spectral indices on either side of the break energy), this was not done here. The decision was based on recent findings from another IceCube analysis that combined two

* The `NNMFit` toolkit used in this analysis was initially developed for a spectrum measurement utilizing a sample of through-going tracks [48]. This sample, primarily consisting of muon neutrinos, was specifically designed to measure a non-zero ν_μ fraction, which informed the choice of flavor fraction parameterization. It is important to note, however, that alternative parameterization methods exist, where the flavor fractions of the three neutrino types are represented as a vector in three-dimensional space, with their relationships defined through a spherical coordinate transformation [`golemflavor`]. This approach could also be implemented in `NNMFit`.

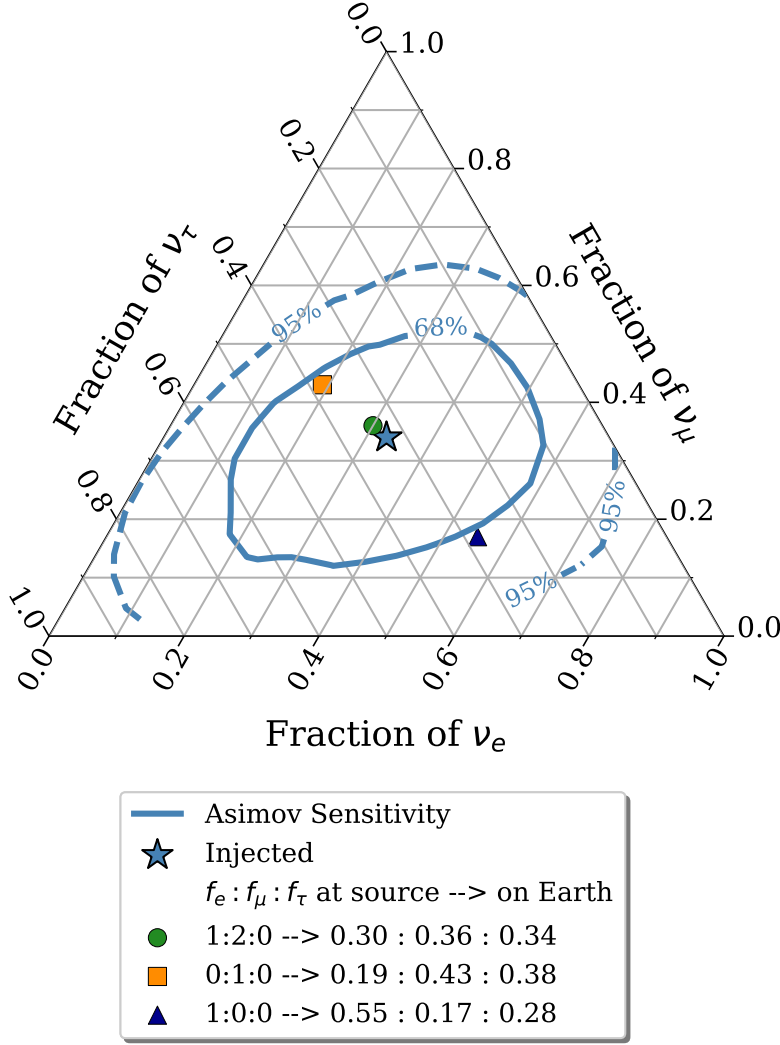


Figure 2.7: Sensitivity of the analysis presented in this thesis to measure the flavor composition using ~ 12 years of IceCube HESE data. A single power law given in Equation 2.13 is assumed, with flavour composition of $\nu_e : \nu_\mu : \nu_\tau = 1 : 1 : 1$. Contours show the 1σ (solid) and 2σ (dashed) confidence intervals assuming Wilks' theorem.

other event samples (track and cascade events, including much lower energies compared to HESE sample), revealing features in the extragalactic astrophysical neutrino spectrum based on the sensitivity to a larger range of astrophysical neutrino energies (~ 10 TeV to ~ 10 PeV) [55]. That study provided evidence of a spectral break at around 24 TeV with more than 4σ significance. The spectrum showed hardness below this break, followed by softening at higher energies, consistent with the softer spectral measurement from HESE-7.5, which is sensitive to the astrophysical neutrino flux above ~ 70 TeV [19]. Importantly, this high-statistics analysis, which extends well beyond the energy range of the current analysis, found no significant structures in the energy range accessible with the HESE sample. Furthermore, an independent study using a different event sample [23] reported similar spectral features and closely aligned best-fit values, strengthening the argument and above choice.

[55]: Naab et al. (2023), *Measurement of the astrophysical diffuse neutrino flux in a combined fit of IceCube's high energy neutrino data*

[19]: Abbasi et al. (2021), *IceCube high-energy starting event sample: Description and flux characterization with 7.5 years of data*

[23]: Basu et al. (2023), *From PeV to TeV: Astrophysical Neutrinos with Contained Vertices in 10 years of IceCube Data*

The 7.5 years of HESE data (2010-2017) was previously used to measure the composition of astrophysical neutrino flavours [21] (in particular to search for ν_τ events) and energy spectrum [19]. This dataset included 102 events, (of which 60 events were above 60 TeV), that passed the HESE selection criteria, as outlined in Section 1.2. Two events were identified as Double Cascades using the particle identifier described in Section 1.4.

For this iteration, the analysis has undergone significant changes compared to previous versions while maintaining consistent selection criteria and particle identification methods. The most notable difference lies in the ice model, specifically its influence on the reconstruction of tau decay length, detailed in Section ???. The previous iteration of the analysis used the SPICE-3.2 ice model. The SPICE-Bfr have impacts on the overall energy estimates, as the number of photons collected in a given time window have significantly changed in this model of ice depending on the alignment of DOMs with respect to the iceflow axis [29], as was discussed in Section 1.5. Furthermore, the treatment of detector systematics has evolved, utilizing the SnowStorm method (see Section 1.1.2) instead of separate Monte Carlo datasets with discrete variations of parameters related to systematic uncertainties used previously. The update also includes using the revised light-yield tables [28] for the maximum likelihood reconstruction method described in Section 1.3. Moreover, the high quantum efficiency DeepCore DOMs were included in the analysis as previously their responses were excluded from millipede reconstruction methods described in Section 1.3, as they can introduce biases which was not simulated correctly for high energy simulations. This has now been fixed and hence these DOMs were no longer excluded from the reconstructions.

Additionally, various corrections have been applied to Monte Carlo simulations, by modifying event interaction weights to incorporate corrections due to tau polarization and initial state radiation corrections to the Glashow cross-sections (see Sections 1.4.2 and 1.4.3 for details). Lastly, some of the nuisance parameters, affecting atmospheric spectra and detector responses have been introduced (as described in Section 2.2.1). Lastly, the analysis software is also different (see Section 2.3). Hence, as a first step, the 7.5 years of HESE data were re-analysed to make direct comparisons with the previous results and to re-evaluate the analysis if necessary.

This chapter presents a new flavour measurements made using 12 years (11.69 to be exact) of HESE data. It begins by discussing the re-analysing of 7.5 years of data, followed by results from the 12-year fit, including a discussion of data / Monte Carlo agreement and detailed post-unblinding checks. Finally, the flavour measurement results are presented and interpreted in the last sections.

3.1	(Re)Analysing the 7.5 years of HESE Data	36
3.2	Unblinding of 12 years of HESE data	38
3.2.1	Fit results	39
3.2.2	Data/Monte Carlo Agreement	41
3.3	Flavour Composition of Diffuse Astrophysical Neutrinos	44
3.4	Discussion	51

[21]: Abbasi et al. (2022), *Detection of astrophysical tau neutrino candidates in IceCube*

[19]: Abbasi et al. (2021), *IceCube high-energy starting event sample: Description and flux characterization with 7.5 years of data*

[29]: Abbasi et al. (2024), *In situ estimation of ice crystal properties at the South Pole using LED calibration data from the IceCube Neutrino Observatory*

[28]: Yuan (2023), *Detecting neutrinos in IceCube with Cherenkov light in the South Pole ice*

3.1 (Re)Analysing the 7.5 years of HESE Data

The re-analysing of the HESE-7.5 data (**Re-analysis Default**), revealed that 64 events met the HESE selection criteria, each with a deposited energy exceeding 60 TeV. It included 6 Double Cascade events, which is a significant increase from the previous analysis (**HESE-7.5**) that identified only two Double Cascade events. The comparison of these reconstructed variables for both iterations is shown in Table 3.1.

Table 3.1: Comparison of Reconstructed quantities of events classified as Double Cascades for results obtained using **Re-analysis Default** and **HESE-7.5** (grey cells). Shown in the table are (from left), MJD (Modified Julian Date), reconstructed length, reconstructed Energy of first (E_1) and second (E_2) cascades, Energy asymmetry (E_A), Energy Confinement (E_C) and classified morphology of the event. The two common events, 57134 (*Double Double*) and 56265 (*Big Bird*) have nearly identical reconstructed quantities.

MJD	Length		E_1		E_2		E_A		E_C		morphology	
57835	13 m	66 m	19 TeV	79 TeV	73 TeV	3 TeV	-0.58	0.93	1	1	Double	Single
57134	17 m	17 m	5.7 TeV	8.7 TeV	92 TeV	79 TeV	-0.89	-0.80	0.99	0.99	Double	Double
56603	13 m	70 m	32 TeV	85 TeV	48 TeV	1 TeV	-0.19	1	1	0.99	Double	Single
55714	14 m	26 m	5 TeV	58 TeV	82 TeV	16 TeV	-0.88	0.55	0.99	1	Double	Single
55800	13 m	20 m	128 TeV	133 TeV	72 TeV	38 TeV	0.28	0.55	1	0.99	Double	Single
56265	16 m	16 m	1.1 PeV	1.2 PeV	0.9 PeV	0.6 PeV	0.09	0.29	1	1	Double	Double

To avoid any confusion, the following terms will be used to describe which iteration of the analysis is being discussed:

HESE-7.5: It refers to previous analysis, with results described in [21]

Re-analysis Legacy: Re analysed results using SPICE-3.2.1 ice model

Re-analysis Default : Re analysed results using SPICE-Bfr ice model

A key difference in this iteration was the ice model used for reconstruction, as mentioned before. Hence, the data was re-analysed using both SPICE-3.2.1 and SPICE-Bfr to make direct comparisons with the previous results, and to check if the observed surplus of events is due to this new ice model. The re-analysis using SPICE-3.2.1 (**Re-analysis Legacy**) contained total of 62 HESE events above 60 TeV deposited energy, of which 7 events were classified as Double Cascades, the reconstructed properties and their comparisons with HESE-7.5 is shown in Table 3.2. Notably, 5 of the 7 double cascade events had been classified as single cascades in the previous analysis. The most striking differences here are specifically reconstructed length and the fact that E_1 and E_2 seem to be almost flipped for some events, even though reconstructed directions (zenith and azimuth, not shown in the table) remains almost identical. Despite the changes in the total number of classified events, the two common Double Cascade events identified in both iterations (Re-analysis Legacy and HESE-7.5) exhibited nearly identical reconstructed properties.

Table 3.2: Comparison of Reconstructed quantities of events classified as Double Cascades upon re-analysing the 7.5 years of HESE data using **SPICE-3.2.1 ice model** with previous results (grey cells). Shown in the table are (from left), MJD (Modified Julian Date), reconstructed length, reconstructed Energy of first (E_1) and second (E_2) cascades, Energy asymmetry (E_A), Energy Confinement (E_C) and classified morphology (as per previous analysis) of the event. The two common events, 57134 (*Double Double*) and 56265 (*Big Bird*) have nearly identical reconstructed quantities. The change in E_1 and E_2 changes the E_A , which is the discrimination cut between single and double cascades.

MJD	Length		E_1		E_2		E_A		E_C		morphology	
57677	27 m	37 m	3.1 TeV	128 TeV	148 TeV	4 TeV	-0.96	0.94	1	0.99	Single	
57134	16 m	17 m	18 TeV	8.7 TeV	92 TeV	79 TeV	-0.89	-0.80	0.99	0.99	Double	
56763	10.2 m	84 m	63 TeV	107 TeV	87 TeV	17 TeV	-0.16	0.72	0.99	0.99	Single	
55477	14 m	279 m	70 TeV	184 TeV	84 TeV	67 TeV	-0.09	0.46	0.99	0.98	Single	
55800	12 m	20 m	105 TeV	133 TeV	89 TeV	38 TeV	0.08	0.55	1	0.99	Single	
56221	12 m	12 m	209 TeV	102 TeV	132 TeV	237 TeV	0.22	-0.4	0.99	0.97	Track	
56265	17 m	16 m	0.8 PeV	1.2 PeV	1 PeV	0.6 PeV	-0.08	0.29	0.99	1	Double	

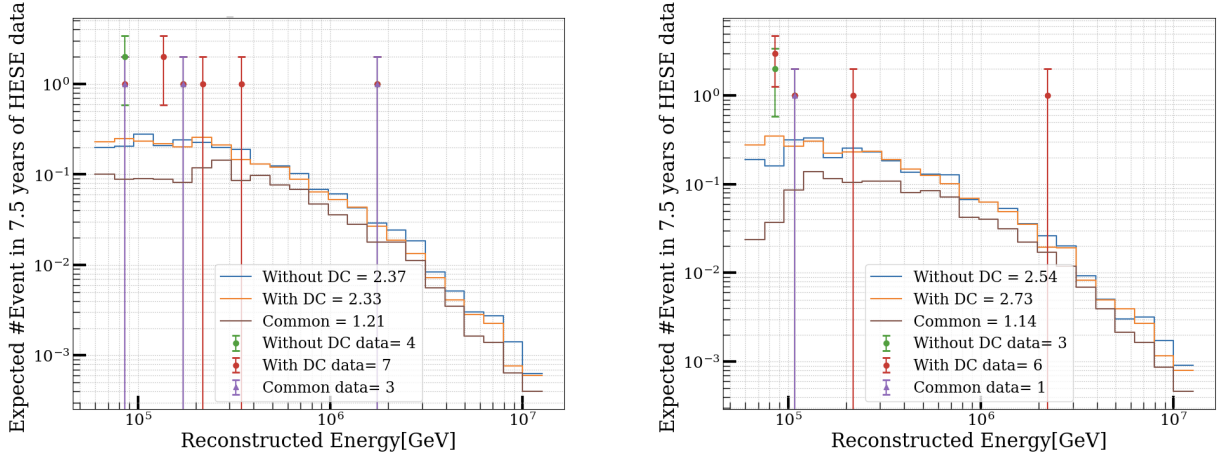


Figure 3.1: The Distribution of the expected number of events classified as double cascades in 7.5 years of HESE data, using the SPICE-3.2.1 (left) and SPICE-Bfr (right) ice models, with DeepCore (With DC) and without DeepCore (Without DC), along with the data events for each respective configuration.

For both ice models, the re-analysis observed an excess of double cascade events was observed compared to what was expected from Monte Carlo (see Figure 3.1), suggesting the presence of unnoticed changes not already accounted for. Careful search of each step in the particle identification process revealed a significant change in the reconstruction method from the previous iteration. Notably, this change involved the incorporation of high quantum efficiency Digital Optical Modules (DOMs) from DeepCore. In earlier analyses, these DOMs had been excluded from the reconstruction of high-energy neutrino events, in millipede-based algorithms reconstructions outlined in 1.3. The rationale for their exclusion stemmed from the smaller statistical uncertainties of digitized waveforms, compared to the systematic uncertainties¹. These systematic uncertainties, which were not well-characterized for individual DOMs, could not be factored into the table-based likelihood fitting method. Nonetheless, due to advancements in simulation, including enhanced reconstruction tables and detector simulations, the analysis presented in this thesis included the DeepCore DOMs, hence the next step was to explore why Monte Carlo predictions had underestimated the number of Double Cascade events. Hence, both the re-analysis were repeated by removing DeepCore DOMs from the reconstruction. Additionally, Monte Carlo simulation was also reprocessed by excluding the DeepCore to make direct Data/ Monte Carlo comparisons.

1: The statistical uncertainties for these DOMs is smaller because of their high quantum efficiencies, which produces more photo-electrons.

Table 3.3: Event classification of 7.5 years of HESE data (Previous) compared with reblinded sample outcome (all events have Reconstructed total energy > 60 TeV). The comparison is shown for all 2 different ice models, each of which further broken down into with and without the deepcore doms. The SPICE-BFR / No DeepCore configuration was selected for application to the full sample.

Morphology	Previous	Reunblinded			
		SPICE-3.2.1		SPICE-Bfr	
		DeepCore	No DeepCore	DeepCore	No DeepCore
Cascades	41	41	44	42	45
Double Cascades	2	7	4	6	3
Tracks	17	14	14	16	14
Total	60	62	62	64	62

Figure 3.1 shows the distribution of classified Double Cascade, both with and without the inclusion of DeepCore DOMs. The Monte Carlo

[56]: Aartsen et al. (2020), *In-situ calibration of the single-photoelectron charge response of the IceCube photomultiplier tubes*

simulations predicts only 2-3 Double Cascade events, yet the data revealed 6 (7) Double Cascade events using SPICE-Bfr (SPICE-3.2.1) when DeepCore DOMs were included and only 3 (4) when they were excluded. It remains clear that for both ice models, the distribution of reconstructed energy and overall expectation remains same irrespective of whether DeepCore DOMs are included or not. This discrepancy pointed to potential issues in reconstruction processes involving DeepCore DOMs upon investigation. The `millipede` reconstructions, as explained in Section 1.3 relies on table-based light yield to quantify observed charge into photons, to account for deposited energies. To do this, it relies on Single Photoelectron (SPE) templates that are associated with each DOM. These templates were re-calibrated recently by using Flasher LEDs [56], which saw a significant shift from the previously assumed mean value of this distribution for both DeepCore and Non-DeepCore DOMs. These updated templates had been used in simulations, but the change had not made its way through the calibration files used in data files (see Appendix ?? for details.). While the Non DeepCore DOMs' shift (<5%) could be fixed via inclusion of optical efficiency parameter (η_{domeff}) in the fit, the High QE DeepCore DOMs that showed >15% difference could not rely on a nuisance parameter.

All of these findings indicated that further investigation at the Monte Carlo level is necessary, Such investigations requires efforts that were beyond the timeline of this thesis work and considering the historical exclusion of DeepCore DOMs (as well as other "bad" DOMs such as bright or saturated modules) from reconstruction chains in previous iterations of HESE analyses, this analysis ultimately decided not to include DeepCore DOMs in the full sample unblinding. **By reconstructing data events using SPICE-Bfr ice model, without the DeepCore DOMs**, the re-anlaysis of the HESE-7.5 data resulted in 62 events with deposited energies above 60 TeV. Of these, 45 were classified as single cascades, 3 as Double Cascades, and 14 as track events. A detailed comparison between these reunblinded results and previous results, including classified morphologies (with different iterations of ice models and DeepCore inclusion/exclusion) is shown in Table 3.3.

3.2 Unblinding of 12 years of HESE data

The High-Energy Starting Events (HESE) sample, covering approximately 12 years of IceCube detector live time (4268.7 days) from May 2010 to August 2022, was unblinded in January 2024 for the analysis outlined in Section 4.3. This sample includes 167 events that passed the HESE selection criteria, which involved the veto and total charge conditions as detailed in Section 4.2. Of these, 3 were coincident events that had previously been removed by manual inspection, but were retained this time since the current Monte Carlo simulations now account for such coincidences. Despite this, the energy threshold of 60 TeV effectively filtered them out, resulting in a final sample of 97 events above the 60 TeV deposited energy threshold. Using the ternary topology identification method from this thesis, 64 events were classified as single cascades, 5 as double cascades, and 28 as tracks.

3.2.1 Fit results

Blind Fit results

In IceCube, all the analysis are done in a blind fashion, meaning, all expected signal and background components for this search are modeled through simulation, which is then used to develop reconstruction algorithms, event selection criteria, and analysis frameworks. Before looking at the full results, a middle step was considered where only nuisance parameters of the fit were revealed first to identify potential striking disagreement between the data and Monte Carlo or unexplainable behaviour of any nuisance parameters (e.g. if they are hitting the boundary of the fit range), called *the blind fit*. To reduce reliance on priors (as priors can penalize the likelihood as discusses in Section 2.1.1), this strategy of performing a blind fit was employed to identify nuisance parameters that require (pre-defined) priors due to their lack of constraints from the data. In addition, the goodness of fit was observed, the p-value of which was to be at least 5%. The best fit values of nuisance parameters are summarized in Table 3.4 along with their gaussian priors. Most of the nuisance parameters fit to their base values (with a likelihood profile that reflects the prior). The detector systematics are not exactly fitting to their default values, but they still remain within one standard deviation of the applied prior width.

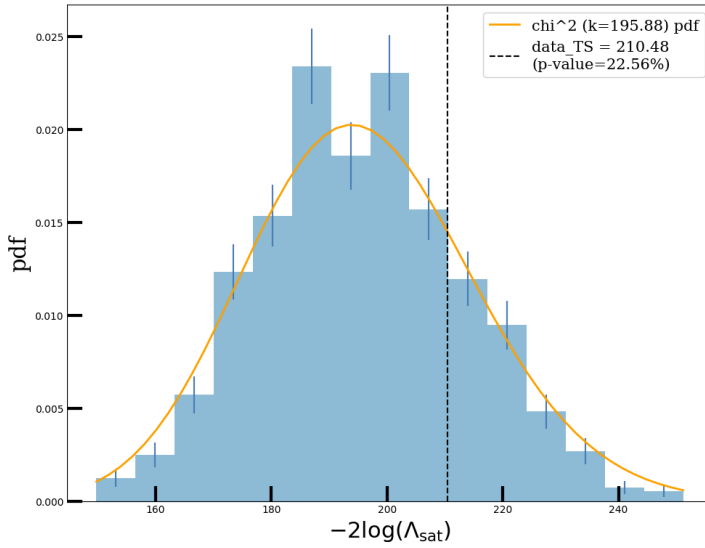


Figure 3.2: Distribution of the test statistics for 1000 pseudotrials injected at best fit (signal parameters kept blind). Vertical line shows TS of data, which matches quite well with degrees of freedom derived by fitting a χ^2 to the distribution.

Lastly, the goodness of the fit (GOF) is tested by using the pseudo data samples. This data is generated by populating the analysis histograms by drawing the number of events in each bin from a Poisson distribution with the mean given by simulation expectations for this bin at the best fit parameter values. These pseudo-data samples are then analyzed in the same way as their real data to obtain a distribution of test statistic values from the outcomes. The saturated model is the one where the data is the model, i.e. the expectation for each bin is the observed counts. Where each analysis bin observes statistically significant data, following a χ^2 distribution with degrees of freedom equal to the difference between the number of analysis bins and the number of free parameters in the fit. However, in reality, not all bins observe data, so

Table 3.4: The best-fit parameter values of the nuisance parameters. The uncertainties are calculated at the 68% confidence level through a profile likelihood scan assuming Wilks' theorem [41], in case of a flat likelihood space, fit boundaries are given as limits. Last column states the gaussian priors on the parameters (if applicable) in terms of the mean (μ) and width (σ). The table is divided in terms of type of the nuisance parameters, above part includes all the parameters that affects the atmospheric neutrino components and the lower part consists if parameters stemming through various detector components. For details, see 2.2.1

Parameter	Best-Fit value	Prior (μ, σ)
Φ_{conv} Conventional Flux normalisation	$0.99^{+0.19}_{-0.2}$	(1.0,0.2)
Φ_{prompt} Prompt Flux Normalisation	$0.0^{+2.25}_{-0.0}$	-
ξ_{CR} Interpolation between Cosmic Ray Models	0.042^{+2}_{-1}	(0,1)
$\Delta\gamma_{\text{CR}}$ Cosmic Ray Spectral Index Shift	-0.00^{+1}_{-1}	(0,0.05)
H_{Barr} Barr-parameter modifying the pion-contribution	$0.0^{+0.5}_{-0.5}$	(0,0.15)
W_{Barr} Barr-parameter modifying the kaon-contribution	$0.0^{+0.5}_{-0.5}$	(0,0.40)
Y_{Barr} Barr-parameter modifying the pion-contribution	$0.0^{+0.5}_{-0.5}$	(0,0.30)
Z_{Barr} Barr-parameter modifying the pion-contribution	$0.0^{+0.5}_{-0.5}$	(0,0.12)
Φ_{muongun} Muon Flux Normalisation	$1.16^{+0.42}_{-0.43}$	(1,0.5)
I_{scale} scale factor for Neutrino Nucleon Inelasticity weight	$0.99^{+0.1}_{-0.09}$	(1,0.1)
Detector Systematics		
η_{domeff} Optical Efficiency of DOMs	$1.04^{+0.06}_{-0.04}$	(1.0,0.1)
η_{abs} Ice Absorption Scaling	$0.99^{+0.04}_{-0.04}$	(1.0,0.05)
η_{scat} Ice Scattering Scaling	$0.98^{+0.04}_{-0.04}$	(1.0,0.05)
$\eta_{\text{h.ice-p0}}$ parametrization for refrozen icecolumn	$-0.27^{+0.28}_{-0.38}$	(-0.27,0.5)
$\eta_{\text{h.ice-p1}}$ parametrization for refrozen icecolumn	$-0.08^{+0.04}_{-0.05}$	(-0.042,0.05)
η_{aniso} Ice Anisotropy Scaling	$0.99^{+0.54}_{-0.63}$	-

some deviations are expected. By comparing the distribution of TS values from these pseudo-data trials to the distribution derived from the real data, a p-value can be calculated. The p-value represents the probability of finding a TS value from the trials that is at least as large as the one from the data fit. Figure 3.2 illustrates this distribution, where the data TS is compared with the distribution of trial TS values. The obtained p-value is 22.56%. Based on this test, it is concluded that the fit result is consistent with the expected outcome from the pseudo-data trials.

Full fit results

In this section, we discuss the full results, i.e signal parameters of the fit performed. The best fit values of the signal parameters for the 97 HESE events are summarized in Table 3.5. As explained in 2.2.1, the flavour fractions within `NNMFit` framework are fitted as scaling factors s_{ν_e} and s_{ν_τ} , which modifies the flux of electron and tau neutrinos relative to the muon neutrino flux. Which is why, the signal parameters listed in Table 3.5 needs to be converted to their corresponding flavour fractions (by using Equation 2.8), yielding a best-fit flavour composition of astrophysical neutrinos as, $\nu_e : \nu_\mu : \nu_\tau = 0.19 : 0.43 : 0.38$.

The best-fit value of astrophysical index (γ_{astro}), assuming a single power law is $2.84^{+0.19}_{-0.18}$. This value is in well agreement with the previous results

Table 3.5: The best-fit signal parameters for a single power-law model for both particle and antiparticle. The uncertainties are calculated at the 68% confidence level through a profile likelihood scan assuming Wilks' theorem.

Parameter		Best-Fit value
ϕ_{ν_μ}	astro. ν_μ normalisation [$10^{-18}\text{GeV}^{-1}\text{cm}^{-2}\text{sr}^{-1}\text{s}^{-1}$]	$2.53^{+1.78}_{-1.49}$
γ_{astro}	astro. spectral index	$2.84^{+0.19}_{-0.18}$
s_{ν_e}	astro. ν_e scaling factor to modify total flux norm ($\Phi_{\nu+\bar{\nu}}^{\text{astro}}$) relative to ϕ_{ν_μ}	$0.45^{+0.68}_{-0.40}$
s_{ν_τ}	astro. ν_τ scaling factor to modify total flux norm ($\Phi_{\nu+\bar{\nu}}^{\text{astro}}$) relative to ϕ_{ν_μ}	$0.896^{+1.34}_{-0.89}$

[19]. The normalization of the all-flavour neutrino flux derived from the fit result is $\Phi_{\nu+\bar{\nu}}^{\text{astro}} = 5.94^{+5.64}_{-4.28}$. The larger uncertainty on normalization is expected for such a fit where each flavour components are allowed to be free, that in turn have larger uncertainty on them (see Table 3.5).

[19]: Abbasi et al. (2021), *IceCube high-energy starting event sample: Description and flux characterization with 7.5 years of data*

Lastly, the table in Table 3.6 provides the breakdown of expected events classified into specific morphologies and their individual components for the best-fit model. Additionally, the comparison includes the expectation based on a $\nu_e : \nu_\mu : \nu_\tau = 1 : 1 : 1$ flavour ratio, which was determined by running the fit with fixed flavour ratios.

Table 3.6: The expected number of HESE events, classified into three morphologies, assuming a fixed flavour ratio of 1:1:1 and at the best-fit flavour ratio. The total expected event counts are further broken down into each of the flux components, Astrophysical (Astro), Conventional atmospheric neutrinos (Conv), Atmospheric Muons (Muon). Prompt atmospheric neutrino component is not shown here as best-fit value of the prompt norm (Φ_{prompt}) is 0.

Reconstructed Morphology	$\nu_e : \nu_\mu : \nu_\tau = 1 : 1 : 1(\text{fixed})$				$\nu_e : \nu_\mu : \nu_\tau = 0.19 : 0.43 : 0.38 (\text{free})$				Data
	Astro	Conv	Muon	Total	Astro	Conv	Muon	Total	
Cascades	58 ± 2	6.8 ± 0.9	-	65 ± 2.7	57 ± 2	6 ± 0.79	-	63.4 ± 2.4	64
Tracks	11.8 ± 0.7	6.3 ± 1	2 ± 3	20 ± 3.6	16 ± 0.8	5.7 ± 0.9	1.84 ± 2.7	23.4 ± 3.4	28
Double Cascades	3.2 ± 0.3	0.4 ± 0.2	-	3.5 ± 0.5	3.8 ± 0.3	0.3 ± 0.2	-	4.1 ± 0.4	5

3.2.2 Data/Monte Carlo Agreement

In addition to the goodness-of-fit test, comparisons of data with Monte Carlo expectations for a few key parameters were performed. Figure 3.3, Figure 3.4 and Figure 3.5 shows the distributions of the analysis observables for all three morphologies, for HESE events with deposited energies above 60 TeV. These plots are generated using the best-fit values stated in Table 3.5 and Table 3.4. Each figure displays individual components as well as the sum of all components under the label **MC sum**. Additionally, to highlight any noteworthy features, a ratio plot is included for each distribution, illustrating the ratio of data events to each bin of the total number of expected simulation events. Due to the low number of observed events, it is challenging to pinpoint any specific spectral features, that these distributions may exhibit.

Figure 3.3 and Figure 3.4 shows the distribution of reconstructed energy (left) and cosine of reconstructed zenith (right) for events classified as single cascades and tracks respectively in the 12 years of HESE data. The zenith plot clearly illustrates the all-sky coverage of the HESE sample as events are observed across the zenith range. It also highlights

2: this lack of simulation is due to the immense amount of computing time that is needed to produce single muons that reach the detector at such high energies.

the decrease of the conventional component in the downgoing region ($\cos(\text{zenith}) > 0.25$)), indicating the self-veto effect (described in Section 1.2). Additionally, the atmospheric muongun component is exclusively visible in the track histogram since muons produce track-like events. However, it's important to note that the expectation exhibits substantial statistical uncertainties due to the lack of sufficient muongun Monte Carlo². To mitigate the impact of statistical fluctuations caused by the low number of simulated events, a kernel density estimation (KDE) is employed to smoothen out the distribution.

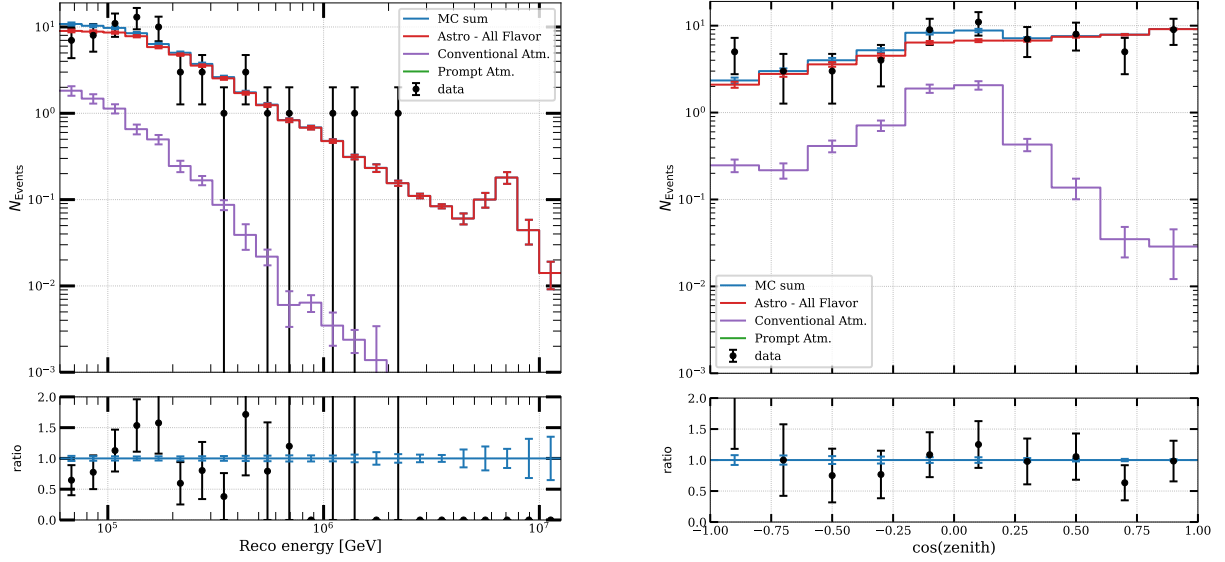


Figure 3.3: Distributions of the total reconstructed deposited energy (left) and the zenith angle (right) for events classified as **single cascades** along with data point positions. Individual components of the fits are produced using best fit values given in Table 3.5 and Table 3.4 and "MC sum" labels the sum of all of these components. The Prompt component is not shown on account of best fit value of 0 for the Φ_{prompt} .

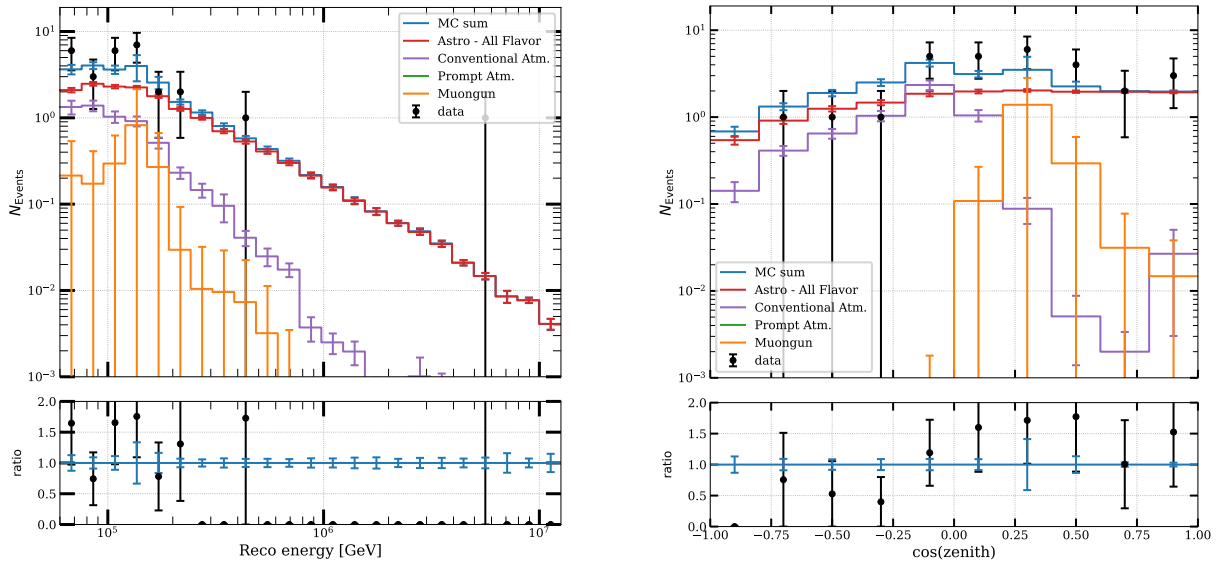


Figure 3.4: Distributions of the total reconstructed deposited energy (left) and the zenith angle (right) for events classified as **tracks** along with data point positions. Individual components of the fits are produced using best fit values given in Table 3.5 and Table 3.4 and "MC sum" labels the sum of all of these components. The Prompt component is not shown on account of best fit value of 0 for the Φ_{prompt} .

Figure 3.5 illustrates the distribution of reconstructed energy (left) and reconstructed length (right) for events classified as double cascades in the 12 years of HESE data. The first two bins show an overfluctuation while the rest of the histogram is empty, but the interpretation is challenging due to the low number of involved events. A noteworthy observation is that one event, although close to 100 TeV, has a large length, suggesting that it is a misclassified track. This particular event demonstrates Energy Confinement near the cut boundary (0.991), a cut that is supposed to differentiate between a double cascade and a track, but not quite the threshold to be a track ($E_C < 0.99$). And hence, the event passed all the cuts and ended up being classified as a double cascade. This becomes more evident in 2D distribution of energy and length in Figure 3.6, where this event clearly ends up in a background dominated region of the PDF (see 1.4 for signal and background pdfs of double cascades).

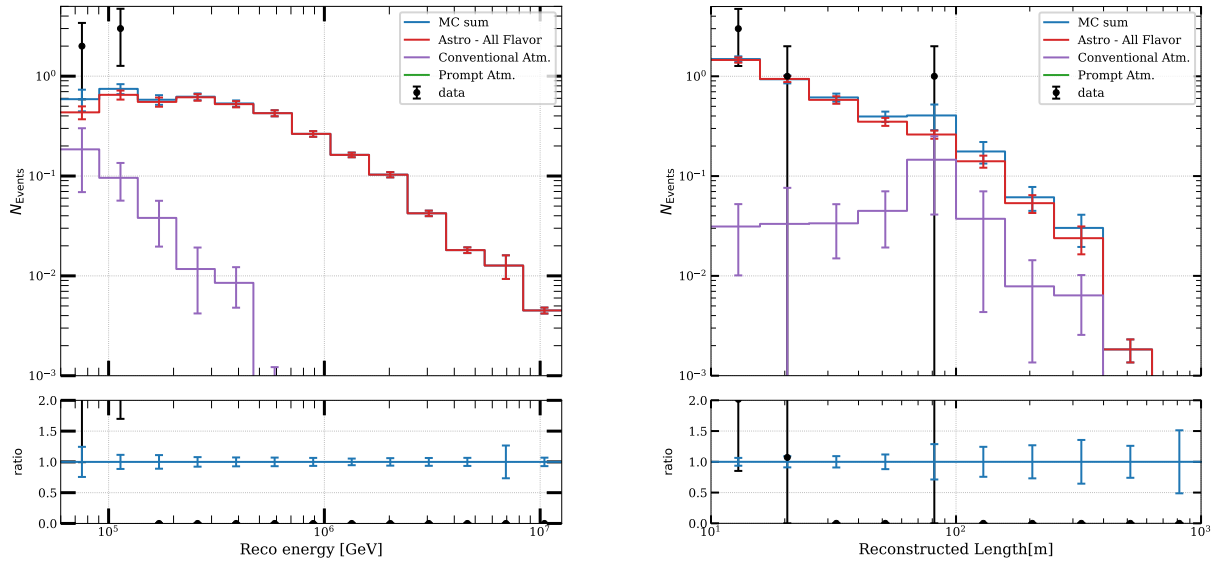


Figure 3.5: Distributions of the total reconstructed deposited energy (left) and the zenith angle (right) for events classified as **double cascades** along with data point positions. Individual components of the fits are produced using best fit values given in Table 3.5 and Table 3.4 and "MC sum" labels the sum of all of these components. The Prompt component is not shown on account of best fit value of 0 for the Φ_{prompt} .

The Figure 3.6 illustrates a pdf for the energy and length distribution of events reconstructed as double cascades, based on the best-fit values described in the tables. The vertical lines demonstrate how quickly the single-cascade background decreases with length. For instance, 68% of misclassified single cascades have reconstructed double-cascade lengths of less than ~ 14 m, 90% have lengths below ~ 20 m, and only 1% have lengths exceeding ~ 25 m. Two of the data events are outside the 68% region, but one of these events is still within the signal region indicated by white lines. The event with a reconstructed length of approximately 95 m but less than 80 TeV energy is clearly in the background region. Another important observation from this figure is the lack of smoothness expected from PDFs when performing forward folding fits. The gradients are applied as an additive correction per bin, to allow detector systematic variations in the fit.

Figure 3.7 presents the distribution of the reconstructed energy asymmetry for simulated events in the double-cascade sample, using the

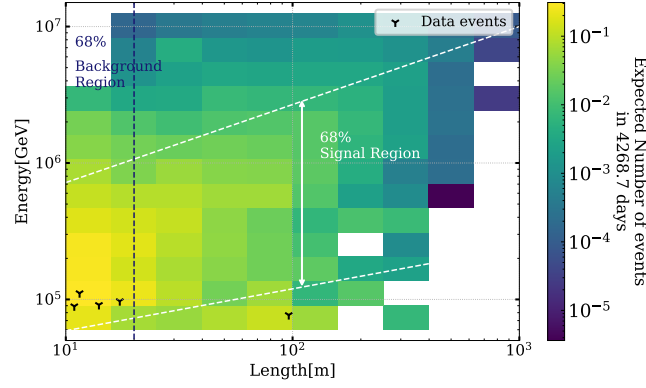


Figure 3.6: Two-dimensional distribution of reconstructed energy vs reconstructed double cascade length of the Monte Carlo events classified as double cascades. Monte Carlo sum is produced using all the best fit parameters from the Table 3.5 and Table 3.4. Position of the data events are marked with Υ . Signal (white) and Background (dark blue) dominated regions are marked with their respective percentiles.

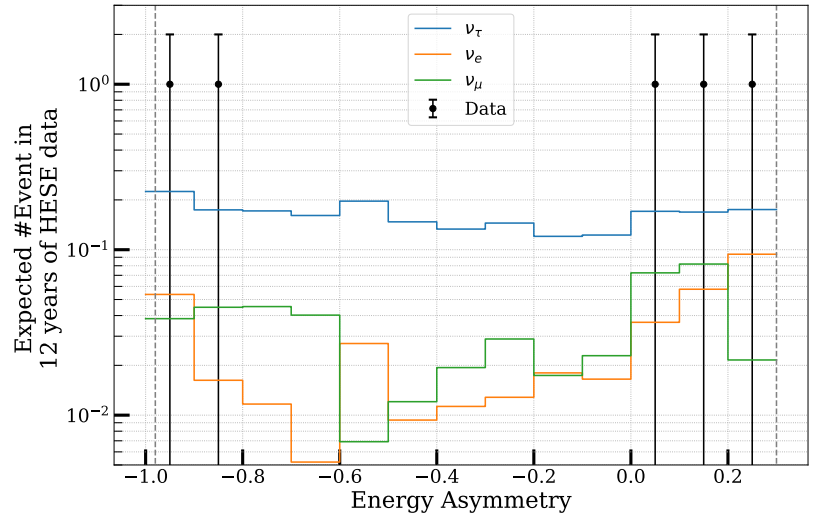


Figure 3.7: Expected distribution of reconstructed energy asymmetry, defined as $E_A = \frac{E_1 - E_2}{E_1 + E_2}$, (where E_1 and E_2 are energies of first and second cascades, respectively) at best-fit, along with data events. Distribution is shown for all flavours separately, to emphasis domination of ν_τ double cascades in the signal region (verticla grey lines).

best-fit astrophysical and atmospheric spectra. The two vertical lines represent the selection cuts applied to choose the double cascade events, as described in section 4.3. Although two of the 5 events are near the cut edge, they all still fall comfortably within the signal-dominated region of the sample.

3.3 Flavour Composition of Diffuse Astrophysical Neutrinos

The flavour composition of astrophysical neutrinos is measured using 97 high-energy starting event (HESE) events, which are divided among three morphologies. The profile likelihood scans for the flavour scale factors, specifically s_{ν_e} and s_{ν_τ} , are shown in Figure 3.8. The results indicate that the tau scale factor (s_{ν_τ}) is only able to reject the possibility of no ν_τ flux by 1σ , also reflected in the wide contours in the 2D scan shown in Figure 3.9. The 1D scans are used to derive 1σ (68%) confidence regions, shown in Table 3.5. The test statistic $-2\Delta \log \mathcal{L}$ compares the global best-fit values of the unconstrained fit to the conditional best-fit values of all remaining model parameters at a fixed scan point. The confidence

regions depicted in Figure 3.9 are calculated using Wilk's theorem [41], as a full Feldman-Cousins construction of the entire flavour composition phase space is computationally demanding (see section 2.1 for details). The applicability of Wilk's theorem is verified by comparing the coverage of the test statistic distribution from Monte Carlo pseudo-experiments to the coverage of a χ^2 -distribution, see Appendix ?? . A large fraction of the flavour composition phase space is found to be slightly over-covered, indicating that Wilk's theorem yields a conservative confidence region. Although a part of the 90% confidence region seems to suffer from slight under-coverage, the χ^2 -approximation is deemed sufficient for presenting the measurement result in Figure 3.9.

[41]: Wilks (1938), *The Large-Sample Distribution of the Likelihood Ratio for Testing Composite Hypotheses*

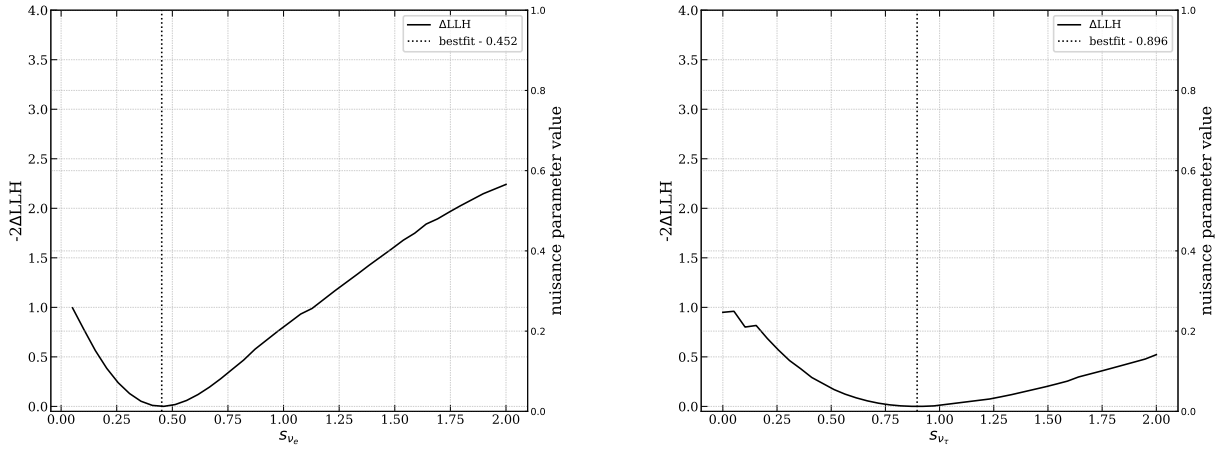


Figure 3.8: 1 dimensional profile likelihood scan of flavour scale factors s_{ν_e} (left) and s_{ν_τ} (right). Solid black line corresponds to the profile likelihood, defined by the likelihood ratio $-2\Delta\log\mathcal{L}$ comparing a fixed value to the best-fit value (denoted by dotted line).

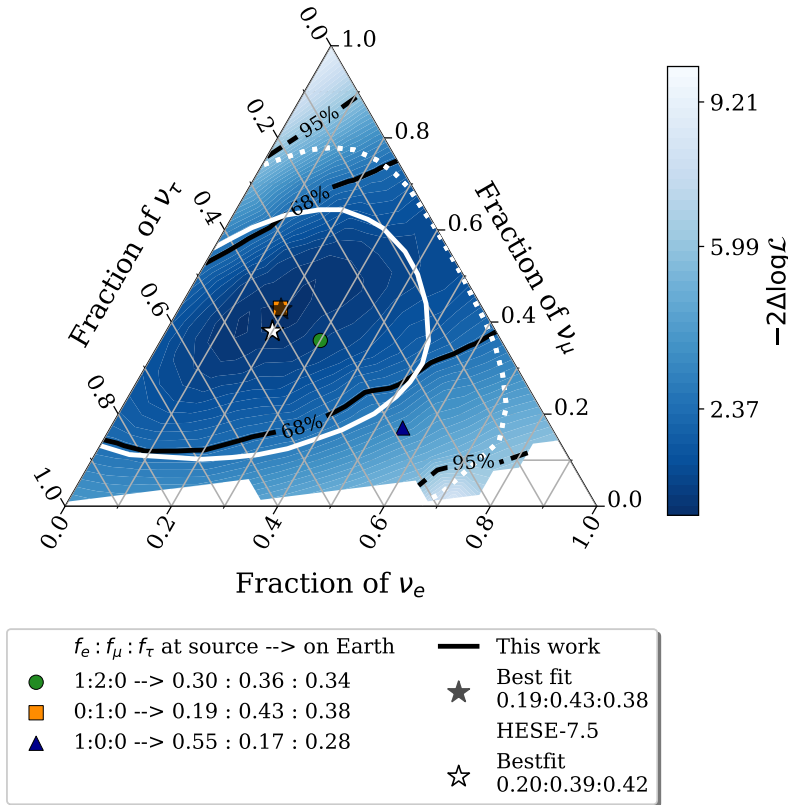


Figure 3.9: A 2 dimensional profile likelihood scan of the astrophysical neutrino flavour composition at Earth using 12 years of HES data, classified in three event morphologies (see text for details). Each point on the triangle corresponds to a flavour composition of $\nu_e : \nu_\mu : \nu_\tau$ which can be read off the axes along the tick directions specified. The best-fit flavour composition of 0.19 : 0.43 : 0.38 is indicated with a white star. The white solid and dashed lines represent the 68% and 95% confidence regions, respectively, obtained from the χ^2 -approximation using Wilk's theorem. Three flavour compositions expected at Earth from different source scenarios are also marked (??). The best-fit flavour composition of a previous measurement that used 7.5 years of HES data is indicated in grey star, with the 68% and 95% confidence regions represented by the grey solid and dotted lines, respectively [21].

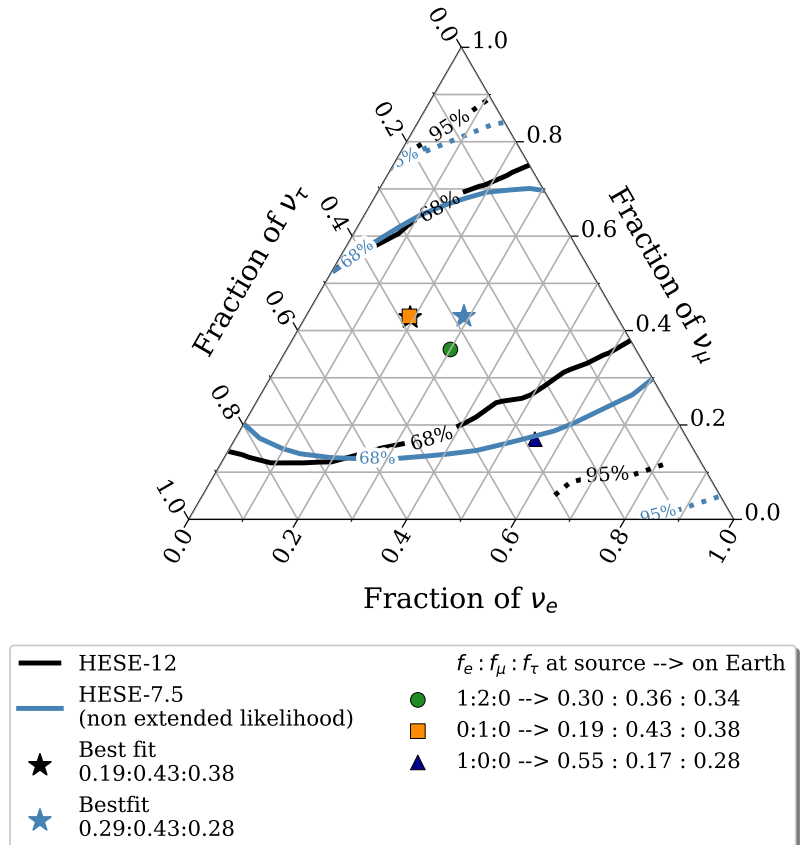
Why are the limits worse than the previous measurements?

[21]: Abbasi et al. (2022), *Detection of astrophysical tau neutrino candidates in IceCube*

[30]: Stachurska (2020), *Astrophysical Tau Neutrinos in IceCube*

The best-fit flavour composition $\nu_e : \nu_\mu : \nu_\tau = 0.19 : 0.43 : 0.38$ aligns well with the previous measurement [21] of $\nu_e : \nu_\mu : \nu_\tau = 0.20 : 0.39 : 0.42$ (grey lines in Figure 3.9). However, with 4 more years of data, which includes more double cascade events, it raises the question of why uncertainties are not shrinking. The reason is quite simple, the grey contours are derived using an extended likelihood, based on density estimates by producing a large number ($\sim 10^6$ events per particle) of resimulations of 2 classified double cascades to assess the **tauness**. A dedicated algorithm (RODEO) was developed and used to compute the density estimate for sparse datasets produced from these resimulations in multiple dimensions (see [30] for details). Because of this, the limits one should actually compare with the previous measurement should be the one derived using *the non-extended likelihood*, which is the same likelihood and PDF setup used for this iteration of the analysis. Figure 3.10 shows such a comparison. The best-fit flavour composition $\nu_e : \nu_\mu : \nu_\tau = 0.19 : 0.43 : 0.38$ measured using this analysis (black lines) aligns well with the previous measurement of $\nu_e : \nu_\mu : \nu_\tau = 0.29 : 0.43 : 0.28$ (blue lines) using the same likelihood. Although not significantly, the limits derived from this iteration do get better along the ν_μ fraction. Only 68% CL contours are shown.

Figure 3.10: The best-fit flavour composition of $0.19 : 0.43 : 0.38$ (black), using 12 years of HESE data (this work) compared with the best-fit flavour composition of a previous measurement that used 7.5 years of HESE data [21]. Comparison is shown by using the same likelihood formulation (none extended likelihood with binning fluctuations, see text for details). The solid and dashed lines represent the 68% and 95% confidence regions, respectively, obtained from the χ^2 -approximation using Wilk's theorem. Three flavour compositions expected at Earth from different source scenarios are also marked (??).



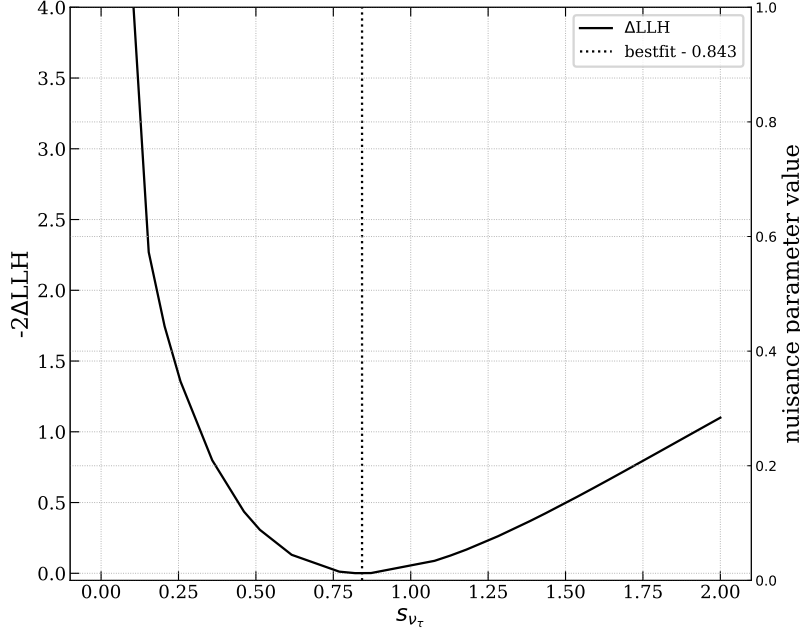


Figure 3.11: 1 dimensional profile likelihood asimov scan of ν_τ scale factor, s_{ν_τ} using **simulation** injected at best fit point. Solid black line corresponds to the profile likelihood, defined by the likelihood ratio $-2\Delta\log\mathcal{L}$ comparing a fixed value to the best-fit value (denoted by dotted line).

Comparison of sensitivities and derived constraints

The setup and all the relevant updates to the sample and selection chain for the analysis presented in this thesis were done using the best-fit values from the previous analysis. The two signal parameters that affect the flavour measurement, especially the ν_τ fraction and hence the double cascade events, are the index of the primary neutrino energy spectrum γ_{astro} (assuming a single power law) and the normalization. A harder spectrum (low γ_{astro}) leads to a larger fraction of high-energy events, while a softer spectrum (high γ_{astro}) leads to a lower fraction of high-energy flux for samples with a similar effective area. This point was discussed in section 2.3 while discussing the sensitivity of the analysis. The analysis setup and sensitivity were shown using a spectrum with an index of 2.87, which is almost identical to the best-fit value for this analysis (2.84) assuming equal partition of the neutrino flavour ($\nu_e : \nu_\mu : \nu_\tau = 0.33 : 0.33 : 0.33$). The estimated sensitivity projected much tighter constraints on 2D flavour measurements, specifically along the ν_τ axis (see Figure 2.7). To understand the lack of improvement to reduce degeneracy along the ν_e/ν_τ axis, the sensitivity of the flavour measurement was recalculated using the best fit parameters from this analysis.

The expected flavour constraints at 68% CL is shown (maroon lines) in Figure 3.12. It is determined by using an asimov dataset [44] created with the best-fit values of all signal and nuisance parameters from Table 3.5 and Table 3.4. For the sake of simplicity in comparison, a Poisson likelihood was utilized, as SAY likelihood tends to yield more conservative limits by construction (see Section 2.1.2). Constructing pseudotrials where data is drawn from SAY likelihood is not straightforward, therefore, to maintain consistency in comparisons, all fits depicted in Figure 3.12 are computed using Poisson Likelihood. Consequently, the 68% data limits displayed on the same plot (black line) are narrower compared to those shown in Figure 3.9. Additionally, there is a slight shift in the best fit point. The key

[44]: Cowan et al. (2011), *Asymptotic formulae for likelihood-based tests of new physics*

point here is that, given these signal parameters, the analysis is sensitive not only to measure a non-zero ν_τ fraction, but also to reject it with better significance (approximately 3σ as shown in Figure 3.11 - the 1D profile likelihood scan of s_{ν_τ} for the asimov dataset used to derive the 2D limits shown in Figure 3.12). The sensitivity results give rise to three questions, that will be discussed

Are the constraints derived from data reliable?

The contours shown in Figure 3.9 are based on the assumption that Wilk's theorem holds. This theorem states that the $-2\Delta\log\mathcal{L}$ approximately follows a χ^2 -distribution with $k = \text{dof}(\hat{\theta}, \hat{\xi}) - \text{dof}(\theta_t, \xi_t)$, where $\text{dof}(\theta, \xi)$ represents the number of free parameters in the fit. In the case of the flavour fit, there are 2 free parameters - s_{ν_e} and s_{ν_τ} . It is important to note that Wilk's theorem is only valid if the sample size is large and the model parameters are not bounded. However, the HESE sample is relatively small with only a few events passing all selection cuts. Additionally, the available Monte Carlo statistics are not large enough to provide sufficient statistics in every bin of the analysis histograms. Furthermore, the parameters are bounded as the flavour fractions cannot be negative. Therefore, it is essential to verify the validity of Wilk's theorem given these conditions.

The validity of Wilk's theorem was tested for a few points on the 68% and 95% contours. This was achieved by generating pseudo datasets, each injected with a specific flavour composition (a point on the contour), while keeping the rest of the fit parameters at their best-fit values, details of which can be found in Appendix ???. Each trials are fitted twice, once with a special case of flavour fractions (the one dataset was injected with), and again by leaving all the parameters free. A likelihood ratio is constructed for each trials by taking ratio of likelihood of *the conditional fit* (fixed flavour fractions) to *the free fit*. The distribution of the constructed likelihood ratio (Test Statistic) is compared with a χ^2 distribution with 2 degree of freedom³. The results agrees well with $\chi^2_{k=2}$ with minor deviations that can be explained by the fact that the two parameters of interest are correlated and hence the degree of freedom is expected to be lower than 2.

3: degree of freedom is 2 as both of the signal parameters are fixed simultaneously

Is deriving sensitivity using an asimov dataset a good choice?

The Asimov dataset is a convenient alternative to generating a large number of pseudo trials for testing a specific realization. Computing the test statistic distribution of both conditional and global best-fit values for each point in the triangle is quite expensive. It should not be assumed that the test statistic value that maximizes the likelihood of the Asimov dataset is always equal to the median of the test statistics derived from the full distribution of various pseudo experiments.

To test this, sensitivity was derived using Monte Carlo pseudotrials, similar to the one described before for wilks' validity, but this time the fixed point for all trials was kept at the data best-fit point, see Appendix ??? for details. In Figure 3.12, each point denoted with a marker "+" represents the points for which pseudo datasets were generated. Each dataset was generated by injecting the point denoted with "+" and fitted twice: once by keeping s_{ν_e} and s_{ν_τ} fixed at the data best-fit values (from Table 3.5) and once with them free. This was done to test if the true flavour fraction is what the data fit returns and with what confidence the injected point can be rejected. The result is shown in Figure Figure 3.12. The color scheme

shows the confidence level each point has to reject the null hypothesis (data best-fit in this case). As can be seen, the pseudo-trial distribution matches quite well with the Asimov sensitivity. In fact, it predicts even tighter constraints compared to the Asimov case.

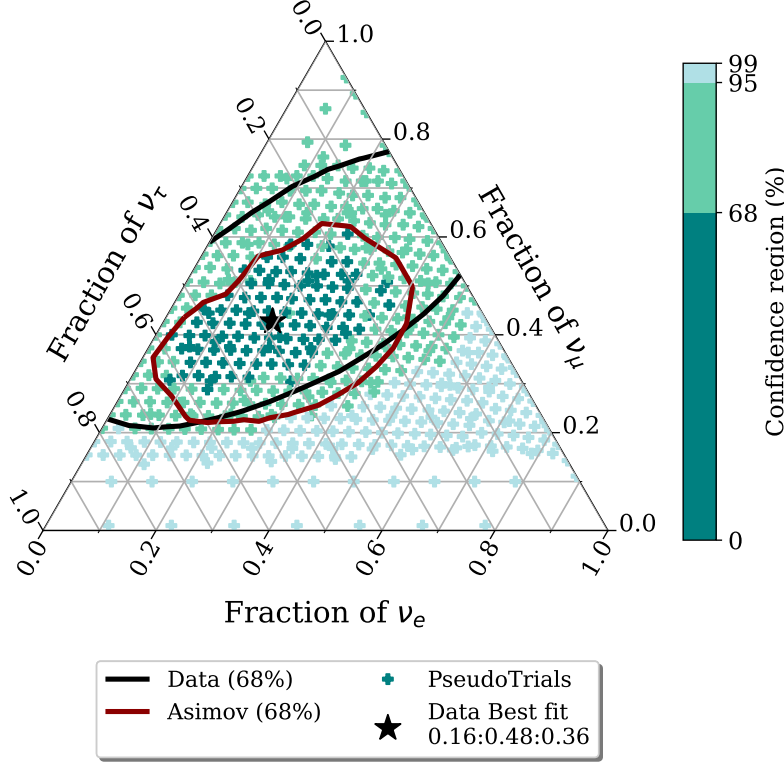


Figure 3.12: Comparison of Measured flavoured ratio (black line) with asimov sensitivity (maroon line) and pseudo trials (marked with '+'). Each + represents a pseudo dataset, drawn from flavour composition of that very point. Colorbar shows confidence intervals of each of these points, to reject the best fit flavour composition of $\nu_e : \nu_\mu : \nu_\tau = 0.19 : 0.43 : 0.38$. All other parameters of the fit are injected at their best fit values.

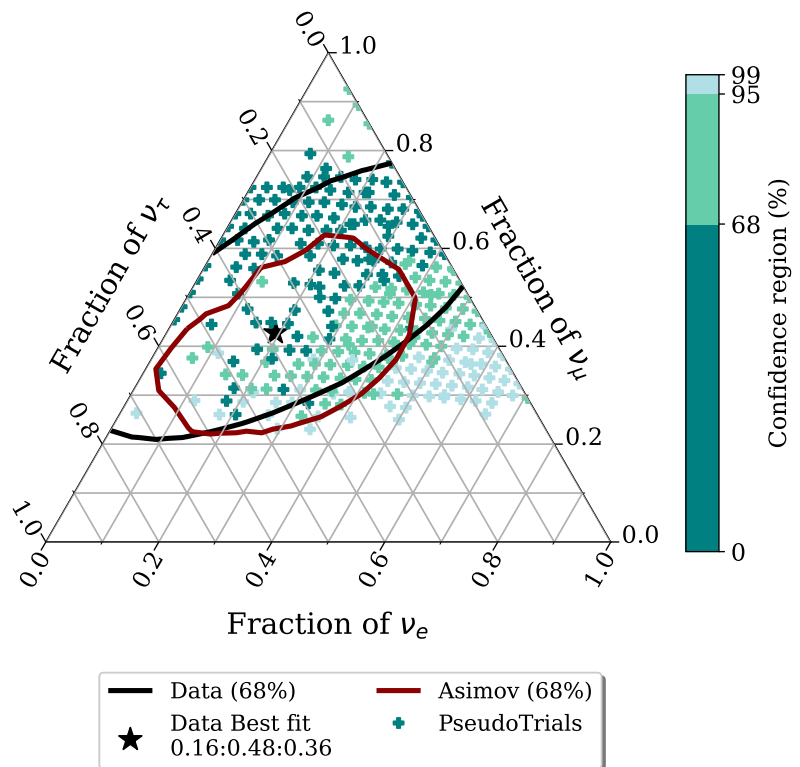
Are the double cascades found in the data a unusual realization of the expectations?

Forward-folding fits, as described in section 2.1, heavily relies on the expected values for each bin of the analysis histograms. It is crucial to choose reliable variables so that the likelihood space looks different for signal and background. For this reason, the analysis variables for double cascade bins are different from those for cascades and tracks. This is because the zenith distribution of astrophysical ν_τ flux shows no significant variation between signal and background. The PDF used in this case was selected due to the correlation of the Tau decay length (L_{dc}) with the energy of the second cascade (E_2) for double cascades resulting from ν_τ -cc interactions, contributing to the population of signal events along this diagonal (see Figure 2.1), while the background lacks this correlation. The 2D Monte Carlo PDF at best fit, shown in Figure 3.6, shows the Monte Carlo events populating the bins along the diagonal. However, the data events are in regions where the background population is expected background density is equally high. While drawing data using poisson distribution, fluctuations around the best-fit are considered which in principle should give all possible realisations of the data events ending up in bins with high expectations. Only a small subset of pseudo-datasets generated with this PDF will produce events that are similar to the observed data. Therefore, in addition to the previously described pseudotrials, only the trials with histograms that included events in

regions predominantly occupied by background-like events were retained for the sensitivity study. This approach helps verify whether the limits derived from this subset of trials resemble those obtained from the actual data.

Ideally, one would generate pseudo trials until all the Poisson-distributed events fall within the same region of the PDF as shown in Figure 3.6. However, this approach was found to be computationally expensive. For instance, each dataset displayed (around 500) in Figure 3.12 was produced from 500 trials, with each trial fitted twice. On average, each fit took approximately one hour to complete. Therefore, before proceeding, the proportion of PDFs that did not meet the cut criteria was estimated to determine whether using computational resources for further trials was justified. Several tested datasets from different regions of the triangle revealed that, for most datasets, only about 20% of the 500 trials resulted in final histograms with events concentrated in the lower energy bins. There was no feasible way to generate a sufficient number of trials to reduce statistical errors and set definitive limits. As a workaround, only the small proportion of trials that met the necessary criteria were used to generate the TS distributions, allowing an update of the sensitivity shown in Figure 3.12. This updated result is presented in Figure 3.13. As evident from the vanished points, not only were most of the trials excluded, but the confidence intervals also became significantly larger—especially along the ν_τ axis—aligning more closely with the data limits. This concludes why both asimov sensitivity and pseudo trials in Figure 3.12 showed such tight constraints.

Figure 3.13: Comparison of Measured flavoured ratio (black line) with asimov sensitivity (maroon line) and pseudo trials (marked with '+'). Each + represents a pseudo dataset, drawn from flavour composition of that very point. Colorbar shows confidence intervals of each of these points, to reject the best fit flavour composition of $\nu_e : \nu_\mu : \nu_\tau = 0.19 : 0.43 : 0.38$. Only trials with final histogram in three lower energy bins are kept in TS distribution. All other parameters of the fit are injected at their best fit values.



3.4 Discussion

The analysis setup and particle identification methods developed and refined throughout this thesis demonstrate that IceCube has sufficient sensitivity to measure the flavour ratios of the astrophysical neutrino spectrum and impose stringent constraints. However, further refinement of techniques, particularly for reconstructing double-cascade events, is necessary. With additional years of data, not only do we gain more neutrino events, but our understanding of the detector's performance also deepens. Consequently, reconstruction techniques should be re-evaluated using newer, updated simulations to better represent a realistic sample of events. Although this analysis did not yield statistically significant results, it identified several issues that raise concerns about the purity of the double-cascade sample. For instance, changing the ice model from SPICE-3.2.1 to SPICE-Bfr resulted in an increased number of classified double-cascade events, with some events being reclassified. Additionally, further investigation is needed into the false mean SPE template issue, which was identified but not fully explored. Since `millipede` reconstruction relies on these templates, excluding certain information may limit the detector's effectiveness. These issues should be addressed thoroughly before making any further measurements with this classifier. Regarding the measured flavour ratio, as illustrated in Figure 3.9, the best fit suggests sources dominated by a muon-damped production scenario; however, with the derived uncertainties, no production scenario is significantly preferred. The neutron beam scenario (source ratio $\nu_e : \nu_\mu : \nu_\tau = 1 : 0 : 0$, evolving to 0.55:0.17:0.28 on Earth) is disfavored by roughly 1σ but remains consistent within 2σ .

A specific measurement of the neutrino energy spectrum was not part of the analysis presented here, as the focus was primarily on flavour measurement, with efforts directed toward improving particle identification. Nonetheless, the HESE sample could also be used to measure, and potentially search for, spectral features. Recent independent studies have discovered a spectral break in the neutrino spectrum at around 30 TeV, softening the spectrum at higher energies, which is within the range of this analysis [55, 57]. This finding offers insight into why previous measurements targeting different energy ranges produced significantly different spectral indices for a single power-law spectrum [19, 48, 58]. Since the HESE sample focuses on high-energy events, where no such spectral features have been observed, and has much lower statistical power than those other samples, no spectral feature searches were attempted during this work.

A less model-dependent approach to describing the astrophysical neutrino flux is the differential unfolding of the energy spectrum. This method divides the flux into energy bins, where each bin is fit independently with a constant $\sim E^{-2}$ spectrum, rather than assuming a continuous power-law across the entire energy range. Ideally, this unfolding would be performed separately for each neutrino flavour to avoid assuming a uniform spectral shape for all flavours. Measuring the flavour composition as a function of energy would also be valuable, as neutrino production processes are energy-dependent. However, due to the limited statistical power of the current dataset, meaningful results could not yet be obtained.

[55]: Naab et al. (2023), *Measurement of the astrophysical diffuse neutrino flux in a combined fit of IceCube's high energy neutrino data*

[57]: Basu et al. (2023), *From PeV to TeV: Astrophysical Neutrinos with Contained Vertices in 10 years of IceCube Data*

[19]: Abbasi et al. (2021), *IceCube high-energy starting event sample: Description and flux characterization with 7.5 years of data*

[48]: Abbasi et al. (2022), *Improved Characterization of the Astrophysical Muon-neutrino Flux with 9.5 Years of IceCube Data*

[58]: Aartsen et al. (2020), *Characteristics of the Diffuse Astrophysical Electron and Tau Neutrino Flux with Six Years of IceCube High Energy Cascade Data*

Finally, improvements in reconstruction methods and more data are necessary for future experiments to shed more light on flavour measurements. Double-cascade reconstruction currently has an upper energy limit, as higher-energy events are only partially contained within the detector due to their geometry. In addition, improved detection hardware could provide better information on photon charge and direction, enhancing the overall reconstruction process. These points, along with the potential to constrain the flavour compositions of astrophysical neutrinos for a proposed new generation of neutrino detectors, will be discussed in detail in the next chapter.

APPENDIX

List of Figures

1.1	Light emission pattern of a simulated muon track event, using the direction propagation program CLSim. The colored lines show individual photon paths through ice, with red indicating earlier and blue indicating later compared to an unscattered photon. Figure taken from [10]	4
1.2	Illustration of the SnowStorm method described in the text. It depicts the contrast between numerous discrete shifts in nuisance parameters (indicated by red squares), each necessitating an entire Monte Carlo set, in comparison to a single SnowStorm Monte Carlo (represented by small blue dots). Figure taken from [16]	5
1.3	The top view (above) and side view (below) display the veto DOMs and the DOMs within the fiducial volume for HESE. DOMs highlighted in red represent the veto region, while those in blue define the fiducial volume. Events where the initial detected light comes from the veto region are excluded from the analysis. Figure taken from [19].	6
1.4	The neutrino effective areas for the high-energy starting event selection as a function of neutrino energy. The distributions are shown for all neutrino flavors, broken down by various zenith angle ranges.	7
1.5	The Atmospheric neutrino fluxes at $E_\nu = 10$ TeV. The plot shows the fraction of the flux that is not vetoed, known as passing fluxes (solid lines), alongside the total flux entering the detector (dashed lines) as a function of the cosine of the zenith angle. Figure is adapted from [24].	8
1.6	The atmospheric neutrino fluxes and the effect of self-vetoing are displayed for a neutrino energy level of $E_\nu = 100$ TeV, see caption of Figure 1.5. Figure taken from [24].	8
1.7	A sketch of energy asymmetry, it is a measure of the relative distribution of total deposited energy between the two cascades, as defined in 1.6. Sketch is adapted from [13].	11
1.8	A sketch of Energy Confinement, it is a measure of how confined are reconstructed energy depositions E_1 and E_2 are within their reconstructed vertices. The confinement, as shown in the sketch is checked within 40 m of the vertices. Sketch is adapted from [13].	12
1.9	The event classification scheme for the Ternary PID. The first level evaluates reconstruction quality; if the criteria are not met, events are classified as single cascades or tracks based on the likelihood values L_{monopod} and L_{SPE16} . The second level considers the reconstructed length, using a threshold below which distinct vertices of double cascades appear as a single cascade. The third and fourth levels focus on energy confinement and energy asymmetry, respectively. The last level is added to improve purity of the double cascade sample at high energies where misclassification is prominent due to glashow events.	13
1.10	Fraction of flavor content per bin in double cascade events. The left panel shows the distribution without the criteria of Total $E_{\text{deposited}} \geq 3$ PeV and $L_{\text{reco}} \leq 20$ m, indicating <i>purity contamination</i> at high energies from $\bar{\nu}_e$ Glashow events. The right panel presents the distribution after reclassifying double cascades as single cascades under these conditions.	14
1.11	The cross section for the Glashow resonance process $\nu_e + e^- \rightarrow W^- \rightarrow X$ is shown with and without initial state radiation and Doppler broadening. The black curve represents the cross section without these effects, the blue dotted curve includes initial state radiation, the orange dotted curve shows Doppler broadening, and the red curve combines both effects. Figure taken from [35].	15
1.12	Length Bias of true double cascades, classified as double cascades, as function of Azimuth angle. Vertical lines shows the direction of the major anisotropy axis. Caption below each figures shows which combination of icemodel is used in simulation and reconstruction respectively. Each figure also shows reduced value of χ^2 calculated by fitting the showed horizontal line, see text for details.	17
1.13	Simulation using Spice-3.2.1 and reconstruction using Spice-3.2.1 but no effective distance. See caption of Figure 1.12 for details.	18

2.1	2D Monte Carlo templates, constructed using reconstructed total energy (E_{Tot}) and double cascade length (L_{dc}) for events classified as double cascades . The signal (left), representing ν_τ -induced double cascades, shows a clear correlation between L_{dc} and E_{tot} , with 68% of events within the indicated signal region (dotted white line). In contrast, the background (right), consisting of ν_μ and ν_e events, lacks this correlation and clusters at low L_{dc} , 68% of all the background events lying below the indicated white dotted verticle line.	29
2.2	2D Monte Carlo templates, constructed using reconstructed total energy (E_{Tot}) and reconstructed zenith ($\cos(\theta_z)$) for events classified as single cascades . The signal (left), representing <i>Astrophysical neutrinos</i> of the sample and the background (right), representing <i>Atmospheric neutrinos</i> , including conventional, prompt and single muon fluxes.	29
2.3	2D Monte Carlo templates, constructed using reconstructed total energy (E_{Tot}) and reconstructed zenith ($\cos(\theta_z)$) for events classified as tracks . The signal (left), representing <i>Astrophysical neutrinos</i> of the sample and the background (right), representing <i>Atmospheric neutrinos</i> , including conventional, prompt and single muon fluxes.	30
2.4	One-dimensional observable distribution, for HESE Single Cascades showing expected number of events as a function of reconstructed energy (right) and reconstructed zenith (left), broken down into different flux components, Astrophysical and Conventional Neutrinos and Muon (single muons). Only statistical errors of the MC simulation are shown.	30
2.5	One-dimensional observable distribution, for HESE Tracks showing expected number of events as a function of reconstructed energy (right) and reconstructed zenith (left), broken down into different flux components, Astrophysical and Conventional Neutrinos and Muon (single muons). Only statistical errors of the MC simulation are shown.	31
2.6	One-dimensional observable distribution, for HESE Double Cascades showing expected number of events as a function of reconstructed energy (right) and reconstructed tau decay length (left), broken down into different flux components, Astrophysical and Conventional Neutrinos and Muon (single muons). Only statistical errors of the MC simulation are shown.	31
2.7	Sensitivity of the analysis presented in this thesis to measure the the flavor composition using ~ 12 years of IceCube HESE data. A single power law given in Equation 2.13 is assumed, with flavour composition of $\nu_e : \nu_\mu : \nu_\tau = 1 : 1 : 1$. Contours show the 1σ (solid) and 2σ (dashed) confidence intervals assuming Wilks' theorem.	33
3.1	The Distribution of the expected number of events classified as double cascades in 7.5 years of HESE data, using the SPICE-3.2.1 (left) and SPICE-Bfr (right) ice models, with DeepCore(<i>With DC</i>) and without DeepCore (<i>Without DC</i>), along with the data events for each respective configuration.	37
3.2	Distribution of the test statistics for 1000 pseudotrials injected at best fit (signal parameters kept blind). Veritcal line shows TS of data, which matches quite well with degrees of freedom derived by fitting a χ^2 to the distribution.	39
3.3	Distributions of the total reconstructed deposited energy (left) and the zenith angle (right) for events classified as single cascades along with data point positions. Individual components of the fits are produced using best fit values given in Table 3.5 and Table 3.4 and "MC sum" labels the sum of all of these components. The Prompt component is not shown on account of best fit value of 0 for the Φ_{prompt}	42
3.4	Distributions of the total reconstructed deposited energy (left) and the zenith angle (right) for events classified as tracks along with data point positions. Individual components of the fits are produced using best fit values given in Table 3.5 and Table 3.4 and "MC sum" labels the sum of all of these components. The Prompt component is not shown on account of best fit value of 0 for the Φ_{prompt}	42
3.5	Distributions of the total reconstructed deposited energy (left) and the zenith angle (right) for events classified as double cascades along with data point positions. Individual components of the fits are produced using best fit values given in Table 3.5 and Table 3.4 and "MC sum" labels the sum of all of these components. The Prompt component is not shown on account of best fit value of 0 for the Φ_{prompt}	43

3.6	Two-dimensional distribution of reconstructed energy vs reconstructed double cascade length of the Monte Carlo events classified as double cascades. Monte Carlo sum is produced using all the best fit parameters from the Table 3.5 and Table 3.4. Position of the data events are marked with Υ . Signal (white) and Background (dark blue) dominated regions are marked with their respective percentiles.	44
3.7	Expected distribution of reconstructed energy asymmetry, defined as $E_A = \frac{E_1 - E_2}{E_1 + E_2}$, (where E_1 and E_2 are energies of first and second cascades, respectively) at best-fit, along with data events. Distribution is shown for all flavours separately, to emphasis domination of ν_τ double cascades in the signal region (verticla grey lines).	44
3.8	1 dimensional profile likelihood scan of flavour scale factors s_{ν_e} (left) and s_{ν_τ} (right). Solid black line corresponds to the profile likelihood, defined by the likelihood ratio $-2\Delta\log\mathcal{L}$ comparing a fixed value to the best-fit value (denoted by dotted line).	45
3.9	A 2 dimensional profile likelihood scan of the astrophysical neutrino flavour composition at Earth using 12 years of HESE data, classified in three event morphologies (see text for details). Each point on the triangle corresponds to a flavour composition of $\nu_e : \nu_\mu : \nu_\tau$ which can be read off the axes along the tick directions specified. The best-fit flavour composition of 0.19 : 0.43 : 0.38 is indicated with a white star. The white solid and dashed lines represent the 68% and 95% confidence regions, respectively, obtained from the χ^2 -approximation using Wilk's theorem. Three flavour compositions expected at Earth from different source scenarios are also marked (??). The best-fit flavour composition of a previous measurement that used 7.5 years of HESE data is indicated in grey star, with the 68% and 95% confidence regions represented by the grey solid and dotted lines, respectively [21].	45
3.10	The best-fit flavour composition of 0.19 : 0.43 : 0.38 (black), using 12 years of HESE data (this work) compared with the best-fit flavour composition of a previous measurement that used 7.5 years of HESE data [21]. Comparison is shown by usingth esame likelihood formulation (none extended likelihood without resimulations, see text for details). The solid and dashed lines represent the 68% and 95% confidence regions, respectively, obtained from the χ^2 -approximation using Wilk's theorem. Three flavour compositions expected at Earth from different source scenarios are also marked (??).	46
3.11	1 dimensional profile likelihood asimov scan of ν_τ scale factor, s_{ν_τ} using simulation injected at best fit point. Solid black line corresponds to the profile likelihood, defined by the likelihood ratio $-2\Delta\log\mathcal{L}$ comparing a fixed value to the best-fit value (denoted by dotted line).	47
3.12	Comparison of Measured flavoured ratio (black line) with asimov sensitivity(maroon line) and pseudo trials (marked with '+'). Each + represents a pseudo dataset, drawn from flavour composition of that very point. Colorbar shows confidence intervals of each of these points, to reject the best fit flavour composition of $\nu_e : \nu_\mu : \nu_\tau = 0.19 : 0.43 : 0.38$. All other parameters of the fit are injected at their best fit values.	49
3.13	Comparison of Measured flavoured ratio (black line) with asimov sensitivity(maroon line) and pseudo trials (marked with '+'). Each + represents a pseudo dataset, drawn from flavour composition of that very point. Colorbar shows confidence intervals of each of these points, to reject the best fit flavour composition of $\nu_e : \nu_\mu : \nu_\tau = 0.19 : 0.43 : 0.38$. Only trials with final histogram in three lower energy bins are kept in TS distribution. All other parameters of the fit are injected at their best fit values.	50

List of Tables

1.1	The four comparison scenarios that were analyzed. The First icemodel in the name always refers to the one used in simulation (second column) and the second refers to the one used in reconstruction (reconstruction). Last column points to corresponding figures.	17
2.1	Parameters used in the likelihood described in Equation 2.3. The gaussian priors on the parameters (if applicable) in terms of the mean (μ) and width (σ) are stated on the alongside.	24
2.2	The expected number of events from different flux components in the HESE sample, assuming a livetime of ~ 12 years, for single cascades, double cascades, and tracks categories. Only Monte Carlo uncertainties are included. The astrophysical spectrum assumed follows Equation 2.13. .	32
3.1	Comparison of Reconstructed quantities of events classified as Double Cascades for results obtained using Re-analysis Default and HESE-7.5 (grey cells). Shown in the table are (from left), MJD (Modified Julian Date), reconstructed length, reconstructed Energy of first (E_1) and second (E_2) cascades, Energy asymmetry (E_A), Energy Confinement (E_C) and classified morphology of the event. The two common events, 57134 (<i>Double Double</i>) and 56265 (<i>Big Bird</i>) have nearly identical reconstructed quantities.	36
3.2	Comparison of Reconstructed quantities of events classified as Double Cascades upon re-analysing the 7.5 years of HESE data using SPICE-3.2.1 ice model with previous results (grey cells). Shown in the table are (from left), MJD (Modified Julian Date), reconstructed length, reconstructed Energy of first (E_1) and second (E_2) cascades, Energy asymmetry (E_A), Energy Confinement (E_C) and classified morphology (as per previous analysis) of the event. The two common events, 57134 (<i>Double Double</i>) and 56265 (<i>Big Bird</i>) have nearly identical reconstructed quantities. The change in E_1 and E_2 changes the E_A , which is the discrimination cut between single and double cascades. .	36
3.3	Event classification of 7.5 years of HESE data	37
3.4	The best-fit parameter values of the nuisance parameters. The uncertainties are calculated at the 68% confidence level through a profile likelihood scan assuming Wilks' theorem [41], in case of a flat likelihood space, fit boundaries are given as limits. Last column states the gaussian priors on the parameters (if applicable) in terms of the mean (μ) and width (σ). The table is divided in terms of type of the nuisance parameters, above part includes all the parameters that affects the atmospheric neutrino components and the lower part consists if parameters stemming through various detector components. For details, see 2.2.1	40
3.5	The best-fit signal parameters for a single power-law model for both particle and antiparticle. The uncertainties are calculated at the 68% confidence level through a profile likelihood scan assuming Wilks' theorem.	41
3.6	The expected number of HESE events, classified into three morphologies, assuming a fixed flavour ratio of 1:1:1 and at the best-fit flavour ratio. The total expected event counts are further broken down into each of the flux components, Astrophysical (Astro), Conventional atmospheric neutrinos (Conv), Atmospheric Muons (Muon). Prompt atmospheric neutrino component is not shown here as best-fit value of the prompt norm (Φ_{prompt}) is 0.	41

Bibliography

Here are the references in citation order.

- [1] A. M. Dziewonski and D. L. Anderson. “Preliminary reference earth model”. In: *Phys. Earth Planet. Interiors* 25 (1981), pp. 297–356. doi: [10.1016/0031-9201\(81\)90046-7](https://doi.org/10.1016/0031-9201(81)90046-7) (cited on page 2).
- [2] F. Halzen and D. Saltzberg. “Tau-neutrino appearance with a 1000 megaparsec baseline”. In: *Physical Review Letters* 81 (1998), pp. 4305–4308 (cited on page 2).
- [3] D. Heck et al. “CORSIKA: A Monte Carlo code to simulate extensive air showers”. In: (Feb. 1998) (cited on page 2).
- [4] J. van Santen. “Neutrino Interactions in IceCube above 1 TeV: Constraints on Atmospheric Charmed-Meson Production and Investigation of the Astrophysical Neutrino Flux with 2 Years of IceCube Data taken 2010–2012”. PhD thesis. Wisconsin U., Madison, Nov. 2014 (cited on pages 3, 9).
- [5] J. H. Koehne et al. “PROPOSAL: A tool for propagation of charged leptons”. In: *Comput. Phys. Commun.* 184 (2013), pp. 2070–2090. doi: [10.1016/j.cpc.2013.04.001](https://doi.org/10.1016/j.cpc.2013.04.001) (cited on page 4).
- [6] D. Chirkin and W. Rhode. “Propagating leptons through matter with Muon Monte Carlo (MMC)”. In: (Aug. 2004) (cited on page 4).
- [7] B. Voigt. “Sensitivity of the IceCube detector for ultra-high energy electron-neutrino events”. PhD thesis. Humboldt-Universität zu Berlin, Mathematisch-Naturwissenschaftliche Fakultät I, 2008. doi: <http://dx.doi.org/10.18452/15850> (cited on page 4).
- [8] L. Radel and C. Wiebusch. “Calculation of the Cherenkov light yield from electromagnetic cascades in ice with Geant4”. In: *Astropart. Phys.* 44 (2013), pp. 102–113. doi: [10.1016/j.astropartphys.2013.01.015](https://doi.org/10.1016/j.astropartphys.2013.01.015) (cited on page 4).
- [9] L. Rädcl and C. Wiebusch. “Calculation of the Cherenkov light yield from low energetic secondary particles accompanying high-energy muons in ice and water with Geant 4 simulations”. In: *Astroparticle Physics* 38 (June 2012) (cited on page 4).
- [10] C. Kopper. *Photons from IceCube Muon*. URL: <https://www.psu.edu/news/research/story/national-science-foundation-funds-supercomputer-cluster-penn-state> (cited on page 4).
- [11] C. Kopper. *Clsim*. URL: <https://github.com/claudiok/clsim> (cited on page 4).
- [12] D. Chirkin. “Photon tracking with GPUs in IceCube”. In: *Nuclear Instruments and Methods in Physics Research Section A: Accelerators, Spectrometers, Detectors and Associated Equipment* 725 (2013), pp. 141–143. doi: <https://doi.org/10.1016/j.nima.2012.11.170> (cited on page 4).
- [13] M. Usner. “Search for Astrophysical Tau-Neutrinos in Six Years of High-Energy Starting Events in the IceCube Detector”. PhD thesis. Humboldt-Universität zu Berlin, Mathematisch-Naturwissenschaftliche Fakultät, 2018. doi: <http://dx.doi.org/10.18452/19458> (cited on pages 5, 8, 10–12, 14, 16, 18, 25).
- [14] N. Whitehorn, J. van Santen, and S. Lafebre. “Penalized splines for smooth representation of high-dimensional Monte Carlo datasets”. In: *Computer Physics Communications* 184.9 (2013), pp. 2214–2220. doi: <https://doi.org/10.1016/j.cpc.2013.04.008> (cited on pages 5, 8).
- [15] R. Abbasi et al. “Calibration and characterization of the IceCube photomultiplier tube”. In: *Nuclear Instruments and Methods in Physics Research Section A: Accelerators, Spectrometers, Detectors and Associated Equipment* 618.1 (2010), pp. 139–152. doi: <https://doi.org/10.1016/j.nima.2010.03.102> (cited on page 5).

- [16] M. G. Aartsen et al. “Efficient propagation of systematic uncertainties from calibration to analysis with the SnowStorm method in IceCube”. In: *JCAP* 10 (2019), p. 048. doi: [10.1088/1475-7516/2019/10/048](https://doi.org/10.1088/1475-7516/2019/10/048) (cited on pages 5, 25).
- [17] E. Ganster. “Measurement of the high-energy astrophysical neutrino energy spectrum combining muon tracks and cascades measured at the IceCube Neutrino Observatory”. PhD thesis. RWTH Aachen University, RWTH Aachen U., 2024 (cited on pages 6, 31).
- [18] R. Naab. “Evidence for a Break in the Diffuse Extragalactic Neutrino Spectrum”. PhD thesis. Humboldt-Universität zu Berlin, Mathematisch-Naturwissenschaftliche Fakultät, 2024 (cited on pages 6, 25, 26, 31).
- [19] R. Abbasi et al. “IceCube high-energy starting event sample: Description and flux characterization with 7.5 years of data”. In: *Physical Review D* 104.2 (2021). doi: [10.1103/physrevd.104.022002](https://doi.org/10.1103/physrevd.104.022002) (cited on pages 6, 8, 23, 25, 26, 28, 33, 35, 41, 51).
- [20] M. G. Aartsen et al. “Evidence for High-Energy Extraterrestrial Neutrinos at the IceCube Detector”. In: *Science* 342.6161 (2013), p. 1242856. doi: [10.1126/science.1242856](https://doi.org/10.1126/science.1242856) (cited on page 6).
- [21] R. Abbasi et al. “Detection of astrophysical tau neutrino candidates in IceCube”. In: *The European Physical Journal C* 82.11 (2022). doi: [10.1140/epjc/s10052-022-10795-y](https://doi.org/10.1140/epjc/s10052-022-10795-y) (cited on pages 6, 10, 27, 35, 36, 45, 46).
- [22] M. G. Aartsen et al. “Atmospheric and astrophysical neutrinos above 1 TeV interacting in IceCube”. In: *Phys. Rev. D* 91 (2 Jan. 2015), p. 022001. doi: [10.1103/PhysRevD.91.022001](https://doi.org/10.1103/PhysRevD.91.022001) (cited on page 7).
- [23] V. Basu et al. “From PeV to TeV: Astrophysical Neutrinos with Contained Vertices in 10 years of IceCube Data”. In: *PoS ICRC2023* (2023), p. 1007. doi: [10.22323/1.444.1007](https://doi.org/10.22323/1.444.1007) (cited on pages 7, 33).
- [24] C. Argüelles Delgado et al. “Unified atmospheric neutrino passing fractions for large-scale neutrino telescopes”. In: *Journal of Cosmology and Astroparticle Physics* 2018 (July 2018), pp. 047–047. doi: [10.1088/1475-7516/2018/07/047](https://doi.org/10.1088/1475-7516/2018/07/047) (cited on pages 7, 8).
- [25] T. Yuan et al. *nuVeto*. URL: <https://github.com/tianluyuan/nuVeto> (cited on page 8).
- [26] A. Fedynitch et al. “Calculation of conventional and prompt lepton fluxes at very high energy”. In: *EPJ Web Conf.* 99 (2015). Ed. by D. Berge et al., p. 08001. doi: [10.1051/epjconf/20159908001](https://doi.org/10.1051/epjconf/20159908001) (cited on pages 8, 24).
- [27] M. G. Aartsen et al. “Energy Reconstruction Methods in the IceCube Neutrino Telescope”. In: *JINST* 9 (2014), P03009. doi: [10.1088/1748-0221/9/03/P03009](https://doi.org/10.1088/1748-0221/9/03/P03009) (cited on pages 8, 16).
- [28] T. Yuan. “Detecting neutrinos in IceCube with Cherenkov light in the South Pole ice”. In: *Nucl. Instrum. Meth. A* 1054 (2023), p. 168440. doi: [10.1016/j.nima.2023.168440](https://doi.org/10.1016/j.nima.2023.168440) (cited on pages 8, 35).
- [29] R. Abbasi et al. “In situ estimation of ice crystal properties at the South Pole using LED calibration data from the IceCube Neutrino Observatory”. In: *The Cryosphere* 18.1 (2024), pp. 75–102. doi: [10.5194/tc-18-75-2024](https://doi.org/10.5194/tc-18-75-2024) (cited on pages 9, 35).
- [30] J. Stachurska. “Astrophysical Tau Neutrinos in IceCube”. PhD thesis. Humboldt-Universität zu Berlin, Mathematisch-Naturwissenschaftliche Fakultät, 2020. doi: [http://dx.doi.org/10.18452/21611](https://dx.doi.org/10.18452/21611) (cited on pages 11, 14, 16, 25, 46).
- [31] A. Cooper-Sarkar, P. Mertsch, and S. Sarkar. “The high energy neutrino cross-section in the Standard Model and its uncertainty”. In: *JHEP* 08 (2011), p. 042. doi: [10.1007/JHEP08\(2011\)042](https://doi.org/10.1007/JHEP08(2011)042) (cited on pages 14, 27).
- [32] S. L. Glashow. “Resonant Scattering of Antineutrinos”. In: *Phys. Rev.* 118 (1 Apr. 1960), pp. 316–317. doi: [10.1103/PhysRev.118.316](https://doi.org/10.1103/PhysRev.118.316) (cited on page 14).
- [33] D. Garg et al. “Neutrino propagation in the Earth and emerging charged leptons with nuPyProp”. In: *JCAP* 01 (2023), p. 041. doi: [10.1088/1475-7516/2023/01/041](https://doi.org/10.1088/1475-7516/2023/01/041) (cited on page 15).
- [34] C. A. Argüelles et al. “Tau depolarization at very high energies for neutrino telescopes”. In: *Phys. Rev. D* 106.4 (2022), p. 043008. doi: [10.1103/PhysRevD.106.043008](https://doi.org/10.1103/PhysRevD.106.043008) (cited on page 15).

- [35] G.-y. Huang, M. Lindner, and N. Volmer. “Inferring astrophysical neutrino sources from the Glashow resonance”. In: *JHEP* 11 (2023), p. 164. doi: [10.1007/JHEP11\(2023\)164](https://doi.org/10.1007/JHEP11(2023)164) (cited on pages 15, 16).
- [36] A. Garcia et al. “Complete predictions for high-energy neutrino propagation in matter”. In: *JCAP* 09 (2020), p. 025. doi: [10.1088/1475-7516/2020/09/025](https://doi.org/10.1088/1475-7516/2020/09/025) (cited on page 15).
- [37] R. Gauld. “Precise predictions for multi-TeV and PeV energy neutrino scattering rates”. In: *Phys. Rev. D* 100.9 (2019), p. 091301. doi: [10.1103/PhysRevD.100.091301](https://doi.org/10.1103/PhysRevD.100.091301) (cited on page 15).
- [38] A. Loewy, S. Nussinov, and S. L. Glashow. “The Effect of Doppler Broadening on the 6.3 PeV W^- Resonance in $\bar{\nu}_e e^-$ Collisions”. In: (July 2014) (cited on pages 15, 16).
- [39] D. Chirkin and IceCube Collaboration. “Evidence of optical anisotropy of the South Pole ice”. In: *International Cosmic Ray Conference*. Vol. 33. International Cosmic Ray Conference. Jan. 2013, p. 3338 (cited on page 16).
- [40] O. Behnke and L. Moneta. *Parameter Estimation*. John Wiley and Sons, Ltd, 2013. Chap. 2, pp. 27–73 (cited on page 20).
- [41] S. S. Wilks. “The Large-Sample Distribution of the Likelihood Ratio for Testing Composite Hypotheses”. In: *Annals Math. Statist.* 9.1 (1938), pp. 60–62. doi: [10.1214/aoms/1177732360](https://doi.org/10.1214/aoms/1177732360) (cited on pages 21, 40, 45).
- [42] G. J. Feldman and R. D. Cousins. “Unified approach to the classical statistical analysis of small signals”. In: *Phys. Rev. D* 57 (7 Apr. 1998), pp. 3873–3889. doi: [10.1103/PhysRevD.57.3873](https://doi.org/10.1103/PhysRevD.57.3873) (cited on page 21).
- [43] B. Sen, M. Walker, and M. Woodroffe. “On the unified method with nuisance parameters”. In: *Statistica Sinica* 19 (Jan. 2009), pp. 301–314 (cited on page 21).
- [44] G. Cowan et al. “Asymptotic formulae for likelihood-based tests of new physics”. In: *Eur. Phys. J. C* 71 (2011). [Erratum: *Eur.Phys.J.C* 73, 2501 (2013)], p. 1554. doi: [10.1140/epjc/s10052-011-1554-0](https://doi.org/10.1140/epjc/s10052-011-1554-0) (cited on pages 21, 22, 47).
- [45] C. A. Argüelles, A. Schneider, and T. Yuan. “A binned likelihood for stochastic models”. In: *JHEP* 06 (2019), p. 030. doi: [10.1007/JHEP06\(2019\)030](https://doi.org/10.1007/JHEP06(2019)030) (cited on page 22).
- [46] T. K. Gaisser. “Spectrum of cosmic-ray nucleons, kaon production, and the atmospheric muon charge ratio”. In: *Astroparticle Physics* 35.12 (2012), pp. 801–806. doi: <https://doi.org/10.1016/j.astropartphys.2012.02.010> (cited on page 24).
- [47] F. Riehn et al. “The hadronic interaction model SIBYLL 2.3c and Feynman scaling”. In: *PoS ICRC2017* (2018), p. 301. doi: [10.22323/1.301.0301](https://doi.org/10.22323/1.301.0301) (cited on page 24).
- [48] R. Abbasi et al. “Improved Characterization of the Astrophysical Muon–neutrino Flux with 9.5 Years of IceCube Data”. In: 928.1 (2022), p. 50. doi: [10.3847/1538-4357/ac4d29](https://doi.org/10.3847/1538-4357/ac4d29) (cited on pages 24, 26, 32, 51).
- [49] H. M. Niederhausen. “Measurement of the High Energy Astrophysical Neutrino Flux Using Electron and Tau Neutrinos Observed in Four Years of IceCube Data”. PhD thesis. Stony Brook U., 2018 (cited on page 25).
- [50] G. D. Barr et al. “Uncertainties in Atmospheric Neutrino Fluxes”. In: *Phys. Rev. D* 74 (2006), p. 094009. doi: [10.1103/PhysRevD.74.094009](https://doi.org/10.1103/PhysRevD.74.094009) (cited on page 25).
- [51] A. Fedynitch and M. Huber. “Data-driven hadronic interaction model for atmospheric lepton flux calculations”. In: *Phys. Rev. D* 106.8 (2022), p. 083018. doi: [10.1103/PhysRevD.106.083018](https://doi.org/10.1103/PhysRevD.106.083018) (cited on page 25).
- [52] P. Eller et al. “A model independent parametrization of the optical properties of the refrozen IceCube drill holes”. In: *PoS ICRC2023* (2023), p. 1034. doi: [10.22323/1.444.1034](https://doi.org/10.22323/1.444.1034) (cited on page 27).
- [53] M. G. Aartsen et al. “Measurements using the inelasticity distribution of multi-TeV neutrino interactions in IceCube”. In: *Phys. Rev. D* 99.3 (2019), p. 032004. doi: [10.1103/PhysRevD.99.032004](https://doi.org/10.1103/PhysRevD.99.032004) (cited on page 27).

- [54] N. Lad et al. “Summary of IceCube tau neutrino searches and flavor composition measurements of the diffuse astrophysical neutrino flux”. In: *PoS ICRC2023* (2023), p. 1122. doi: [10.22323/1.444.1122](https://doi.org/10.22323/1.444.1122) (cited on page 28).
- [55] R. Naab et al. “Measurement of the astrophysical diffuse neutrino flux in a combined fit of IceCube’s high energy neutrino data”. In: *PoS ICRC2023* (2023), p. 1064. doi: [10.22323/1.444.1064](https://doi.org/10.22323/1.444.1064) (cited on pages 33, 51).
- [56] M. G. Aartsen et al. “In-situ calibration of the single-photoelectron charge response of the IceCube photomultiplier tubes”. In: *JINST* 15.06 (2020), P06032. doi: [10.1088/1748-0221/15/06/P06032](https://doi.org/10.1088/1748-0221/15/06/P06032) (cited on page 38).
- [57] V. Basu et al. “From PeV to TeV: Astrophysical Neutrinos with Contained Vertices in 10 years of IceCube Data”. In: *PoS ICRC2023* (2023), p. 1007. doi: [10.22323/1.444.1007](https://doi.org/10.22323/1.444.1007) (cited on page 51).
- [58] M. G. Aartsen et al. “Characteristics of the Diffuse Astrophysical Electron and Tau Neutrino Flux with Six Years of IceCube High Energy Cascade Data”. In: *Phys. Rev. Lett.* 125 (12 Sept. 2020), p. 121104. doi: [10.1103/PhysRevLett.125.121104](https://doi.org/10.1103/PhysRevLett.125.121104) (cited on pages 26, 51).